The Thesis Committee for Peidong Zhao
Certifies that this is the approved version of the following thesis:

Numerical Investigation of Lost Circulation and Fracture Resistance Enhancement Mechanism

APPROVED BY
SUPERVISING COMMITTEE:

Supervisor:

Kenneth E. Gray

Claudia L. Santana

Numerical Investigation of Lost Circulation and Fracture Resistance Enhancement Mechanism

by

Peidong Zhao, B.S.

Thesis

Presented to the Faculty of the Graduate School of

The University of Texas at Austin

in Partial Fulfillment

of the Requirements

for the Degree of

Master of Science in Engineering

The University of Texas at Austin

August 2016

Dedication

To my mother, Hongguang Lv, and father, Jianguo Zhao,

for their love.

Acknowledgements

I would like to express my greatest gratitude to my advisor, Dr. Kenneth E. Gray, for his recognition, inspiration, and immense guidance. Dr. Gray has been supportive since the first day I began this process. With his plentiful research experience, he has not only offered me assistantship, but also moral support for my scientific research. The joy and enthusiasm he has for our research group was contagious and motivational.

I wish to convey my appreciation to Dr. Claudia L. Santana from Halliburton for her time and effort in reviewing this thesis. I am overwhelmed by having the opportunity to discuss my research with her. Constructive discussions on rock mechanics and the operational experiences she shared have extensively contributed to this thesis.

I am grateful for the Department of Petroleum and Geosystems Engineering at the University of Texas at Austin. My education and research experiences were outstanding, and I owe thanks to professors and staff members for their technical training and administrative support. I would like to thank all my colleagues in the research group for their assistance. Special thanks go to Dr. Yongcun Feng for his helpful guidance on the topic of lost circulation. I would like to mention Mahdi Haddad, Hanyi Wang, and Haotian Wang for their knowledge sharing on fracture modeling. I would like to extend my gratitude to all my dear friends for their company since beginning this work.

I genuinely acknowledge the Wider Windows Industrial Affiliate Program within the University of Texas at Austin for financial and logistical support of this work. Project support and technical discussions with industrial colleagues from Wider Windows sponsors are gratefully acknowledged, including BHP Billiton, British Petroleum, Chevron, ConocoPhillips, Halliburton, Marathon, National Oilwell Varco, Occidental Oil and Gas, and Shell.

Abstract

Numerical Investigation of Lost Circulation and Fracture Resistance Enhancement Mechanism

Peidong Zhao, M.S.E

The University of Texas at Austin, 2016

Supervisor: Kenneth E. Gray

Drilling in complex geological settings often possesses significant risk for unplanned events that potentially intensify the economic problem of cost-demanding operations. Lost circulation, a major challenge in well construction operations, refers to the loss of drilling fluid into formation during drilling operations. Over years of research effort and field practices, wellbore strengthening techniques have been successfully applied in the field to mitigate lost circulation and have proved effective in extending the drilling mud weight margin to access undrillable formations. In fact, wellbore strengthening contributes additional resistance to fractures so that an equivalent circulating density higher than the conventionally estimated fracture gradient can be exerted on the wellbore. Therefore, wellbore strengthening techniques artificially elevate the upper limit of the mud weight window.

Wellbore strengthening techniques have seen profound advancement in the last 20 years. Several proposed wellbore strengthening models have contributed considerable

knowledge for the drilling community to mitigate lost circulation. However, in each of these models, wellbore strengthening is uniquely explained as a different concept, with supporting mathematical models, experimental validation, and field best practices. Due to simplifications of the mathematical models, the limited scale of experiments, and insufficient validation of field observations, investigating the fundamental mechanisms of wellbore strengthening has been an active and controversial topic within the industry. Nevertheless, lost circulation is undoubtedly induced by tensile failure or reopening of natural fractures when excessive wellbore pressure appears.

In this thesis, a fully coupled hydraulic fracturing model is developed using Abaqus Standard. By implementing this numerical model, an extensive parametric study on lost circulation is performed to investigate mechanical behaviors of the wellbore and the induced fracture under various rock properties and bottomhole conditions. Based on the fracture analysis, a novel approach to simulate the fracture sealing effect of wellbore strengthening is developed, along with a workflow quantifying fracture gradient extension for drilling operations. A case study on fracture sealing is performed to investigate the role of sealing permeability and sealing length. The results described in this thesis indicate the feasibility of hoop stress enhancement, detail the mechanism of fracture resistance enhancement, and provide insights for lost circulation mitigation and wellbore strengthening treatment.

Table of Contents

List of Tables

List of Figures

Chapter 1: Introduction

1.1 Lost Circulation and Wellbore Strengthening

A narrow mud weight window (MWW) possesses significant challenges for drilling operations. Both hydrostatic and equivalent mud weight (EMW) must be strictly maintained within the window, which is confined by a minimum requirement to prevent fluid influx and wellbore instability and a maximum allowance to avoid wellbore breakdown and lost circulation. Lost circulation occurs when wellbore pressure exceeds the window.

The process of lost circulation can be described as unintentional hydraulic fracturing of a wellbore. The sources of abnormally high hydraulic pressure can be derived from fluid surge effect, annulus pack-off, high annulus friction, etc. When hydraulic pressure exceeds fracture initiation pressure (FIP) and fracture propagation pressure (FPP), hydraulic fracturing is induced. Consequently, drilling fluid is lost into formation as it invades the drilling-induced fracture. For an intact wellbore, circular geometry transforms and magnifies the in-situ stresses into a more compressive form at the wellbore so that the FIP at the wellbore can be significantly higher than the far-field FPP. However, if fractures are induced, the additional pressure-holding strength of the wellbore as a continuum medium vanishes. Moreover, if natural fractures exist, the wellbore is naturally weak in holding mud pressure. As a result, to prevent fracture propagation and lost circulation at a fractured wellbore, the maximum allowable hydraulic pressure should be reduced, and the MWW upper limit is governed only by far-field FPP. In conventional well design, mud weight selection is intended for an intact wellbore. After lost circulation, necessary mud weight reduction is often circumscribed by following the drilling plan so that protracted nonproductive time is required to address the induced fractures in order to reach the target

depth; for a deepwater operation, this often means several million dollars per day. In a worst-case scenario, when severe loss is encountered, the target formation can be considered inaccessible for management. Therefore, the economic cost of lost circulation is substantial.

To mitigate lost circulation, wellbore strengthening (WBS) techniques are widely practiced in the field. However, with different company preferences and guided models, the treatment conducted for operations can be very different. WBS treatment can be categorized by different operational procedures as preventive treatment, which continuously circulates lost circulation material (LCM) within the drilling fluid, and remedial treatment, which squeezes LCM to the induced fractures after lost circulation. WBS treatment can be also categorized by different objectives: the hoop stress enhancement method (i.e., stress cage) and fracture resistance method (i.e., tip screen-out). In either case, WBS aims to prevent further fracture propagation. In this thesis, we will mostly use the latter categorization.

The purpose of the hoop stress enhancement method is to increase apparent fracture resistance by modifying hoop stress when the fracture is propped. Even though stress cannot be measured, hoop stress enhancement is theoretically proved (Alberty and McLean 2004, Wang et al. 2007, Morita and Fuh 2012) and is supported by field observations (Aston et al. 2004, Dupriest 2005, Song and Rojas 2006, Aston et al. 2007). The objective of the fracture resistance enhancement method is to raise the apparent FPP by preventing wellbore pressure from being transmitted to the fracture tip. Fracture propagation resistance enhancement is supported by experimental and field observations (Morita et al. 1990, Fuh et al. 1992, Onyia 1994, Morita et al. 1996, Fuh et al. 2007, Van Oort et al. 2001, Razavi et al. 2015).

1.2 OBJECTIVES OF THIS RESEARCH

The objectives of this research are

- Investigating factors involved during lost circulation.
- Exploring controllable factors to prevent further mud loss.
- Validating hoop stress enhancement and fracture resistance enhancement.
- Quantifying fracture gradient extension for drilling operations.

1.3 THESIS ORGANIZATION

In Chapter 2, we present a literature review of the underlying mechanisms of lost circulation and WBS. In Chapter 3, we first give a brief description of the cohesive zone model (CZM), after which the methodology and formulation of a fracturing simulator is discussed. In Chapter 4, we present a parametric study on various rock properties and bottomhole conditions, followed by discussion of the results. In Chapter 5, a novel approach considering a fracture resistance enhancement mechanism is introduced with a recommended workflow for drilling operations. Then, a case study on sealing permeability and length is discussed with quantification of fracture gradient extension with respect to specific sealing condition.

Chapter 2: Background and Literature Review

Lost circulation has notoriously caused major nonproductive time in drilling operations. During a severe lost circulation event, excessive wellbore pressure hydraulically fractures the wellbore and stimulates drilling mud flowing into the formation. As a consequence, normal bottomhole conditions are altered and drilling operations have to be ceased to remedy the unplanned downhole disturbance. Overall, lost circulation is a multiphysics process and requires an in-depth understanding of wellbore failure mechanisms in order to develop mitigating techniques. This chapter speaks to the topics of MWW, wellbore fracturing, and previous studies on lost circulation treatment. We aim to present a comprehensive description of the lost circulation process and a constructive understanding of the fundamental mechanisms of WBS.

2.1 MUD WEIGHT WINDOW

Mud weight expresses the density (mass per volume) of a drilling fluid. This unique concept originated in the 1940s when drilling engineering was still a craft, not a science. Habitually, drilling engineers characterize pressure in the wellbore or formation by EMW or pressure gradient. By converting pressure units to density units, the pressure gradient is practical for comparing pressures at a given depth and selecting an appropriate mud weight.

During drilling operations, drilling fluid is the first barrier to control fluid influx to the wellbore and is the overriding method to support excavation of deep-buried rocks. For these purposes, drilling engineers assess a safe MWW (or drilling/operating margin) to confine the mud weight to a minimum requirement to prevent fluid influx and wellbore instability and to a maximum allowance to avoid wellbore breakdown and fluid losses (as shown in Figure 2.1).

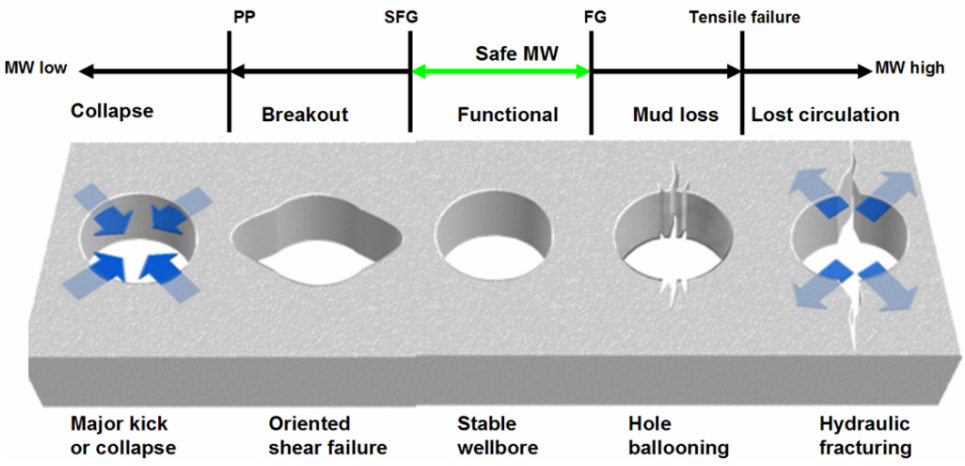

Figure 2.1: Mud weight window showing relationship between annular fluid pressure, near-wellbore stress, and modes of wellbore failure. (Zhang et al. 2008)

Pore pressure gradient is the pore pressure at a given depth divided by the true vertical depth (TVD). When mud weight is lower than pore pressure gradient in a permeable zone, formation fluid (such as oil, gas, and water) flows into the wellbore and a "kick" is induced. As a result, a higher mud pressure has to be applied to the wellbore and stops the uncontrolled influx. In complex geological settings, compaction disequilibrium and hydrocarbon generation can cause abnormal pore pressure, where pore pressure is abnormally higher than hydrostatic pressure (Zhang 2011). Therefore, extensive pore pressure analyses should be performed before, during, and after drilling to ensure a safe MWW for annular pressures.

Wellbore stability analysis became an active area of research as the exploration and production industry attempted to extend the lateral reach with a high deviating angle to reach remote pay zones, with an objective to mitigate shear failure of the wellbore, such as breakout or wellbore collapse. Upon the creation of a free surface (the wellbore wall), principal stresses align with the radial and tangential directions at the surface. If no external traction applies to the wellbore, compressive stress is strongly amplified at the wellbore

wall in two symmetrical spots aligned with the azimuth of minimum horizontal stress, which leads to shear failure (i.e., breakout) in the vicinity of those spots (Zoback 2010). To mitigate shear failure, maintaining the mud weight above shear failure gradient (SFG) applies an external traction to the wellbore circumference and reduces compressive stress in the vicinity. SFG can be analytically calculated from the elastic solution of a borehole (Bradley 1979), along with a preferred failure criterion such as Mohr-Coulomb (Fjaer et al. 2008), modified Lade (Ewy 1998), Drucker-Prager (Bradley 1979), etc. Aside from the conventional techniques, the influence of anisotropic strength of rocks and fluid penetration into permeable zones needs to be considered when drilling a deviated wellbore (Zoback 2010). The minimum requirement of mud weight has to be greater than the SFG to ensure wellbore stability.

Mud weight is proportional to the hydrostatic pressure applied to the wellbore surface. When circulating drilling fluid inside annulus to the surface, a higher mud pressure appears in the wellbore, and equivalent circulating density (ECD) is used to characterize mud pressure. This term in particular accounts for the annulus frictional pressure losses that cause the addition of EMW to original mud weight. Meanwhile, if mud outflow is limited at the surface, EMW should consider annulus backpressure along with ECD.

As shown in Figure 2.1, tensile failure occurs at the wellbore if EMW (mud pressure) is higher than fracture gradient and defines the upper limit of the safe MWW. The wellbore initially experiences "borehole ballooning/ breathing," which is the frequent reopening of microfractures at the wellbore. No severe mud loss happens under this condition, but a fracture closure pressure can be possibly observed from annulus pressure when pumps are shut off. Lost circulation occurs when mud pressure reaches the formation breakdown pressure and when hydraulic fracture propagates into the formation. By losing a large volume of mud into the formation, the hydrostatic head is reduced inside the annulus,

and a subsequent kick can be simultaneously triggered when mud pressure is below pore pressure at certain depths. Lost circulation happens not only during a drilling process, but also when cementing and completing the wellbore. In general, seepage loss is inevitable, and severe loss is preventable and remediable with understanding of current techniques.

Lost circulation in a naturally fractured or vugular formation is very different from the mud loss described in the previous paragraph. As the wellbore penetrates such a formation, a massive void space instantaneously triggers fluid loss such that conventional mitigation techniques do not work or are too expensive. To cure these extreme cases, drilling engineers often implement the "pressurized mud cap drilling" technique, which utilizes water as a sacrificial drilling fluid to manage downhole pressure and intentionally injects all the drilling fluid, cuttings, and kick fluid into the formation. Therefore, lost circulation in a naturally fractured formation is not discussed in this thesis.

2.2 STRESS CONCENTRATION AROUND THE WELLBORE

The excavation of rock material perturbs the stress field in the near-wellbore region. As explained, the detached material is no longer available to sustain in-situ stresses, and principal stresses align with the wellbore wall after the wellbore is drilled. Meanwhile, the mud pressure, which is different from the original stress, acts as an external traction at the wellbore wall and causes a redistribution of stress. Thus, stress concentration appears around the wellbore. Ernst G. Kirsch derived the solution of stress distribution around a cylindrical opening of an isotropic, elastic medium in 1898. Later, Bradley (1979) modified Kirsch's solution and introduced the first analytic borehole stability analysis for an arbitrarily deviated wellbore. Determining the stress state in the vicinity of the wellbore involves rotating and transforming the stress tensor, as shown in Figure 2.2. Assuming

linear elasticity, the method to calculate the stress state in a cylindrical coordinate system is utilized to validate the numerical model in this thesis and is illustrated below.

The principal stress ($S_1 > S_2 > S_3$) tensor is given by:

$$S_s = \begin{bmatrix} S_1 & 0 & 0 \\ 0 & S_2 & 0 \\ 0 & 0 & S_3 \end{bmatrix}$$

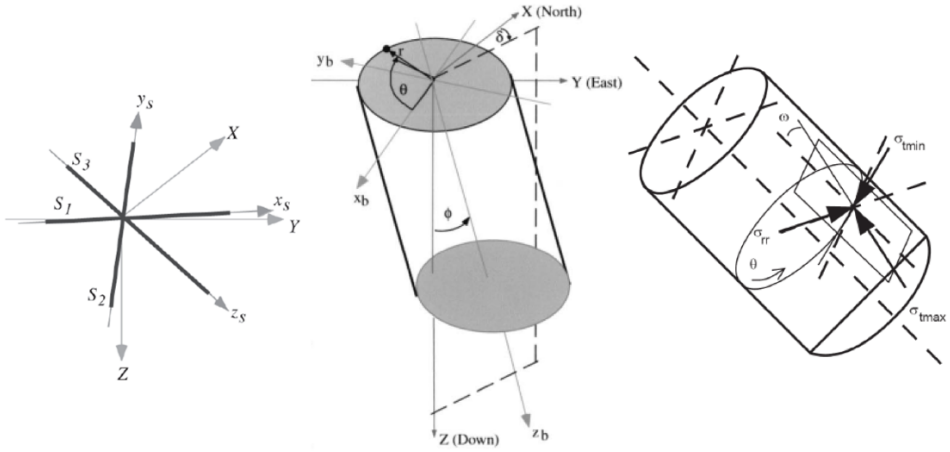

Figure 2.2: Coordinate systems used in calculating the stress state around the wellbore. (modified from Peska and Zoback 1995)

α, β, and γ are the Eulerian angles defining the rotation of principal stress tensor to the geographic coordinate system. δ is the azimuth of the wellbore measured clockwise from geographic north, and ϕ is the deviation of the wellbore with respect to the vertical direction. They define stress tensor rotation from the geographic coordinate system to the wellbore coordinate system. S denotes the total stress, and σ denotes the effective stress.

	$\boldsymbol{S_V > S_{H,max} > S_{h,min}}$	$\boldsymbol{S_{H,max} > S_V > S_{h,min}}$	$\boldsymbol{S_{H,max} > S_{h,min} > S_V}$
$\boldsymbol{\alpha}$ $\boldsymbol{(0° \; to \; 360°)}$	azimuth of $S_{h,min}$	azimuth of $S_{H,max}$	azimuth of $S_{H,max}$
$\boldsymbol{\beta}$ $\boldsymbol{(-90° \; to \; 90°)}$	$-90°$	$0°$	$0°$
γ $\boldsymbol{(0° \; to \; 360°)}$	$0°$	$90°$	$0°$

Table 2.1: Eulerian angles for various stress regimes.

$$R_s=\begin{bmatrix} \cos\alpha\cos\beta & \sin\alpha\cos\beta & -\sin\beta \\ \cos\alpha\sin\beta\sin\gamma-\sin\alpha\cos\gamma & \sin\alpha\sin\beta\sin\gamma+\cos\alpha\cos\gamma & \cos\beta\sin\gamma \\ \cos\alpha\sin\beta\cos\gamma+\sin\alpha\sin\gamma & \sin\alpha\sin\beta\cos\gamma-\cos\alpha\sin\gamma & \cos\beta\cos\gamma \end{bmatrix}$$

$$R_b=\begin{bmatrix} \cos\delta\cos\phi & \sin\delta\cos\phi & -\sin\phi \\ -\sin\delta & \cos\delta & 0 \\ \cos\delta\sin\phi & \sin\delta\sin\phi & \cos\phi \end{bmatrix}$$

$$S=R_bR_s^TS_sR_sR_b^T$$

$$S_{rr}=\left(\frac{S_{11}+S_{22}}{2}\right)\left(1-\frac{{r_w}^2}{r^2}\right)+\left(\frac{S_{11}-S_{22}}{2}\right)\left(1+\frac{3{r_w}^4}{r^4}-\frac{4{r_w}^2}{r^2}\right)\cos 2\theta+S_{12}\left(1+\frac{3{r_w}^4}{r^4}-\frac{4{r_w}^2}{r^2}\right)\sin 2\theta+P_w\frac{{r_w}^2}{r^2}$$

$$S_{\theta\theta}=\left(\frac{S_{11}+S_{22}}{2}\right)\left(1+\frac{{r_w}^2}{r^2}\right)-\left(\frac{S_{11}-S_{22}}{2}\right)\left(1+\frac{3{r_w}^4}{r^4}\right)\cos 2\theta-S_{12}\left(1+\frac{3{r_w}^4}{r^4}\right)\sin 2\theta-P_w\frac{{r_w}^2}{r^2}$$

$$S_{zz}=S_{33}-2v(S_{11}-S_{22})\frac{{r_w}^2}{r^2}\cos 2\theta-4vS_{12}\frac{{r_w}^2}{r^2}\sin 2\theta$$

$$S_{r\theta}=-\left(\frac{S_{11}-S_{22}}{2}\right)\left(1+\frac{2{r_w}^2}{r^2}-\frac{3{r_w}^4}{r^4}\right)\sin 2\theta+S_{12}\left(1+\frac{2{r_w}^2}{r^2}-\frac{3{r_w}^4}{r^4}\right)\cos 2\theta$$

$$S_{\theta z}=(-S_{13}\sin\theta+S_{23}\cos\theta)\left(1+\frac{{r_w}^2}{r^2}\right)$$

$$S_{rz}=(S_{13}\cos\theta+S_{23}\sin\theta)\left(1-\frac{{r_w}^2}{r^2}\right)$$

The above equations assume positive compressive stress. The effective stress law considers the effect of pore pressure as follows:

$$\sigma_{ij}=S_{ij}-\delta_{ij}\alpha_P P_p$$

Assuming no pore pressure perturbation, modifying the above equations to calculate the effective stress at the wellbore wall yields:

$$\sigma_{ZZ}=\sigma_{33}-2v(\sigma_{11}-\sigma_{22})\cos 2\theta-4v\sigma_{12}\sin 2\theta$$

$$\sigma_{\theta\theta}=\sigma_{11}+\sigma_{22}-2(\sigma_{11}-\sigma_{22})\cos 2\theta-4\sigma_{12}\sin 2\theta-(P_w-P_P)$$

$$\tau_{\theta Z}=2(\sigma_{23}\cos\theta-\sigma_{13}\sin\theta);\ \tau_{r\theta}=\tau_{rz}=0$$

$$\sigma_{rr}=P_w-P_P$$

2.3 WELLBORE FRACTURING

Hydraulic fracturing of the wellbore has become a must-have in rock-mechanic-related textbooks (Jaeger et al. 2007, Fjaer et al. 2008, Zoback 2010, Yew and Weng 2014). Severe lost circulation events are unplanned and occur when excessive mud pressure induces fractures or reopens natural fractures at the wellbore and then propagates into the formation. Therefore, the mechanisms of hydraulically fracturing the wellbore are the basis for lost circulation analysis. In this section, a formation strength test (FST) is introduced first to illustrate a macroscopic schematic of hydraulically fracturing the wellbore. Then, fracture initiation and fracture propagation are detailed, discussed with practical consideration of drilling environment to advance familiarity with the underlying mechanisms.

2.3.1 Understanding Leak-Off Test

FSTs are small-scale hydraulic fracturing practices frequently performed during drilling operations. FST is a generic name for a range of pressure testing operations, including leak-off test (LOT), extended leak-off test (XLOT), etc. For simplicity of nomenclature, LOT is used to refer to FST in the rest of this thesis. By plotting surface pressure or downhole pressure versus time or injected volume, each of the characteristic points from the plot reveals a different physical process that is ongoing during wellbore hydraulic fracturing. Therefore, a review of LOT is inevitably necessary in analyzing induced fracture behavior during lost circulation. Multiple literature sources have presented an artificially composed LOT figure to demonstrate the schematic of LOT. All are very similar, so an intelligible LOT plot is chosen based on the author's personal preference.

Figure 2.3 assumes a vertical, intact borehole undergoing a normal faulting stress regime and constant pumping rate. By pumping drilling fluid into the wellbore and

restricting outflow, the fluid pressure applied at the wellbore ramps up and reduces the compressive hoop stress (tangential stress) at the wellbore that is originally generated by in-situ stresses. When hoop stress reaches the tensile strength of the rock at the azimuth of maximum horizontal stress, a small fracture is initiated. By continuous pumping, the fracture propagates abruptly into the formation at a critical moment, at which point fluid from the borehole rushes into the newly created fracture and causes a sudden drop in fluid pressure. At this moment, the maximum fluid pressure of the plot is the formation breakdown pressure. However, when the above assumptions are not met, this "peak pressure" is possibly not observed. The propagation pressure plateau indicates that the fracture propagates into the formation. In this period, fluid leaks off into the permeable formation, and the net pressure, which is the fluid pressure minus the minimum in-situ stress, sustains the fracture opening. When pumps are shut off, an instantaneous shut-in pressure is seen, and the amount of change from propagation pressure is the frictional pressure loss from the surface to the fracture tip. By continuously monitoring pressure response, the pressure declines due to the fluid leak-off and fracture closure. In theory, the fracture closes when the fluid pressure inside it equals the minimum in-situ stress. Overall, the processes described above are the fundamental mechanisms for all kinds of FSTs.

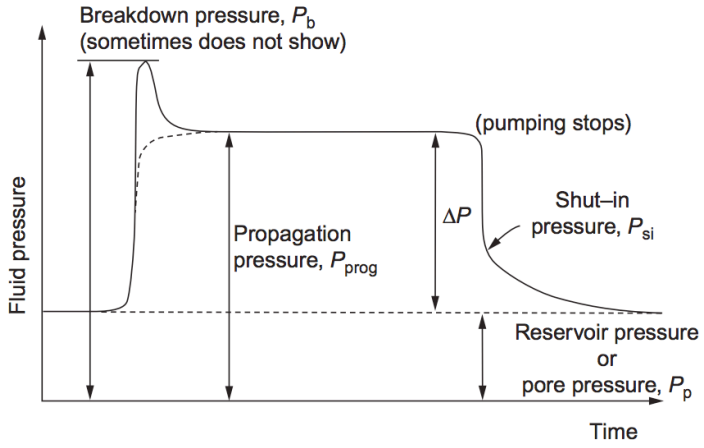

Figure 2.3: A typical downhole pressure record of leak-off test. (Yew and Weng 2014)

A typical field application of LOT is to evaluate the mechanical strength of the casing shoe to determine the maximum pressure it can withstand. This pressure is necessary for selecting mud weight, estimating kick tolerance, and designing the subsequent casing setting depth for drilling the new hole section. Also, knowing the mechanism of fracture closure, LOT reasonably estimates minimal in-situ stress, which is an input parameter for all kinds of well completion design. Noting the inexistence of breakdown pressure, the complexity of testing conditions at the field is far beyond the scope of the assumptions a model can make. Considerable efforts to enhance LOT analysis have been made in the past. Overall, the deviation of field testing results compared to the ideal condition is generally due to testing methodology, drilling fluid compressibility, wellbore mechanical expansion, fluid leakage, drilling fluid properties, induced or natural fractures, and downhole conditions. Operational personnel can refer to constructive discussions and conclusions available in the literature to enhance interpretation (Postler 1997, Okland et al. 2002, van Oort and Vargo 2008, Alberty and McLean 2014).

2.3.2 Fracture Initiation

Conventional fracture gradient analysis assumes a vertical, intact, and impermeable wellbore. Fracture initiation can then be interpreted by the Hubbert-Willis (1957) expression, which is derived from Kirsch's solution, when the effective hoop stress at the wellbore surface equals the tensile strength of the rock.

$$p_{ini} = 3S_{hmin} - S_{Hmax} - P_P + T \tag{2.1}$$

where p_{ini} is the FIP; S_{hmin} and S_{Hmax} are the minimum and maximum horizontal stresses; P_P is the pore pressure; and T is the tensile strength. Equation 2.1 only applies to cases where a perfect impermeable cake forms at the wellbore wall or where formation rock is impermeable. However, if pore pressure increases due to fluid invasion from the

wellbore to the formation, the effective stress at the wellbore becomes more tensile and the required mud pressure to initiate fracture decreases. Haimson-Fairhurst (1967) presented a more general model incorporating fluid infiltration into the permeable and poroelastic borehole wall.

$$p_{ini} = \frac{3S_{hmin} - S_{Hmax} - 2\eta P_P + T}{2(1-\eta)} \tag{2.2}$$

$$\eta = \frac{\alpha_P(1-2v)}{2(1-v)}$$

where η is the poroelastic parameter of the rock, which characterizes the magnitude of the stress induced by fluid penetration. It ranges from 0 for no fluid penetration to 1 for unimpeded penetration. Schmitt and Zoback (1989) observed from hydraulic fracturing experiments that Biot's poroelastic parameter varies by pore structure and rock composition such that pore pressure has less effect on reducing the tensile stress at which failure would be expected. A further modified equation accounts for the experimental validations of non-Terzaghi effective stress law as follows:

$$p_{ini} = \frac{3S_{hmin} - S_{Hmax} - 2\eta P_P + T}{1+\beta-2\eta} \tag{2.3}$$

where β is the effective stress coefficient for tensile failure. Overall, all three methods indicate the intrinsic relationship among FIP, stress anisotropy, and pore pressure, where FIP decreases with an increase in stress anisotropy and an increase in pore pressure. However, these relationships have to be carefully examined because horizontal stresses are also a function of pore pressure and overburden stress.

For a wellbore with microfractures or natural fractures, Kirsch's elastic solution, which is the continuum mechanics approach, is no longer valid. A fracture mechanics approach should be utilized to estimate fracture reopening, and propagation pressure for the pre-existing fractures should replace the FIP that often defines the fracture gradient in

conventional fracture gradient analysis. Lee et al. (2004) presented an analytical solution for propagating a fracture from a wellbore:

$$p_{ini} = \frac{3S_{hmin} - S_{Hmax}}{2} - \frac{K_{IC}}{\pi\sqrt{2L}} \tag{2.4}$$

This linear elastic fracture mechanics (LEFM) model solves for the smooth fracture closure at the tip under the Barenblatt condition, which assumes a mobile equilibrium between the positive stress intensity factor produced from fracture fluid and the negative stress intensity factor produced from compressive horizontal stress. Feng et al. (2016) implemented this equation in dimensionless form and presented the influence of each term in Equation 2.4 to the FIP.

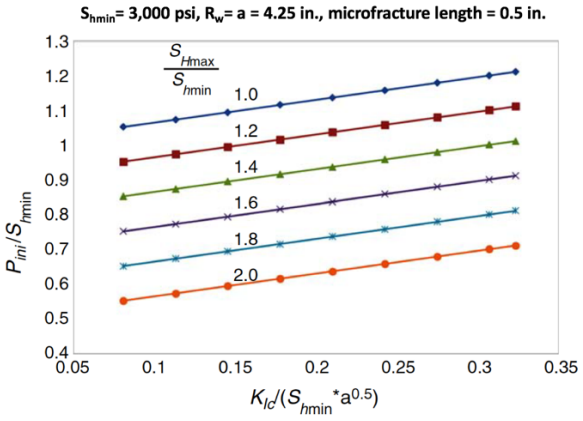

Figure 2.4: Dimensionless fracture initiation pressure at a wellbore with microfractures (Feng et al. 2016)

Figure 2.4 shows FIP decreasing with an increase in stress anisotropy and a reduction in fracture toughness; FIP is possibly smaller than minimum horizontal stress when stress anisotropy is high and fracture toughness is low; with a fracture length of about 10% of the wellbore, FIP is far below the minimum horizontal stress.

For ideal cases, LOT leak-off pressure, the first inflection point of the pressure ramping up, indicates the fracture's initiation at the wellbore. However, this phenomenon is not always true, especially when high-solids-content drilling fluid is utilized. Once a

short fracture is initially induced, the microfractures may be soon sealed by a filter cake formed by mud solids, such that the observable "leak-off pressure" may instead be the rupture pressure of the filter cake rather than the FIP of an intact wellbore (Feng et al. 2016). Until formation breakdown, this sealing and breaking process of the mud cake could repeat during the initial fracture propagation. Consequently, multiple leak-off points (or no obvious leak-off point) are possibly recorded. Guo et al. (2014) experimentally found that fractures can grow significantly without any clear leak-off signature.

Aadnoy et al. (2008) experimentally studied the fracture resistance provided by filter cake. They emphasized the mechanical strength of filter cake that dictates the plastic deformation during the fracture initiation. The rupture of filter cake is expected to be controlled by cake strength and thickness, cake bonding to the wellbore wall, cake particle-size distribution (PSD), and the opening of the fracture at the wellbore (Cook et al. 2016).

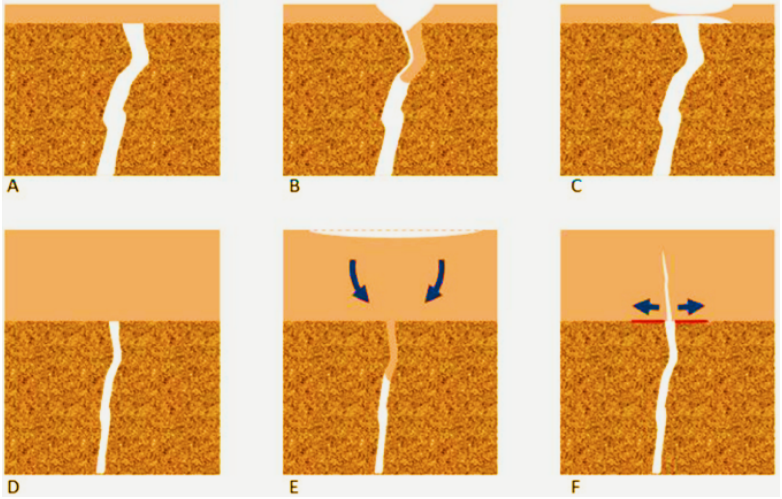

Figure 2.5: Schematic of the filter cake mechanical behavior over a crack opening. (A) and (D) show a thin cake over a wide crack and a thick cake over a narrow crack, respectively. From (B) and (E), wellbore pressure can punch a hole through a thin cake and will extend the thick cake laterally, making it rather difficult to squeeze the material into the crack. (C) and (F) show the response to stretching the cake, where thin cake is pulled apart and a crack must propagate upward from the fracture mouth within the thick cake. (Cook et al. 2016)

2.3.3 Fracture Propagation

In theory, there are three modes of propagating a crack: opening, sliding, and tearing. This study only considers the opening mode (also called Mode I crack). In LEFM, Mode I stress intensity factor K_I examines the fracture stability.

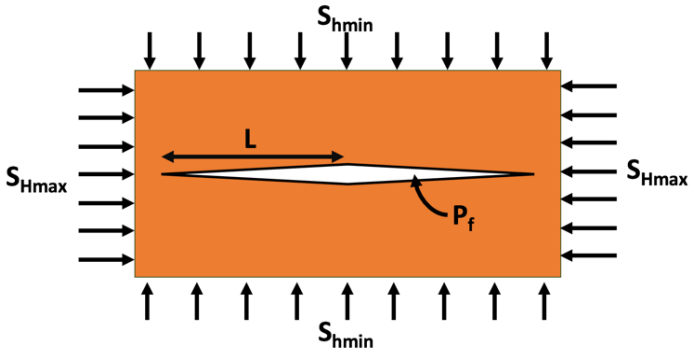

Figure 2.6: A bi-wing hydraulic fracture in an infinite plate under the action of in-situ stresses.

For estimating the Mode I stress intensity factor of an edge crack propagating in the maximum horizontal stress direction in a linear elastic infinite plate that is subjected to heterogeneous in-situ stresses (as shown in Figure 2.6), a closed-form solution (modified from Anderson 2005, Yew and Weng 2014) follows:

$$K_I = 1.12(P_f - S_{hmin})\sqrt{\pi L} \tag{2.5}$$

where P_f is the fluid pressure applied at the fracture surface, S_{hmin} is the minimal horizontal stress, L is the fracture length of one of the fracture wings, and the unit of intensity factor is $\text{stress}\times\sqrt{length}$. The fracture propagates when K_I reaches the critical stress intensity factor or the fracture toughness, K_{Ic}. The fracture toughness of rock can be obtained from the experiment or numerical analysis. In Equation 2.5, the stress intensity factor is proportional to the fracture length and the difference between P_f and S_{hmin}. When fracture length is long, an extremely small fracture fluid pressure in excess of the minimal horizontal stress is enough to make K_I=K_{Ic} and drives fracture propagation.

Therefore, fracture toughness primarily dominates the initiation and initial extension of the fracture, where the fracture length is small. This phenomenon can be observed from the LOT data. Before formation breakdown, fracture length is short and is mostly affected by fracture toughness. After formation breakdown, the fracture propagates in an unstable manner, where fracture volume enlarges at a greater rate than pump rate.

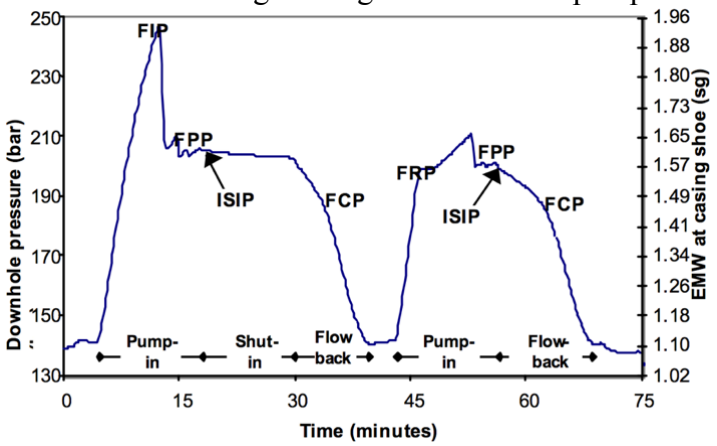

Figure 2.7: Field data of an extended leak-off test. (Okland et al. 2002)

Wellbore pressure then drops to FPP due to the sudden enlargement of fracture volume (as shown in Figure 2.7). FPP decreases as fracture size increases due to the smaller excess pressure required to keep the fracture open, as well as the larger fracture perimeter has a higher probability of finding the weak point to propagate (Okland et al. 2002). When the fracture is large enough, FPP is just above the least principal stress. According to the theory of LEFM, a fracture propagates when the stress intensity at the tip reaches the fracture toughness of the rock. Assuming an incompressible fluid and constant rate of injection, after the fracture extends for a distance, the stress intensity factor at the new tip has to build up and generates additional propagation until reaching the fracture toughness in order to propagate the fracture further. This explains the wave-like (or step-by-step) decreasing pattern of the FPP, which can be seen in Figure 2.7.

As mentioned in the fracture initiation section, the solids content of drilling fluid can distort the FIP from the theoretical prediction. Solids are carried into the fracture and plug it by forming an internal cake. This cake limits the fluid flow toward the tip and reduces the fluid pressure inside the fracture. Ultimately, the cake restricts buildup of the stress intensity factor at the tip and increases the FPP. This phenomenon can be pronounced during the initiation and early extension of the fracture when a "tough" filter cake exists at the wellbore wall, and it requires a high pressure to rupture the cake and restricts fluid seepage across it into the fracture. Subsequently, the fluid that enters the fracture quickly leaks into the formation rock, fracture fluid pressure is equivalent to formation pore pressure, and stress intensity at the tip has minor buildup.

Fluid leak-off into the formation increases the FPP. Permeability, pore pressure, wettability, capillary entry pressure, and solid plug at the rock surface dictate hydraulic conductivity of the rock and can affect the rate of leak-off. For an impermeable rock, very limited hydraulic energy can dissipate into the formation rock, most of it flowing toward the fracture tip to propagate the fracture, in which fluid's fracturing efficiency is high for impermeable rock compared to the fracturing of a permeable one. For a permeable rock, fluid penetration at fracture surface elevates pore pressure in the vicinity. In the theory of poroelasticity, elevated pore pressure expands the porous medium, which induces more compressive stress (i.e., poroelastic backstress) that acts on the fracture surface, tends to close the fracture, and inhibits fracture growth (Wang 2016). On the other hand, forming the mud cake requires a certain volume of fluid leak-off and could provide additional resistance in fracture propagation. Overall, dominated by the hydraulic conductivity, fluid leak-off into the formation reduces the chance of fracture propagation, and the resulting pore pressure elevation tends to increase poroelastic backstress impeding fracture growth.

2.4 LOST CIRCULATION AND WELLBORE STRENGTHENING

Lost circulation is the loss of drilling fluid into rock formation during drilling operations. As a result, the rate of mud returning at the annulus side is less than the rate of mud pump-in at the drillpipe side.

Present drilling activities often take place in complex geological settings and require advanced mud formulation to handle the technical difficulty driven from the rock physical and chemical properties. The cost of drilling fluid can be easily beyond USD 100/bbl, and lost circulation adds even further expenditure beyond that planned.

Mud loss can reduce the hydrostatic head inside the annulus. For a severe lost circulation event, this reduction can be significant, such that mud pressure along the wellbore is inadequate to maintain wellbore stability and to balance pore pressure. Immediate actions have to be taken for the safety of the drilling operation. Therefore, lost circulation extends drilling operation nonproductive time because the consequent "chain-reaction" must be resolved, such as fluid influx, underground blowout, stuck pipe, unplanned casing points, sidetracks, failure to reach target depth, etc. The cost of nonproductive time can be 1 to 3 million USD per day for a deepwater operation. Therefore, the cost of lost circulation is substantial for today's cost-demanding operations.

When circulating drilling fluid to the surface or when tripping drillstring, friction pressure gives rise to ECD, and the wellbore experiences mud pressure fluctuation. Moreover, this variation increases as the well deepens, creating more risk of exceeding the MWW. In fact, lost circulation typically occurs in a narrow MWW, such as with depleted reservoir, overpressured formation, deviated wellbore, and naturally fractured formation. Early evaluation of such a drilling environment can reveal the inaccessibility of the target formation and stop the drilling.

WBS techniques, which have seen significant advancement in the last 20 years, have been utilized successfully to artificially elevate the effective fracture gradient and ultimately extend the MWW. In fact, WBS only offers superior benefits for permeable formation in resolving lost circulation. Different from its literal meaning, WBS contributes additional resistance to the fracture so that an ECD higher than the conventionally estimated fracture gradient can be exerted on the wellbore. In all kinds of WBS techniques, LCM, composed of engineered solid particles, is blended and circulated within the drilling mud. Even though there are particles from the mud itself and the rock cuttings, drilling engineers customize the sizes of LCM, considering the geometry of natural fractures and the induced fractures at the wellbore. With this in mind, WBS methods require transporting and depositing LCM at the fracture space.

Two main types of WBS techniques are currently adopted in drilling operations: the hoop stress enhancement method (e.g. stress cage) and the fracture resistance enhancement method (e.g., fracture propagation resistance). Within these two types, different WBS models also hold very different interpretations on the process for LCM placement and underlying mechanisms. Thus, each model lays out a distinctive operational recommendation and is uniquely supported by its own mathematical model and pilot validations. Various representative studies are categorized into two main types and are presented in the following sections.

2.4.1 Hoop Stress Enhancement Method

Hoop stress is known as the tangential component of the stress tensors along the wellbore circumference. The purpose of the hoop stress enhancement method is to increase apparent fracture resistance by depositing LCM at the fracture, forming an immobile mass. The motivation of this method is that a fractured wellbore is essentially held closed by hoop stress, and applying displacement at the fracture surface modifies the near-wellbore stress, which requires a higher ECD equal to the elevated hoop stress to open and propagate the fracture (as shown in Figure 2.8).

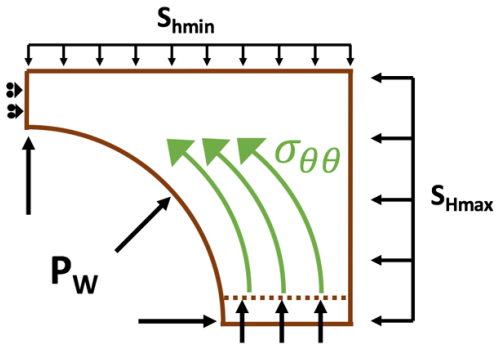

Figure 2.8: A schematic of hoop stress enhancement for one-quarter of the wellbore with a partial fracture at the bottom. Boundary conditions are in black. The dotted line indicates the displacement of the fracture surface after enhancement.

Alberty and McLean (2004) introduced a physical model for stress cages. As shown in Figure 2.9, a stress cage projects that LCM deposits near the fracture mouth act as a proppant and as a seal to isolate the majority of a fracture from wellbore pressure.

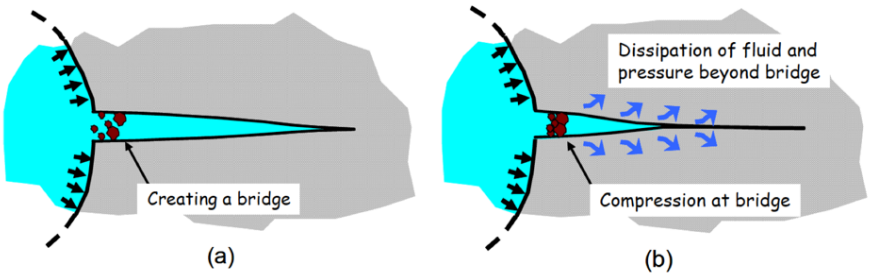

Figure 2.9: Stress cage process. (Modified from Alberty and McLean 2004)

LCM is deposited near the fracture mouth and props open the fracture mouth (Figure 2.9a). Then, as fracture fluid pressure equilibrates to formation pore pressure, the isolated part of the fracture tends to close. A two-dimensional (2D) finite-element-based LEFM model was developed to simulate stress cages. This model requires users to predefine fracture length and concentration of LCM. The finite element model confirmed that highly concentric stresses are developed near the plugging location, and the hoop stress around the wellbore can be enhanced if plugging is achieved near the wellbore wall. Corresponding to their numerical model, the authors suggested that stress enhancement is a function of rock stiffness, fracture width, fracture length, plugging location, and compressive strength of the bridging material. From an engineering perspective, this finite element model has been applied in drilling operations to estimate LCM concentrations (depending on particle size) to build the desired fracture resistance. Besides the modeling efforts, experiments conducted on a fixed-fracture device display bridge development near the fracture mouth; field trials also prove the effectiveness of elevating fracture reopening pressure and the feasibility of stress cage as a preventative treatment (Aston et al. 2004).

Dupriest (2005) presented the fracture closure stress (FCS) model and field data validating the treatment. FCS refers to the stress holding fracture faces closed (as shown in Figure 2.10).

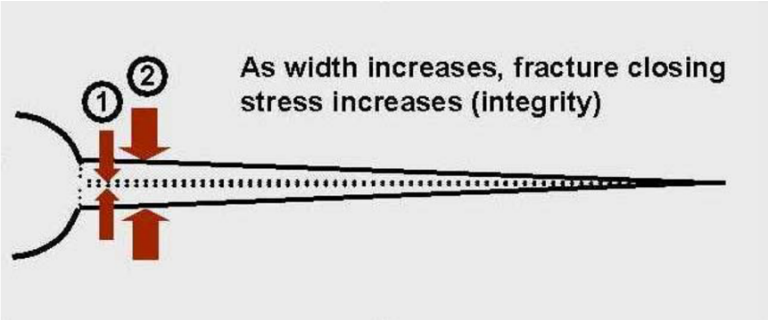

Figure 2.10: Fracture closure stress model. (Dupriest 2005)

This model is a remedial treatment that conducts a series of hesitation-squeezing operations after fluid loss. The objective of this treatment is to maintain isolation of the tip and achieve a final fracture width. Similar to the stress cage, the FCS model indicates the enhancement of the hoop stress, specifically by elevating the fracture closing stress greater than the planned ECD through fracture aperture widening. Differently, FCS emphasizes the needs for fracture tip isolation, which gives rise to a higher differential pressure to transmit pressure to the fracture tip. When fluid pressure near the tip exceeds the least principle stress, the fracture propagates. Dupriest described the particle packing inside the fracture as the immobile mass. He stated that the type of LCM, which composes the immobile mass, is relatively unimportant. Due to the harsh environment experienced through the circulation system to the fracture, LCM strength is also relatively unimportant. However, Dupriest highlighted that fluid leak-off accelerates the development of the immobile mass. Then, the LCM serves primarily as a fluid loss enhancer for the mud. Uniform particle size is recommended to increase matrix seepage losses. Overall, apparent permeability, FCS enhancement, and the differential pressure driving the fluid loss dictate the success of developing the immobile mass and dehydrating the LCM during hesitation squeezing.

Wang et al. (2007, 2009) implemented boundary element analysis to investigate the improvement of wellbore pressure containment (WPC) by propping fractures with particulate LCM to strengthen the wellbore. They defined WPC as wellbore breakdown pressure or FPP, whichever is higher. When lost circulation happens, WPC is exceeded by wellbore pressure. In the authors' model, a 6-in. fracture length, a wellbore radius, and a propping displacement are predefined, and the LEFM theory is assumed to evaluate fracture stability. They found that propping the cracks can elevate the hoop stress above the one calculated from Kirsch's solution; stress anisotropy highly influences stress cage treatment; smaller wellbore radius and higher rock stiffness can offset a larger scale of

treatment required for a wide crack opening; sealing location is recommended to be at the fracture mouth; and fracture sealing that reduces fracture fluid pressure maintains fracture stability.

Ideal WPC	Perfectly circular wellbore with impermeable wellbore wall at reservoir temperature
Weakening WPC	Borehole shape (hydraulically conductive cracks) Rock shrinkage (cooling or water outflow) Increased pore pressure Strength loss
Strengthening WPC	Sealing fractures Propping fractures Rock expansion (chemical or thermal swelling) Reduced pore pressure Rock consolidation

Table 2.2: Summary of wellbore strengthening. (Wang et al. 2009)

Feng et al. (2015) adopted finite element analysis to assess fracture sealing, with further consideration of poroelastic material. Their model, with a 6-in. predefined fracture, illustrated that a high concentration of stress enhancement exists in the vicinity of bridging location and deteriorates as bridging location moves away from the wellbore. Higher stress anisotropy was shown to have higher hoop stress enhancement. Considering pore pressure perturbation, FCS is higher in the poroelastic model. After bridging, fluid leak-off lowers the developed hoop stress enhancement, but, under a different leak-off rate, fracture width is almost the same over a long period of time.

Salehi and Nygaard (2011) stated that WBS can restore hoop stress, but not to its stress state when on an intact wellbore. They claimed that pore pressure perturbation during their “injection” reduces the effective stress, which had not been considered in previous linear elastic models.

2.4.2 Fracture Resistance Enhancement Method

The objective of the fracture resistance enhancement method is to raise the apparent FPP. The solids content in drilling fluids can form a bridge inside the induced fracture aperture. Therefore, different from the previous method, LCM aggregate is employed to prevent the wellbore pressure from transmitting to the fracture tip, which in turn prevents fracture propagation.

The early development of this method was motivated by the joint industry project DEA-13, conducted by the Drilling Engineering Association in the 1980s, to investigate the fundamental mechanism of lost circulation with oil-based drilling fluid. Onyia (1994) and Morita et al. (1996) later described the experiments. A total of 35 fracturing experiments were conducted on 30×30×30-in. Berea and Torrey sandstone blocks and 20.5×30-in. Mancos shale cores. The blocks were subjected to confining pressures of 3000 psi vertically and 1800 psi and 2200 psi horizontally. With a predrilled 1.5-in. borehole, low- (10-ppg) and high- (16-ppg) density diesel, water- and mineral-oil-based muds were injected at 0.2 to 2.5 cm^3/s in four steps to (1) achieve wellbore breakdown; (2) reopen the fracture; (3) test the healing effect of drilling fluids after waiting for 1 hour; and (4) create a new fracture perpendicular to the original crack by altering the confining pressures. Then, fracture initiation, propagation, and reopening were captured from the pressure response and split samples were visually inspected. The published results and analysis of DEA-13 (Onyia 1994) suggested that FIP is independent of mud type (as shown in Figure 2.11); high-density, water-based mud (WBM) exhibits higher FPP than oil-based mud (OBM); WBM generates a thicker cake inside the fracture and a higher fracture reopening pressure; the most effective LCM treatment for oil-based, mud-induced fractures in permeable rocks is a high-fluid-loss, WBM pill; and the main difference between high-density OBM and WBM with respect to their lost circulation inducement lies in their reopening and

propagation pressures (i.e., the upper peak points of the "saw-tooth" propagation pressures shown in Figure 2.11). Remarkably, DEA-13 established the basis for the development of the fracture resistance enhancement method.

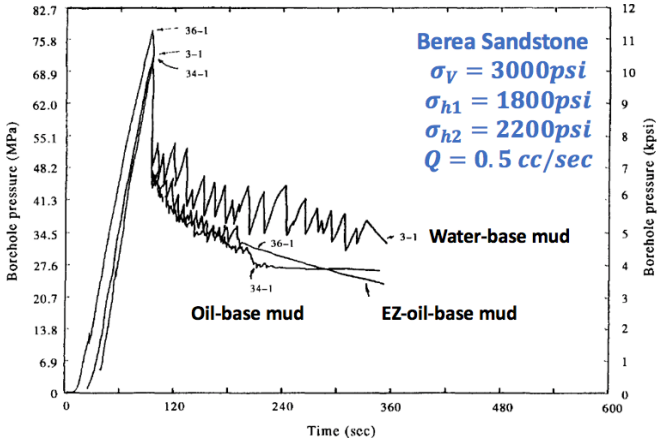

Figure 2.11: Comparison of mud types from DEA-13. (Modified from Morita et al. 1996)

Based on experimental observations, the "tip screen-out" model (as shown in Figure 2.12) was proposed (Morita et al. 1990, Fuh et al. 1992, Morita et al. 1996).

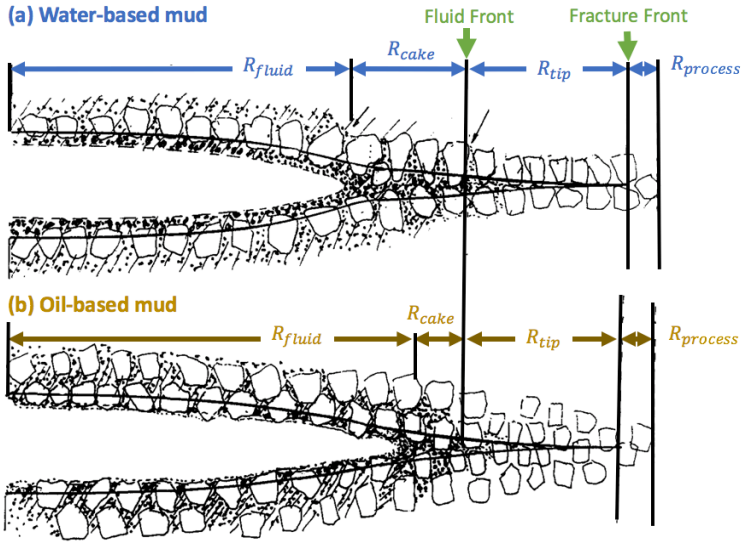

Figure 2.12: Fracture propagation in water-based mud showing a larger dehydrated zone (i.e., external cake), R_{cake}, than oil-based mud. In the case of oil-based mud, internal cake is predominantly developed. (Modified from Morita et al. 1990)

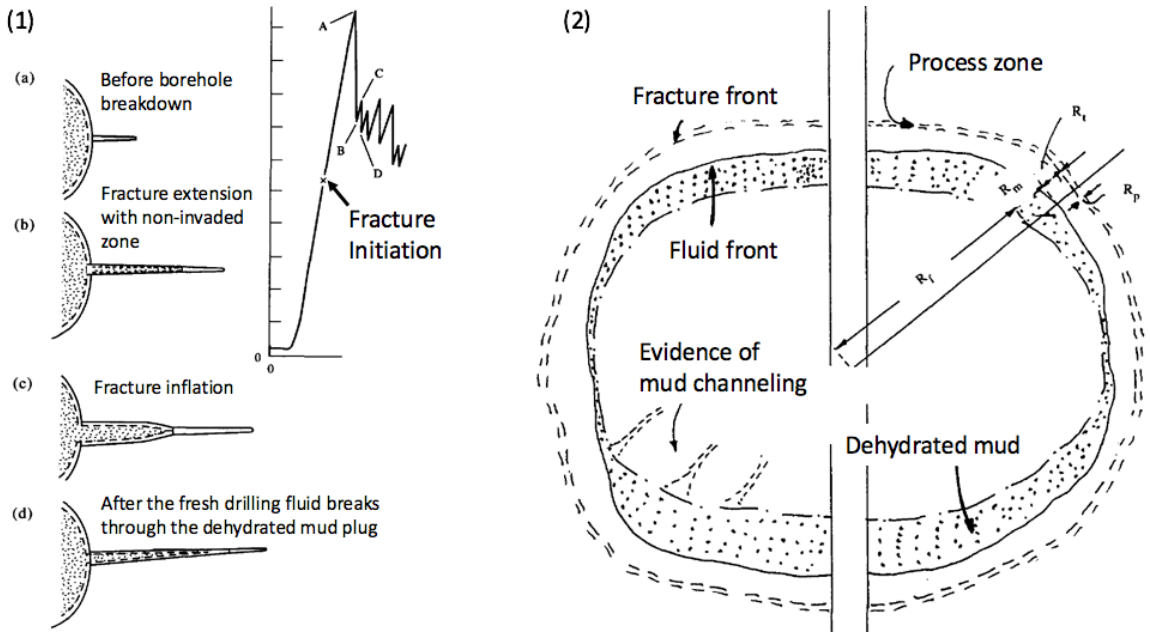

Figure 2.13: (1) Typical sequence of fracture extension for water-based mud. (2) Side view of mud cake formed in a fracture. (Modified from Morita et al. 1996)

Visually inspecting the split sample, three zones are observed (as shown in Figure 2.13.2): (1) the non-invaded zone, where narrow fracture width inhibits fluid penetration, (2) the mud dehydrated zone, where solids concentration is high due to screen-out, and (3) the fractured zone, where mud is mobile. Solids aggregation at the dehydrated zone is believed to respond to increasing propagation resistance (i.e., pressure fluctuation) in WBM, which has better dehydration ability than OBM. The dehydrated zone isolates the fracture tip from the wellbore pressure, so the fracture propagates at a higher pressure when the wellbore pressure breaks through the cake and transmits to the fracture tip (as shown in Figure 2.13.1.c). Instead, OBM is designed to control fluid loss by using an invert emulsifier to generate internal filter cakes. This contributes to a lower and smoother propagation pressure of OBM compared to WBM. Overall, a significant increase in formation fracture resistance can be achieved by the screen-out effect, resulting in solid particle content of drilling fluids.

Fuh et al. (1992, 2007) presented theoretical formulations and successful field trials using loss prevention material (LPM) as a preventive treatment continuously performed during drilling operations. Remarkable improvements in borehole breakdown pressure and FPP were achieved by implementing LPM in permeable formations. The authors suggested that optimal LPM should have a large and uniform size to provide sealing capacity after being packed, to be easily handled, and to not alter the mud properties. Suitable LPM concentration and size, a certain degree of filtrate loss, and a quick screen-out process are critical for propagation resistance treatment. Morita and Fuh (2012) assessed multiple WBS methods and concluded that the effectiveness of all treatments depends on width and concentration of plugging materials, Young's modulus, wellbore size, and in-situ stress; preventive lost circulation methods are effective for stabilizing micro- and macrocracks; and the stress cage method theoretically works for all rocks, but has limits with placing the LCM and maintaining fracture stability during the squeezing treatment.

The GPRI 2000 project replicated DEA-13 with smaller-scale fracture tests (van Oort et al. 2011). It suggested that coarse particles and finer particles are both needed to bridge fracture and reduce particle aggregation permeability, respectively (Razavi et al. 2015).

Kaageson-Loe et al. (2009) investigated the fracture sealing ability of particulate-based LCM and illustrated the hypothesis of fracture sealing mechanism (as shown in Figure 2.14). A pair of artificial, porous plates (5×0.5-in.) was used in a fracture testing device. Results show that "fracture plugging" provides the most competent seal and strength of sustained high fluid pressure. To achieve fracture plugging, a certain concentration is required for particles larger than fracture aperture. Frictional resistance holding the LCM aggregation in place and fluid loss characteristic of LCM were mentioned as important in forming the fracture seal.

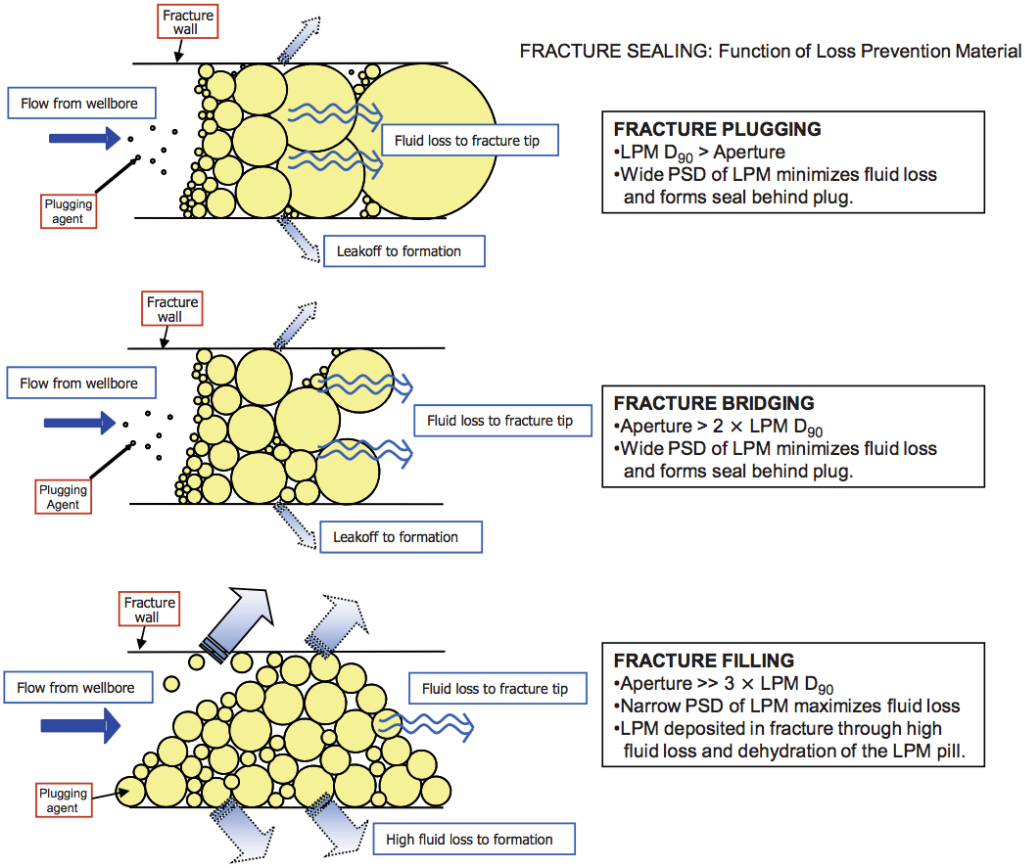

Figure 2.14: Illustration of fluid-loss-control mechanism for particulate-based loss prevention material. Particle-size distribution, relative fracture aperture, fluid leak-off at fracture surface, and fluid loss to the fracture tip affect the final fracture seal. Fracture plugging and bridging are design criteria for low fluid loss (i.e., fracture or formation is rapidly plugged and sealed). Fracture filling is the design criterion for high fluid loss (i.e., loss prevention material dehydration prior to forming the fracture seal). (Kaageson-Loe et al. 2009)

Guo et al. (2014) presented conclusions drawn from hundreds of tests on WBS. They suggested that PSD, size, and LCM concentration with respect to fracture apertures are critical in delivering WBS benefit. Preventive treatment with low-concentration LCM (depending on fracture aperture) is more effective than a remedial treatment with a higher concentration. Fracture sealing is mostly observed near the wellbore, and the filter cake is critical for WBS treatment.

Van Oort et al. (2011) proposed the fracture propagation resistance model, mostly based on the investigation of DEA-13. Fracture propagation resistance possesses the same underlying mechanism as Morita and Fuh's model, but with different justification. Experiments were conducted on Berea sandstone cores and Mancos shale cores (4-in. diameter and 6-in. length) to validate fracture propagation resistance. They suggested that the effect of optimum PSD overrides the effect of LCM type in providing fracture propagation resistance (Razavi et al. 2015). More specifically, Figure 2.15 shows that LCM with bimodal PSD achieves the best FPP enhancement.

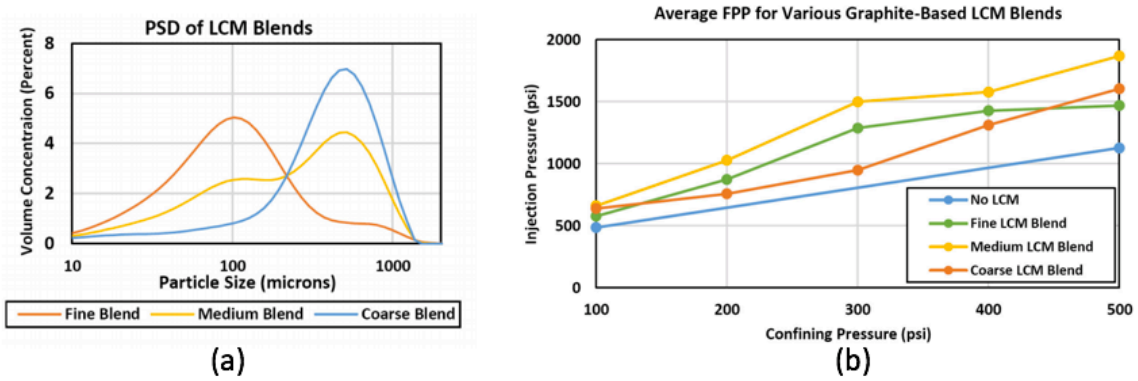

Figure 2.15: (a) Particle-size distribution of different blends. (b) Effect of lost circulation material particle-size distribution on fracture propagation pressure. (Razavi et al. 2015)

Experiment results also indicated that an LCM-concentration threshold exists in elevating FPP and excessive fluid injection inversely reduces FPP. Thus, small-volume squeezing is recommended. Furthermore, thin-section analysis located fracture sealing in the vicinity of the fracture tip but not near the wellbore, which evidently supports the tip isolation mechanism of the fracture propagation enhancement method.

Chapter 3 Overview of Model Formulation

In this thesis, Abaqus Standard, a commercial software for finite element analysis, is adopted to simulate the processes of lost circulation and WBS. The fully coupled hydraulic fracturing code based on the CZM enables the explicit capture of dynamically induced fracture growth during lost circulation, along with mechanical wellbore behaviors. For the first part of this chapter, we briefly introduce simulation purposes and capabilities of the simulation tool. Then, we present governing equations that couple different physical processes occurring during hydraulic fracturing. Lastly, we discuss mesh generation and validation that ensure simulation accuracy.

3.1 Methodology Description

For this thesis, the computational model of lost circulation generally requires simulation of wellbore excavation and fracture propagation due to fluid pressurization. Furthermore, a time-dependent fluid-solid interaction is essential to model rocks, the porous medium. With these objectives, the selected software offers vigorous coupling of the physical processes during lost circulation, including (1) pore fluid flow within the porous medium, (2) porous medium deformation due to fluid pressurization at the opening surface and poroelastic effect generated by pore fluid flow, (3) fracture fluid flow and seepage loss within the fracture, and (4) irreversible fracture propagation. In this model, 2D plane strain and large fracture height are assumed to minimize the computation while acquiring the most significant physics. We employ pore pressure plane strain elements (CPE4P) to model the rock, pore pressure cohesive elements (COH2D4P) to model fracture initiation and propagation, and fluid pipe elements (FP2D2) to model fluid flow inside the wellbore annulus and to maintain a mass balance among pipe element, fluid seepage at wellbore, and fluid flow into the fracture.

CZM is used to model fracture propagation. The advantage of CZM is considering the fracture process zone ahead of the crack tip to capture nonlinear fracture-mechanics behavior on the basis of energy condition, which implies fracture propagation occurs when the energy release rate reaches a critical value in the process zone. Different from the LEFM characteristics of fracture dimension and loading condition, CZM models the crack tip as a process zone experiencing progressive damage with material softening due to microcracks and pore space, and it estimates distribution and intensity of cohesive stress base on material properties (as shown in Figure 3.1). Thus, CZM is more applicable for modeling quasibrittle material, such as ductile rocks.

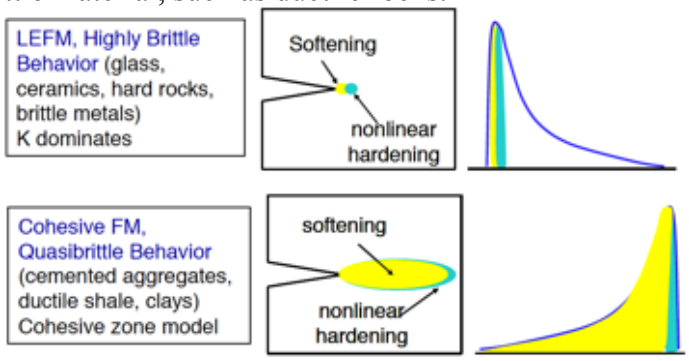

Figure 3.1: Fracture process zone in linear elastic fracture mechanics and cohesive zone model. (Modified from Yao et al. 2010)

The validation of the numerical tool used here with respect to semi-analytical fracture propagation solutions was documented by Zielonka et al. (2014). Fracturing experiments also confirmed the applicability of the numerical approach used here (Ning et al. 2015). Yao et al. (2010) compared cohesive fracture results with a pseudo-three-dimensional (pseudo-3D) model and the Perkins-Kern-Nordgren model, and they showed that CZM can predict hydraulic fracture geometry more accurately. Shin and Sharma (2014), and Haddad and Sepehrnoori (2014) investigated stress interference during multifracture propagation. Kostov et al. (2015) illustrated an automated workflow to

estimate fracture geometry for optimizing wellbore integrity. Wang et al. (2016) investigated plasticity effect during fracture propagation.

3.2 GOVERNING EQUATIONS

The previous section stated the physical processes taking place during lost circulation (or induced fracturing). The governing equations are Darcy's law for pore fluid flow, Biot's theory of poroelasticity for porous medium, Reynold's lubrication theory for fracturing fluid flow, the traction-separation constitutive law for cohesive fracture modeling, and Bernoulli's equation for fluid flow in the pipe (Abaqus 2016).

3.2.1 Fluid Flow in Porous Medium

Pore fluid is assumed to be single-phase and fully saturates the porous medium. Pore fluid flow is modeled by attaching the finite element mesh to the solid phase, such that fluid may flow through this mesh. A continuity equation is therefore required for the fluid, equating the increase rate of fluid volume, V, stored at a point to the rate of volume of fluid flowing across the surface, S, into the point within the time increment. The liquid mass continuity equation is as follows:

$$\frac{d}{dt}\left(\int_V \rho_w \phi dV\right) = -\int_S \rho_w \phi \boldsymbol{n}\boldsymbol{v}_{\boldsymbol{w}} dS$$

where ρ_w is the mass density of pore fluid, ϕ is the porosity of the porous medium, $\boldsymbol{v}_{\boldsymbol{w}}$ is the average velocity of pore fluid relative to the solid phase (the seepage velocity), and n is the outward normal vector to surface S.

Constitutive behavior of pore fluid flow is governed by Darcy's law as follows:

$$\phi \boldsymbol{v}_{\boldsymbol{w}} = -\widehat{K} \cdot \frac{\partial \psi}{\partial X}$$

where $\phi \boldsymbol{v}_{\boldsymbol{w}}$ is the volumetric flow rate of the liquid through surface S, $\widehat{K}$ is the hydraulic conductivity in which $\widehat{K} = \frac{Kg\rho_w}{\mu}$ converts permeability (in Darcy's unit) to hydraulic

conductivity, μ is the fluid viscosity, ψ is the fluid pressure head, and g is gravitational acceleration. Pressure head driven by gravitational effect is ignored in this study.

3.2.2 Porous Medium Deformation

A porous medium is assumed with isotropic, poroelastic material. The theory of poroelasticity, which couples linear elastic rock deformation and pore pressure, is enforced by Abaqus. Effective stress dictates the material behavior. Effective stress, σ'_{ij}, is expressed in terms of total stress as follows:

$$\sigma'_{ij} = \sigma_{ij} + p_p \delta_{ij}$$

Negative stress magnitude represents compressive stress. In this study, Biot's poroelastic constant is assumed to be 1. Stress equilibrium for the solid phase of the material in terms of the principle of virtual work for the volume under consideration in its current configuration at time t is as follows:

$$\int_V \left(\sigma'_{ij} - p_p I\right) : \delta\varepsilon dV = \int_S t \cdot \delta v dS + \int_V f \cdot \delta v dV$$

where $\delta\varepsilon$ is the virtual rate of deformation, I is the unit matrix, t are surface tractions per unit area, and f are body forces (excluding fluid weight) per unit volume.

3.2.3 Fluid Flow in Fracture

Fluid flow continuity within the fracture gap and through the interface is maintained by the cohesive element. The fluid constitutive response is reflected by tangential flow within the gap and normal flow across the gap (as shown in Figure 3.2). The Poiseuille flow equation constitutes the tangential flow. A linear leak-off model is applied for normal flow.

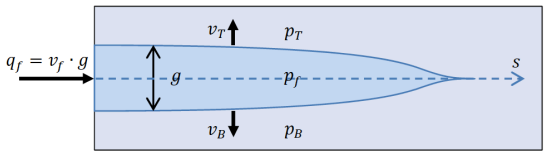

Figure 3.2: Fluid flow within the cohesive element. (Zielonka et al. 2014)

Tangential flow within the fracture is governed by Reynold's lubrication theory, which is defined by the continuity equation as follows:

$$\frac{\partial g}{\partial t} + \frac{\partial q_f}{\partial s} + v_T + v_B = 0$$

where g is the fracture aperture, $q_f = v_f \cdot g$ is the tangential flow rate of fracture fluid across the fracture, and v_T and v_B are the normal flow velocities of fracture fluid leaking through the top and bottom fracture surfaces into the porous medium. Incompressible, Newtonian fluid through narrow parallel plates comprises the momentum equation as follows:

$$q_f = -\frac{g^3}{12\mu_f}\frac{\partial p_f}{\partial s}$$

where μ_f is the fracture fluid viscosity. Normal flow is characterized by a simplified leak-off model as follows:

$$v_T = C_T(p_F - p_T)$$

$$v_B = C_B(p_F - p_B)$$

where p_F, p_T, and p_B are the fracture fluid pressure and pore fluid pressure on the top and bottom surface of the fracture, and C_T and C_B are the leak-off coefficients for each surface. In fact, leak-off coefficients define permeability damage by fracture fluid (i.e., mud cake), and two nodal points define the crossing surface, as shown in Figure 3.3.

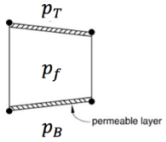

Figure 3.3: Leak-off coefficient interpretation as a permeable layer. (Abaqus 2016)

Thus, a conversion for leak-off coefficients reasonably quantifies the permeability formation damage at the fracture surface as follows:

$$\mathrm{C} = \frac{k_{cake} * A_{fracture\ surface}}{\mu_{pore\ fluid} * g_{initial}}$$

3.2.4 Fracture Initiation and Propagation

Fracture initiation and propagation is modeled based on a cohesive zone method using coupled pressure/deformation cohesive elements. Because cohesive element is predefined, fracture propagates along this guided path. Because material homogeneity and stress field are manually constituted, the concern of fracture turning is evaded.

Cohesive element models the separation of two initially bonded surfaces. Modified CZM with an additional degree of freedom for pore pressure is implemented to simulate material damage resulting from fluid pressurization in the fracture gap where fracture fluid pressure acts as a traction on the fracture surface. Initially, material is modeled with linear elastic behavior, where material stiffness constitutes the deformation. Then, when stress applied on the interface satisfies damage initiation criteria, the cohesive element starts to experience gradual damages as a result of fracture fluid pressure counteracting the in-situ compressive stresses, and a traction-separation constitutive law governs the gradual loss of strength for the cohesive element (SDEG measures the damage in Abaqus, SDEG = 1 when the element is totally damaged). After the element is totally damaged, it becomes an irreversible fractured material with fracture fluid flow and fracture fluid pressure as tractions on the fracture surface. A typical traction-separation constitutive law for a cohesive layer is shown in Figure 3.4.

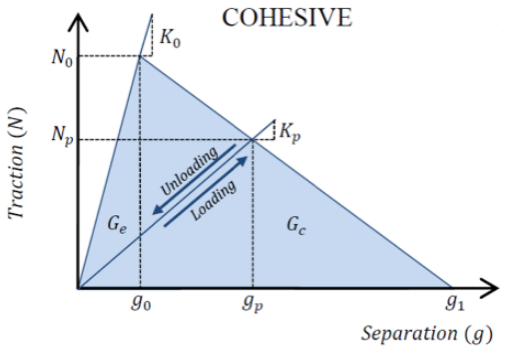

Figure 3.4: A typical traction-separation law. (Zielonka et al. 2014)

In this traction-separation constitutive law, the initial stiffness, K_o, defines the constitutive behavior of linear elastic material prior to damage initiation. Damage initiation is defined by maximum effective tensile strength, N_o, and the quadratic nominal stress criterion as follows:

$$\left\{\frac{N^n}{N_O^n}\right\}^2 + \left\{\frac{N^s}{N_O^s}\right\}^2 + \left\{\frac{N^t}{N_O^t}\right\}^2 = 1$$

where the superscript indicates the direction of nominal stress. After damage is initiated, the cohesive layer evolves from g_0, where maximum tensile strength meets g_1, where the layer is fully damaged and is free to open beyond this separation. If the interface is unloaded prior to complete damage, a linear traction ramp-down is applied with damaged stiffness, K_p. The area under the softening part of the traction-separation curve is the fracture energy, G_c. Conversion of fracture energy from fracture toughness is conducted under Irwin's equation as follows:

$$G_C = \frac{K_{IC}^2(1-v^2)}{E}$$

Linear softening is assumed in our study. Only Mode 1 fracture propagation is considered. When dissipated energy reaches critical fracture energy, the material is fractured.

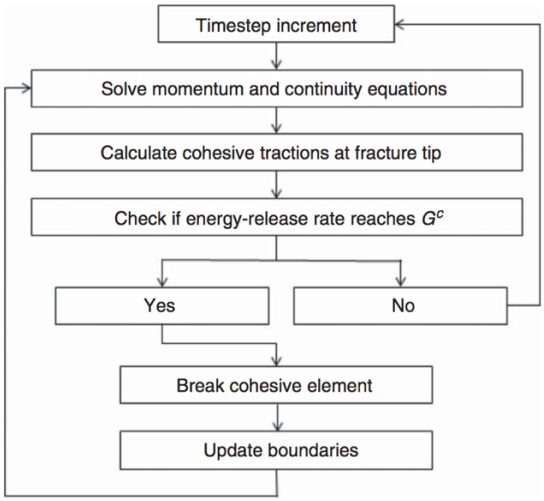

Figure 3.5: Solution flow diagram for fracture propagation procedure (Wang et al. 2016)

3.2.5 Fluid Flow in Pipe

Fluid pipe elements are used to model fluid flow at the wellbore annulus. By adopting a "tie" constraint between pipe element and wellbore nodes, this element automatically maintains fluid conservation and equilibrium among pipe element, fluid seepage at the wellbore, and fluid flow into the fracture. A pipe element defined by two nodes assumes steady-state flow and incompressible single-phase fluid and is filled with fluid at all times. Providentially, pressure boundary condition is able to be specified for this element and offers better understanding of lost circulation with respect to ECD.

Pressure loss of pipe flow is governed by Bernoulli's equation as follows:

$$\Delta \mathrm{P} = (C_L + K_i)\frac{\rho v^2}{2}$$

$$C_L = \frac{fL}{D_h}$$

where $\Delta \mathrm{P}$ is the pressure loss between two nodes, ρ is the fluid density, C_L is the loss coefficient, K_i is the directional loss term, f is the frictional factor of pipe, L is the pipe length, and D_h is the diameter of the pipe. Gravitational term is disregarded in the above equation.

3.3 Mesh Generation and Validation

A convergence study is performed to guide simulation model discretization. This particular work is highly necessary to ensure simulation accuracy. To model lost circulation, excessive loading is applied at the wellbore, and mesh dependency of cohesive fracture propagation is simulated. Hence, mesh refinement is conducted in the vicinity of the wellbore experiencing the most deformation and the cohesive element. Model geometry (as shown in Figure 3.6) in this convergence study is consistent with all other models in this thesis. Boundary conditions and loads applied in this convergence study replicate the bottomhole condition and are consistent with all others as well.

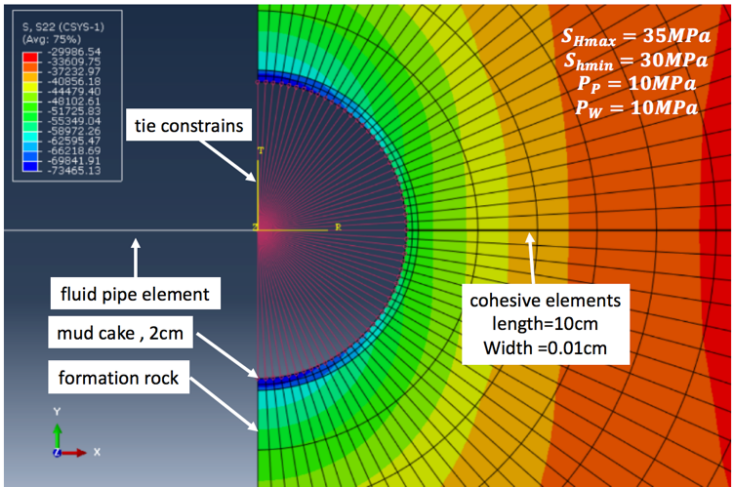

Figure 3.6: Final mesh refinement for elements at the wellbore wall and cohesive elements. Figure is showing the hoop stress after wellbore excavation.

Kirsch's solution with positive compressive stress is used to validate the hoop stress obtained from the numerical solution with negative compressive stress. By refining nodes along the wellbore surface, numerical results are plotted with the analysis solution, as shown in Figure 3.7. Because a thin layer of mud cake is defined near the wellbore wall, an aspect ratio of elements along the wellbore wall is optimum for finite element analysis, as long as the node point is refined properly.

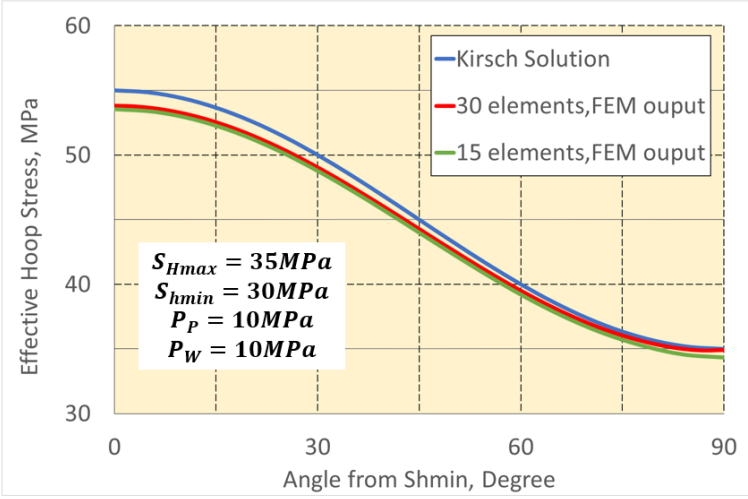

Figure 3.7: Comparison of hoop stresses from numerical results to Kirsch's solution.

As a converged solution is obtained, 30 elements are meshed along one-quarter of the wellbore wall. Under this mesh, error differences with respect to the analytical solution, which is independent of deformation, is less than 2.5%.

The nodal setup of the cohesive element is shown in Figure 3.8. The width of cohesive element H is set as 0.0001 m or 100 micrometers.

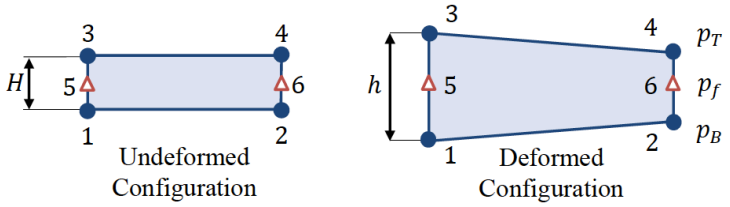

Figure 3.8: Coupled pressure/deformation cohesive element. (Zielonka et al. 2014)

Because fractures propagate in the longitudinal direction (i.e., middle nodes) of cohesive element, refinement is conducted on the length. By simulating constant flow rate injections with different element sizes, a smooth and converged FPP is obtained (as shown in Figure 3.9). Therefore, 10 cm is used for the cohesive element length.

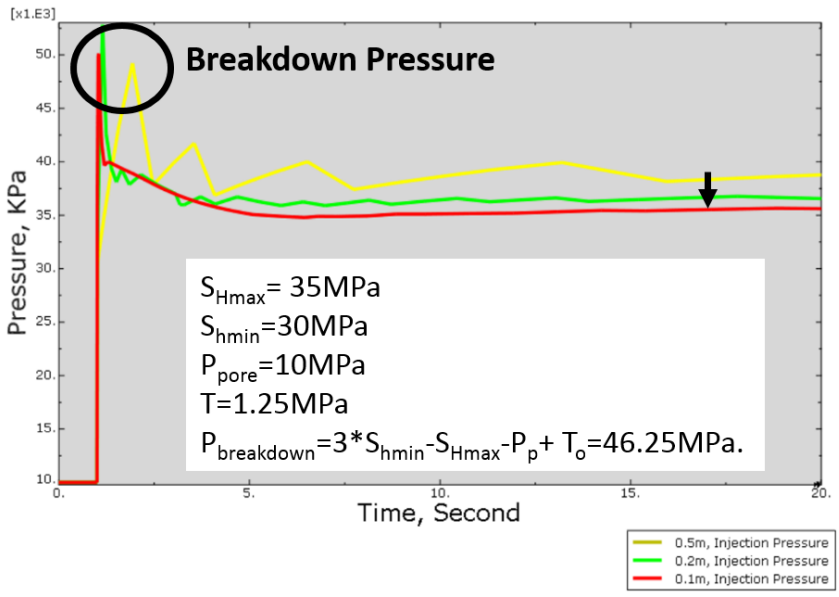

Figure 3.9: Convergence study on cohesive element.

3.4 HIGHLIGHTS OF THE CHAPTER

- Abaqus Standard is utilized to simulate the processes of lost circulation and WBS. The basic features and governing equations of Abaqus are introduced in this chapter as a background for the simulation steps in the following chapter.
- The flexibility of this fully coupled hydraulic fracturing simulator assists in effectively modeling nonlinear correlations among various geological conditions and bottomhole conditions.
- The simplicity of the governing equation effectively reduces computational efforts and accurately replicates the multiphysics process of induced fracturing.
- A convergence study is performed to validate the discretization approach involved in the finite element analysis. The converged results prove an acceptable simulation accuracy for the meshing method used.

Chapter 4: Parametric Study of Lost Circulation

In this chapter, results of a parametric study on lost circulation are presented. The purpose of this analysis is to investigate lost circulation patterns under various material properties and downhole conditions. The focused subjects are hoop stress in the vicinity of wellbore, fracture geometry, and rate of lost circulation. This chapter first introduces the simulation setup and validations. Then, a base case is generated as a benchmark for the parametric study, and each parametric influence is separately discussed. Finally, obtained insights are summarized.

4.1 Model Description

The model geometry comprises a 2D semicircular plate and a fluid pipe (as shown in Figure 4.1). The semicircular plate is simplified from a complete wellbore because boundary conditions assigned to the symmetry surface replicate the existence of the other half of the wellbore. Plain strain thickness is 1 m, the external boundary is 15 m away from the wellbore center, the wellbore radius is 0.25 m, and the fluid pipe is 1m long.

A tie constraint (as shown in Figure 4.3) is applied to the last node of the fluid pipe element and all nodes along the wellbore surface so that these nodes share the same pore pressure degree of freedom. Mud column gravitational effect is ignored in this study. Boundary conditions assigned at the fluid pipe represent downhole fluid conditions (i.e., ECD, flow rate). Pressure loss across the fluid pipe is negligible, and a layer of mud cake with low permeability is beside the wellbore surface (as shown in Figure 4.2). Furthermore, with a predefined stress field, fractures propagate along the layer of cohesive elements placed along the azimuth of S_{Hmax}. All materials are assumed homogenous and isotropic.

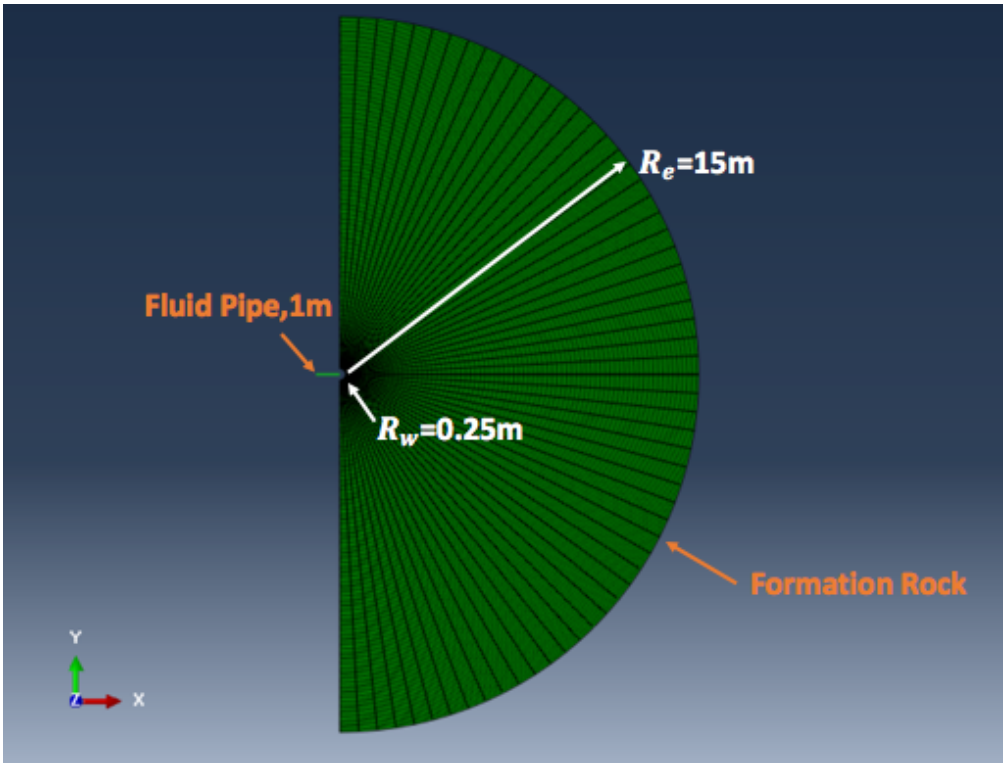

Figure 4.1: Model geometry with mesh.

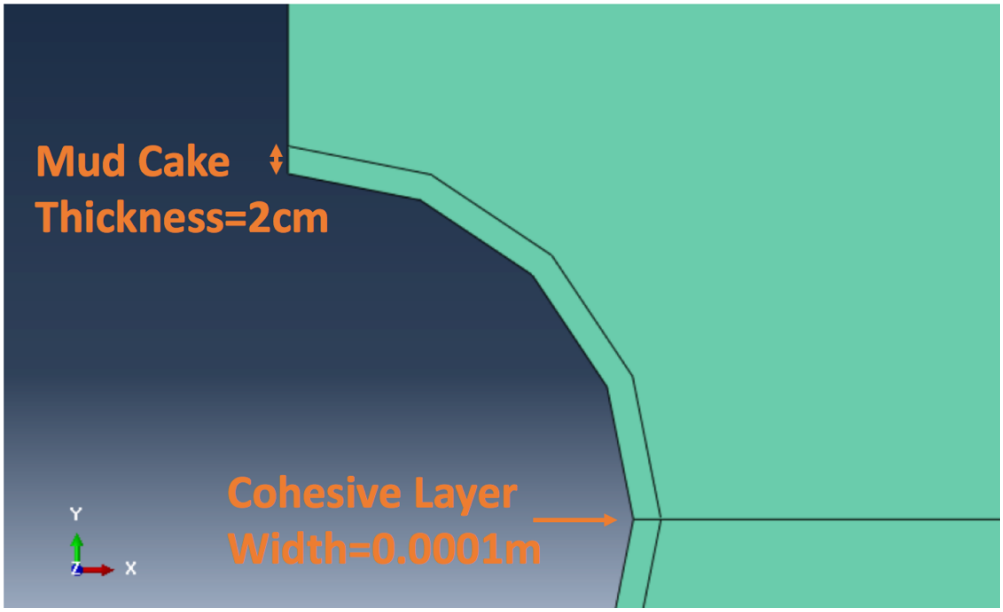

Figure 4.2: Model partition in the near-wellbore region. Cohesive elements are inserted in the middle of the semicircular plate along the azimuth of S_{Hmax}.

Nodal distance is uniform in both radial and tangential directions of the wellbore (as shown in Figure 4.3). Overall, 9091 linear elements are executed in the simulation model, which consists of two fluid pipe elements (FP2D2), 149 cohesive elements (COH2D4P), and 8940 pore fluid/stress elements (CPE4P).

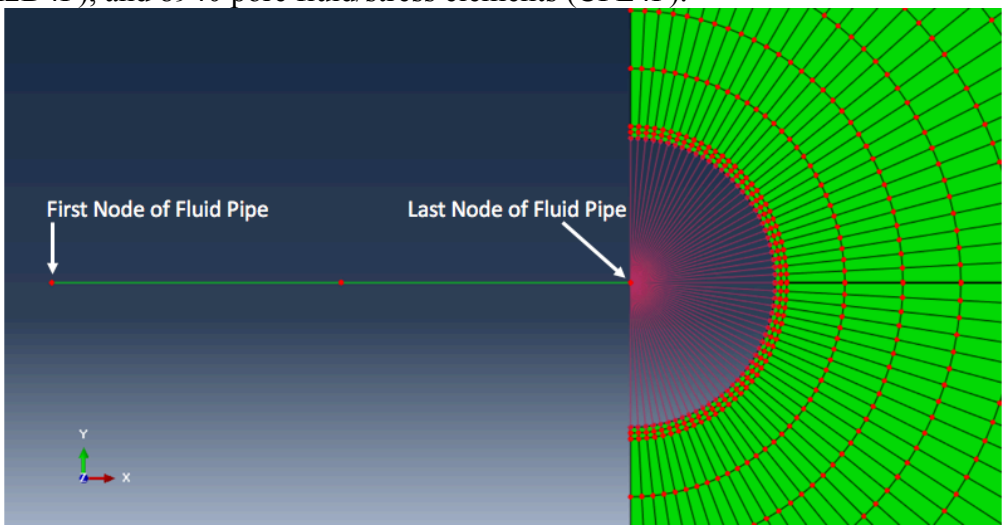

Figure 4.3: Seeded nodes in the near-wellbore region. Pink lines represent tie constraint.

Even though the numerical results might not exactly align with the analytical solution or precisely reproduce lost circulation events in the field, a consistent simulation approach, employed to all cases in this parametric study, rigorously guarantees the logic of observations presented in the rest of the thesis. A quote from George Box is applicable on this point: “All models are wrong, but some are useful” (Box and Draper 1987).

4.2 Boundary Conditions and Loads

The simulation model in this parametric study follows three steps: initialization, wellbore excavation, and lost circulation. These steps replicate a complete process of mud loss, following a sequence of initializing subsurface conditions, removing rock material by drilling, and pressurizing mud to induce fracture growth.

The first step initializes subsurface conditions for formation rock, including porosity, pore pressure, and effective in-situ stresses. Boundary conditions are listed as follows:

- Zero radial displacement is assigned at the outer surface and wellbore surface.
- Zero normal displacement is assigned at the symmetric surface.

Initial conditions are characterized by predefined fields, which are listed as follows:

- Rock porosity is assigned to all continuum elements.
- Pore pressure is assigned to all elements.
- Effective stress tensor is assigned to all continuum elements.
- Initial gap is specified for a cohesive element located at the wellbore wall.

Initial gap is required by Abaqus to initialize fracture propagation. After fluid leaves the pipe element, some of the fluid flows into the predamaged element to initiate fracture growth, while the other part diffuses at the wellbore surface and flows into the formation.

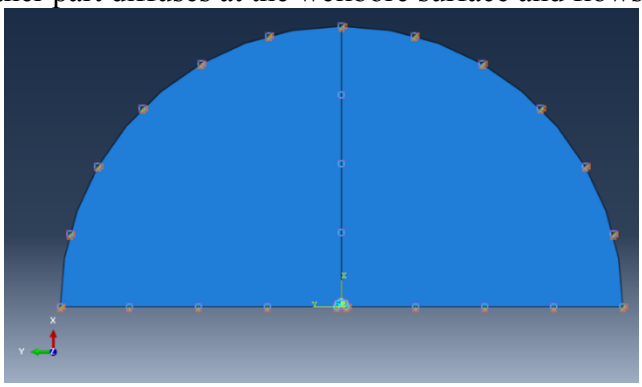

Figure 4.4: Boundary conditions and predefined fields in the initialization step.

The second step simulates the drilling process, where a certain volume of material is removed and mud pressure acts as a traction applied at the wellbore surface. In this step, the wellbore surface experiences deformation, as well as stress concentration in the

tangential direction. A "Geostatic" procedure is conducted in Abaqus. Boundary conditions are listed as follows:

- Zero radial displacement at the wellbore surface is deactivated.
- All other surface-displacement constraints are kept for this step and the next steps.

A pore pressure mechanical load (i.e., PORMECH, as shown in Figure 4.5) is applied at the wellbore surface, where surface traction equals the pore pressure of the nodes at the wellbore surface. This loading condition implies a pressure balance between drilling fluid and formation fluid.

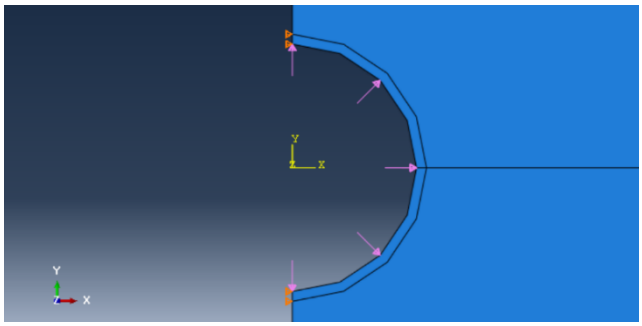

Figure 4.5: Boundary conditions and loads in the wellbore excavation step.

In the third step, previous boundary conditions and loads are kept. A new pressure boundary condition is created at the external boundary with a value of initial pore pressure; this condition is for fluid transient flow within the rock. A constant pressure boundary condition is applied at the first node of the fluid pipe element (as shown in Figure 4.3) to model wellbore pressure (i.e., ECD). With two pressure boundary conditions defined, fracture propagation is computed under the procedure "Soils, Consolidation," which is a transient coupled pore pressure/effective stress analysis. By utilizing a "tie" constraint and "PORMECH" simultaneously, wellbore surface traction is always equal to fluid pressure at the fracture mouth. The simulation time is set at 5 seconds for this parametric study, but it terminates when the CZM process zone reaches to the fixed external boundary.

4.3 BASE CASE

The base case (and all other cases) simulates lost circulation occurring in a vertical wellbore with a 3000-m TVD. Estimations of effective in-situ stresses and pore pressure are listed in Table 4.1. Rock properties used in the base case are similar to Berea Sandstone material properties (as listed in Table 4.2, Morita et al. 1990).

TVD	3000	m			
Overburden Gradient	23	MPa/km	Pore Pressure Gradient	9.8	MPa/km
S_v	69	MPa	Pore Pressure	**29.4**	MPa
K_ratio (S_v/S_hmin)	0.79		Effective Stresses		
K_ratio (S_v/S_Hmax)	0.82		S'_v	**39.60**	MPa
S_hmin	54.51	MPa	S'_hmin	**25.11**	MPa
S_Hmax	56.58	MPa	S'_Hmax	**27.18**	MPa

Table 4.1: Subsurface stress estimation for base case.

Cohesive Elements			Formation Rock		
Tensile Strength	1250	KPa	Young's Modulus, E	1E+07	KPa
Fracture Energy	0.1	KPa*m	Poisson's ratio, v	0.2	
Fracture Toughness	1.03	MPa*sqrt(m)	Biot Coefficient	1	
Fracture Fluid	20	cp	Permeability	100	mD
Leak-off Coefficient	1E-07	m/s	Pore Fluid Specific Gravity	9.8	KPa/m
			Pore Fluid Viscosity	1	cp

Table 4.2: Material parameters for base case.

Static mud cake experiments conducted in Wider Windows revealed an initial cake permeability of 0.01 mD and a permeability range of 0.0005 to 0.001 mD after a few minutes of pressure holding (Jaffal 2016). Therefore, 0.0005 mD was selected as the mud cake permeability for the base case so that fluid is much easier placed in the fracture rather than being diffused at the wellbore surface. Due to complex pressure loading and filtrate leaking conditions, the physical model describing mud cake formation at the fracture surfure still remains a challenge for the industry. In addition, considering the narrow fracture opening and rapid propagation of drilling-induced fracture, cake development in the early propagation process should be limited. Therefore, in this lost circulation model, which simulates fracture propagtion for 5 seconds, 0.1 mD is used as the damaged

permeability (i.e., leak-off coefficient) at the fracture surface. This study ignores the mechanical interference of mud cake (cake shares the same mechanical properties with rock) and only considers the permeability damage caused by particle plugging at the opening surface.

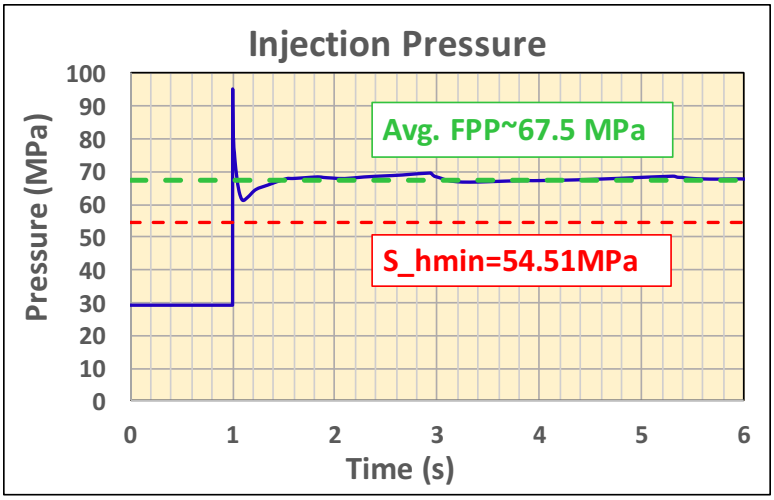

Figure 4.6: Injection pressure of Case 2. Fluid is injected at 0.01 m^3/s for 5 seconds.

With the same material properties of the base case, an injection case is additionally performed to estimate FPP (as shown in Figure 4.6). The third simulation step is modified with a constant flow rate load (i.e., CFLOW) at the first node of the fluid pipe element. FPP, which is the injection pressure recorded at the pipe inlet, is above minimum horizontal stress in this injection case. Breakdown pressure is higher than analytical breakdown pressure, which is 78.8 MPa using Equation 2.1, and is not comparable with the analytical one due to different fracturing mechanisms. For the base case, a value of 78 MPa was selected as wellbore pressure, which is higher than the injection case FPP but lower than the analytical breakdown pressure.

Comparing the simulation results between the base case and injection case, with a defined wellbore pressure, the final fracture geometry is significantly larger than that of

the constant flow rate (as shown in Figure 4.7). Even though wellbore pressure in the base case is about 15% higher than the injection case FPP, the total volume of fluid entering the fluid pipe (i.e., the total mud loss volume) is tripled (as shown in Figure 4.8). Fracture length of the base case is about 11 m after wellbore pressure is held for 5 seconds. Since frictional pressure loss at the fracture surface is negligible, fracture fluid pressure is almost the same as wellbore pressure. Assuming an infinite source of drilling fluid, as fracture fluids leak-off and new fracture volume generates, a constant wellbore pressure defined as the boundary condition continuously drives fluid flow into the fracture in order to maintain fracture fluid pressure close to wellbore pressure. Consequently, fluctuating fluid flow rates are induced, and a greater total fluid volume entering the fracture is generated. Therefore, for the same period of time, fracture growth due to excessive ECD (i.e., lost circulation) is more significant than the one from the injection test (i.e., LOT).

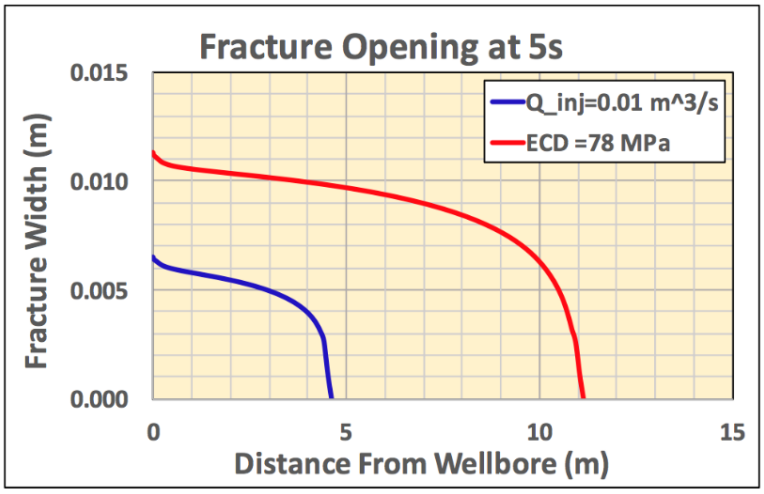

Figure 4.7: Comparison of final fracture geometry between base case and injection case.

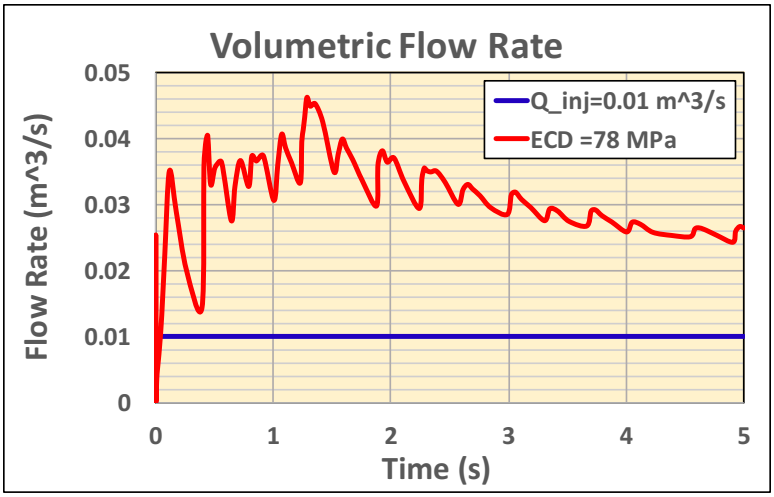

Figure 4.8: Comparison of volumetric flow rate between base case and injection case.

The fracture mouth opening is plotted in Figure 4.9. Because the width of the fracture mouth continuously grows from 1 to 2 seconds, the effective hoop stresses along the wellbore wall at those moments is extracted, as shown in Figure 4.10.

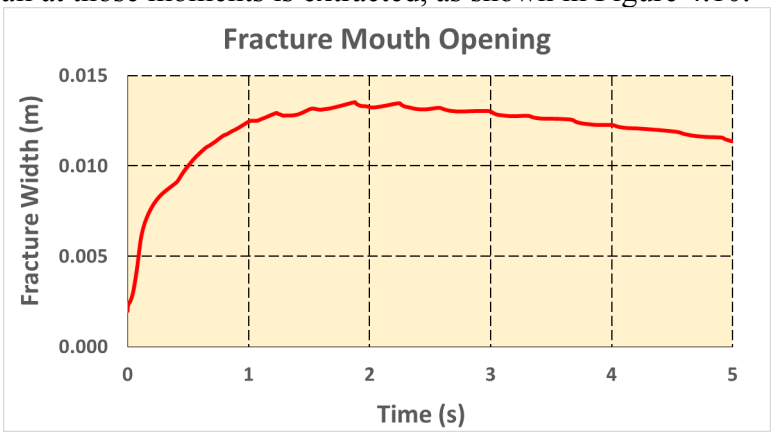

Figure 4.9: Fracture mouth widths of base case.

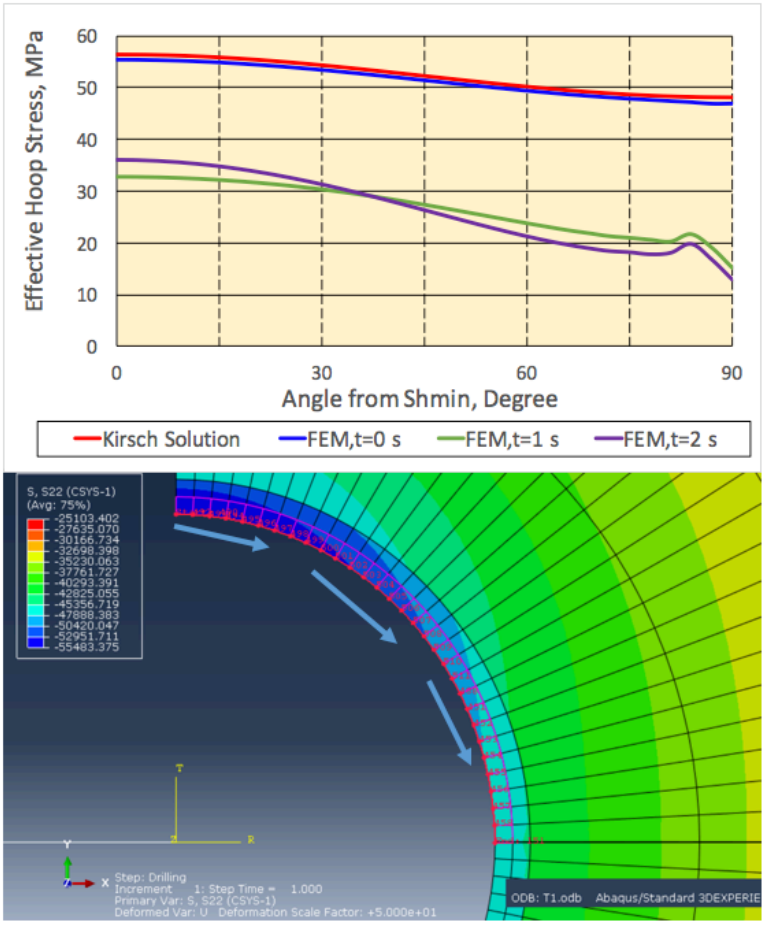

Figure 4.10: Effective hoop stress around the wellbore. Data are obtained from red dotted nodes in the lower picture.

As fracture width increases about 0.001 m from 1 to 2 seconds, an effective hoop stress increase is observed of approximately 3 MPa, meaning the rock becomes more compressive at an azimuth of S_{hmin} (i.e., 0˚ in Figure 4.10). However, effective hoop stress decreases by approximately 2 MPa at an azimuth of S_{Hmax} (i.e., 90˚ in Figure 4.10).

To avoid possible element overdistortion due to boundary conditions, hoop stress around the inner surface of the rock material is also obtained (as shown in Figure 4.11). Similar to the stress variation around the wellbore surface from 1 to 2 seconds, hoop stresses increase between 0 and 24° and decrease otherwise.

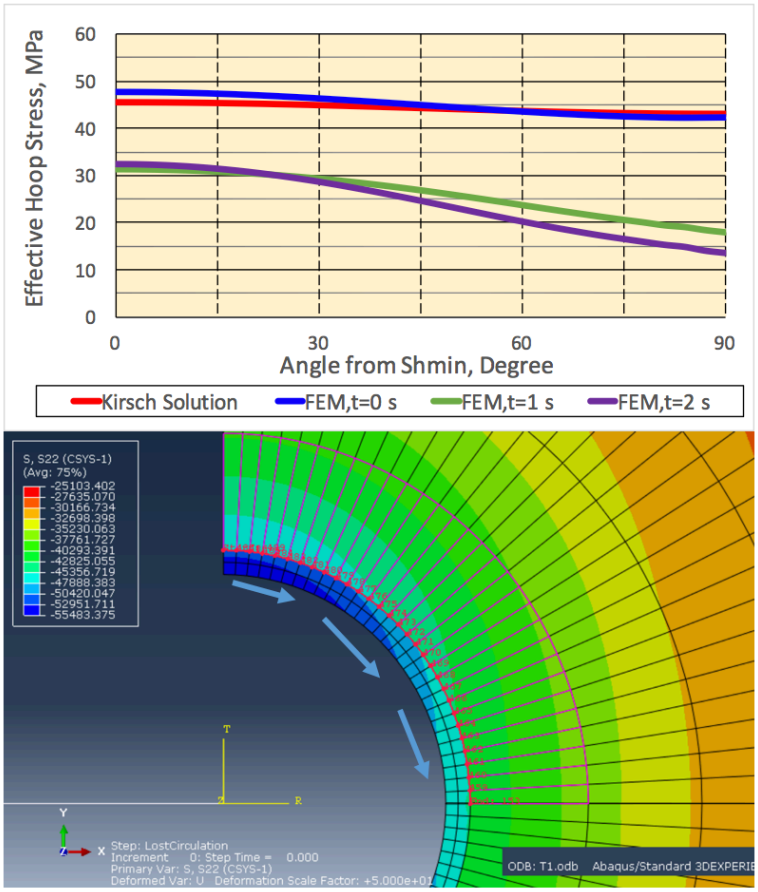

Figure 4.11: Effective hoop stress along a path in the vicinity of wellbore. Data are obtained from red dotted nodes in the lower picture.

The reduction in hoop stress is due to the elevation of pore pressure as fluid invades rock through both the fracture surface and the wellbore. Assuming Biot's coefficient of 1, the total hoop stresses along this path (as shown in Figure 4.13) are calculated by adding pore pressures (as shown in Figure 4.12) to effective stresses (as shown in Figure 4.11). From 1 to 2 seconds, a slight increase in total hoop stress occurs between 0 and 60°; total stresses at the few nodes in the vicinity of 90° still decrease from 1 to 2 seconds. However, total hoop stresses are elevated about 10 MPa from the initial intact condition to the fractured condition at 1 second. Therefore, fracture width growth leads to hoop stress enhancement,

but the counterproductive effect from pore pressure is also substantial in reducing effective hoop stress.

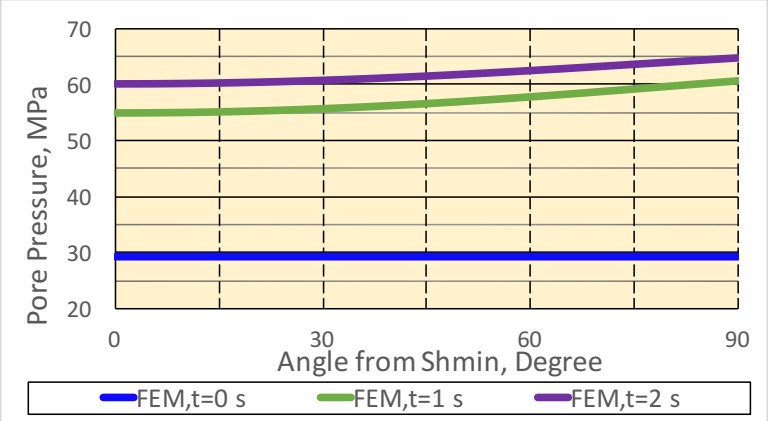

Figure 4.12: Pore pressure along the path from base case.

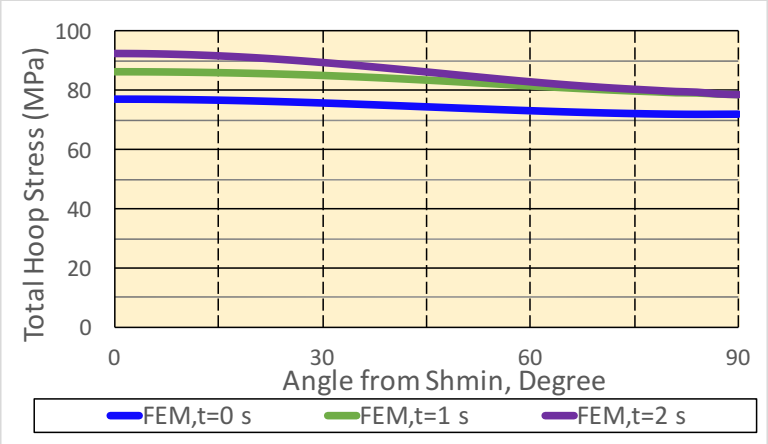

Figure 4.13: Calculated total hoop stresses along the path from base case.

The pattern of fluid invasion during lost circulation is shown in Figure 4.14 and Figure 4.15. Several pressure fronts appear and propagate along the wellbore tangential direction in the near-wellbore region. Even though mud cake acts as a good fluid barrier, leak-off fluid at the fracture surface penetrates rock and raises pore pressure. Thus, rock near the fracture surface experiences intense pore pressure buildup and possibly becomes tensile-stressed, even though fracture width is growing. This poroelastic effect is similar

and consistent with previous double porosity wellbore stability analysis (Zhang and Roegiers 2005). Despite simulating lost circulation in a 100-mD rock, considering poroelasticity with Biot's coefficient of 1 and ignoring capillary pressure or further fluid flow complexity, fluid seepage significantly deteriorates hoop stress enhancement during initial lost circulation. However, if elevated pore pressure is later mitigated as pore fluid dissipates to the far field, hoop stress enhancement is still achievable.

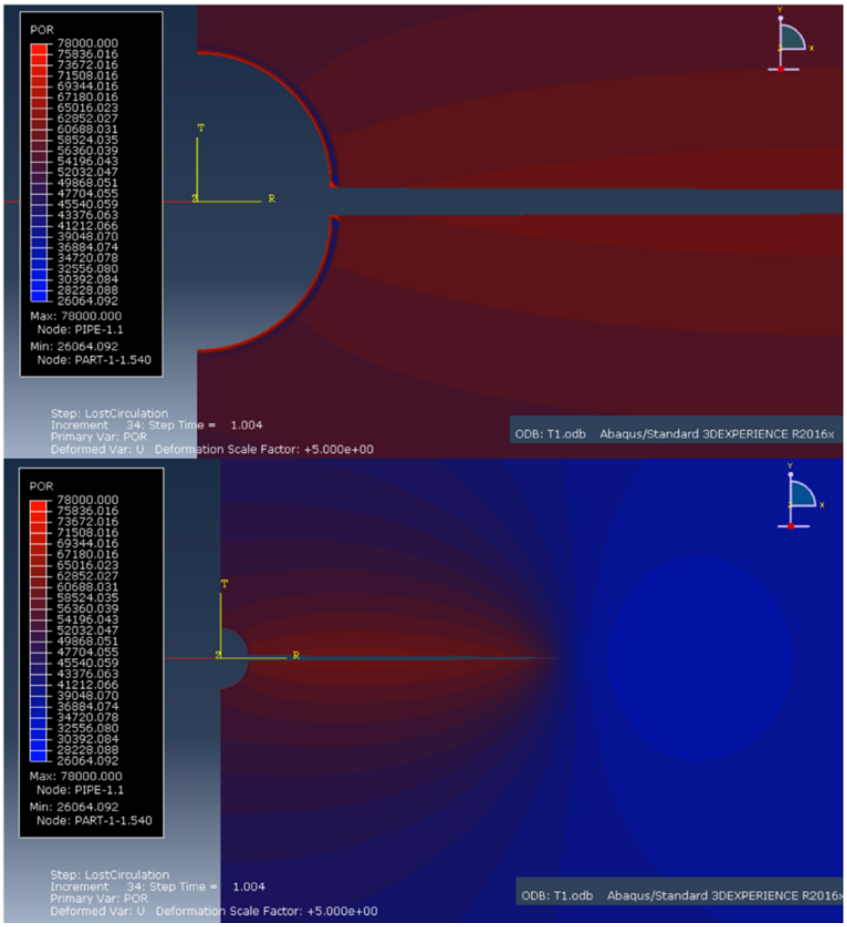

Figure 4.14: Pore pressure at 1 second from the base case. Deformation is magnified five times.

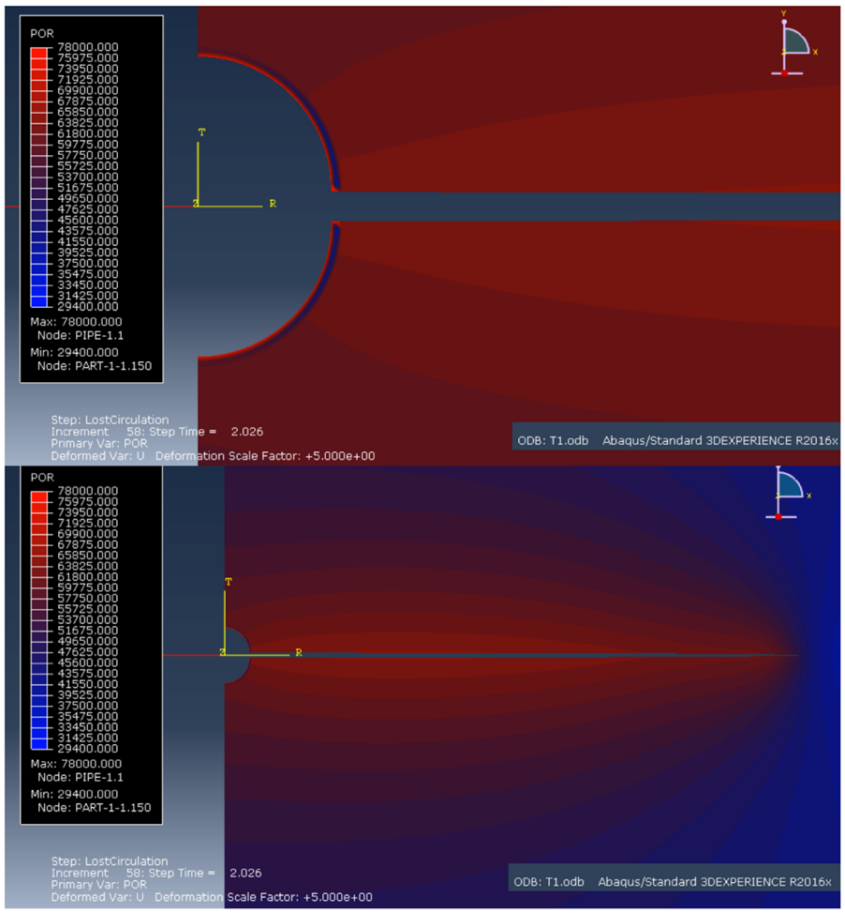

Figure 4.15: Pore pressure at 2 seconds from the base case. Deformation is magnified five times.

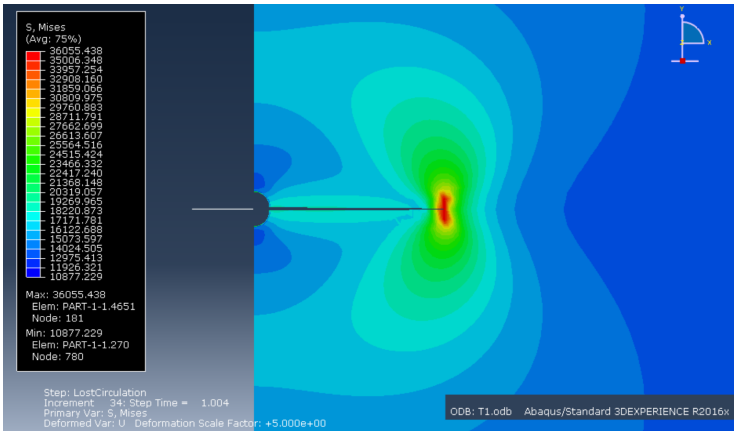

Figure 4.16: Von Mises stress at 1 second from the base case. Deformation is magnified five times.

4.4 Study on Rock Properties

The strategy of this parametric study is to investigate influences on fracture geometry. Volumetric flow at the first node of the fluid pipe element, which is equivalent to mud loss rate (or loss rate), is plotted as well. Each study only modifies one parameter. For consistency, red text represents results from the base case. A summary of parametric input is listed in Table 4.3. Average computational time among these cases is about 4 minutes.

		Effective In-situ Stress Field				Rock						Mud Cake		Cohesive Elements						Notes
Purpose	Case #	S'_Hmax (KPa)	S'_hmin (KPa)	S'_v (KPa)	P_pore (KPa)	E (KPa)	v	k (mD)	K (m/s)	ϕ	μ_pore (cp)	k (mD)	K (m/s)	C_leak-off (m/(KPa*s))	G_c (KPa*m)	K_Ic (MPa*sqrt(m))	Tensile Strength (KPa)	μ_fracture (KN*S*M^-2)	ECD (KPa)	Time=5s
Base Model	1	27,140	25,110	39,600	29,400	1.00E+07	0.2	100	9.80E-07	0.25	1	0.0005	4.90E-12	1.00E-07	0.1	1.02	1250	2.00E-05	78,000	μ_fracture= 20 cp
	2	27,140	25,110	39,600	29,400	1.00E+07	0.2	100	9.80E-07	0.25	1	0.0005	4.90E-12	1.00E-07	0.1	1.02	1250	2.00E-05		Q_injection=0.01m^3/s
Young's Modulus	3	27,140	25,110	39,600	29,400	1.50E+07	0.2	100	9.80E-07	0.25	1	0.0005	4.90E-12	1.00E-07	0.1	1.25	1250	2.00E-05	78,000	
	4	27,140	25,110	39,600	29,400	2.00E+07	0.2	100	9.80E-07	0.25	1	0.0005	4.90E-12	1.00E-07	0.1	1.44	1250	2.00E-05	78,000	
Fracture Toughness	5	27,140	25,110	39,600	29,400	1.00E+07	0.2	100	9.80E-07	0.25	1	0.0005	4.90E-12	1.00E-07	0.4	2.04	1250	2.00E-05	78,000	
	6	27,140	25,110	39,600	29,400	1.00E+07	0.2	100	9.80E-07	0.25	1	0.0005	4.90E-12	1.00E-07	0.8	2.89	1250	2.00E-05	78,000	
Tensile Strength	7	27,140	25,110	39,600	29,400	1.00E+07	0.2	100	9.80E-07	0.25	1	0.0005	4.90E-12	1.00E-07	0.1	1.02	1000	2.00E-05	78,000	
	8	27,140	25,110	39,600	29,400	1.00E+07	0.2	100	9.80E-07	0.25	1	0.0005	4.90E-12	1.00E-07	0.1	1.02	800	2.00E-05	78,000	
Rock Permeability	9	27,140	25,110	39,600	29,400	1.00E+07	0.2	5	4.90E-08	0.25	1	0.0005	4.90E-12	1.00E-07	0.1	1.02	1250	2.00E-05	78,000	
	10	27,140	25,110	39,600	29,400	1.00E+07	0.2	150	1.47E-06	0.25	1	0.0005	4.90E-12	1.00E-07	0.1	1.02	1250	2.00E-05	78,000	
Stress Anisotropy	11	35,000	25,110	39,600	29,400	1.00E+07	0.2	100	9.80E-07	0.25	1	0.0005	4.90E-12	1.00E-07	0.1	1.02	1250	2.00E-05	78,000	
	12	40,000	25,110	39,600	29,400	1.00E+07	0.2	100	9.80E-07	0.25	1	0.0005	4.90E-12	1.00E-07	0.1	1.02	1250	2.00E-05	78,000	
Pore Pressure	13	27,540	25,510	40,000	29,000	1.00E+07	0.2	100	9.80E-07	0.25	1	0.0005	4.90E-12	1.00E-07	0.1	1.02	1250	2.00E-05	78,000	
	14	28,540	26,510	41,000	28,000	1.00E+07	0.2	100	9.80E-07	0.25	1	0.0005	4.90E-12	1.00E-07	0.1	1.02	1250	2.00E-05	78,000	
ECD	15	27,140	25,110	39,600	29,400	1.00E+07	0.2	100	9.80E-07	0.25	1	0.0005	4.90E-12	1.00E-07	0.1	1.02	1250	2.00E-05	67,500	Avg.FPP in #2
	16	27,140	25,110	39,600	29,400	1.00E+07	0.2	100	9.80E-07	0.25	1	0.0005	4.90E-12	1.00E-07	0.1	1.02	1250	2.00E-05	80,000	
Mud Cake	17	27,140	25,110	39,600	29,400	1.00E+07	0.2	100	9.80E-07	0.25	1	0.0040	3.92E-11	1.00E-07	0.1	1.02	1250	2.00E-05	105,000	
	17	27,140	25,110	39,600	29,400	1.00E+07	0.2	100	9.80E-07	0.25	1	0.0100	9.80E-11	1.00E-07	0.1	1.02	1250	2.00E-05	105,000	
Leak-off Coefficient	17	27,141	25,111	39,601	29,399	1.00E+07	0.2	100	9.80E-07	0.25	1	0.0005	4.90E-12	1.00E-06	0.1	1.02	1250	2.00E-05	104,999	~1mD leak-off
	18	27,140	25,110	39,600	29,400	1.00E+07	0.2	100	9.80E-07	0.25	1	0.0005	4.90E-12	1.00E-05	0.1	1.02	1250	2.00E-05	105,000	~10mD leak-off
Mud Viscosity	19	27,140	25,110	39,600	29,400	1.00E+07	0.2	100	9.80E-07	0.25	1	0.0005	4.90E-12	1.00E-07	0.1	1.02	1250	4.00E-05	105,000	μ_fracture= 40cp
	20	27,140	25,110	39,600	29,400	1.00E+07	0.2	100	9.80E-07	0.25	1	0.0005	4.90E-12	1.00E-07	0.1	1.02	1250	1.50E-04	105,000	μ_fracture=150cp
	21	27,140	25,110	39,600	29,400	1.00E+07	0.2	100	9.80E-07	0.25	1	0.0005	4.90E-12	1.00E-07	0.1	1.02	1250	3.00E-04	105,000	μ_fracture=300cp

Table 4.3: List of case input for parametric study.

4.4.1 Effect of Young's Modulus

Final fracture geometries with different Young's moduli (i.e., stiffness) are shown in Figure 4.17. Increasing Young's modulus results in a narrower and longer fracture. When stiffness is low, rock behaves in a more ductile manner and tends to deform so that the fracture width is wider. On the other hand, when stiffness is high, stress concentration at the fracture tip becomes more intense and strain energy buildup at the fracture tip tends to be fostered. As a result, fractures propagate faster. Overall, the influence of rock stiffness is much greater on width than on length.

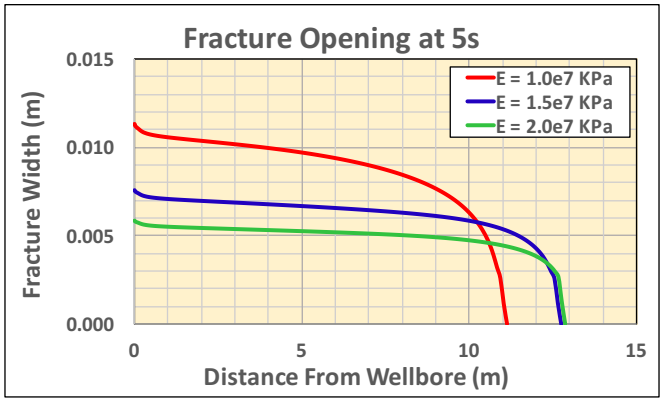

Figure 4.17: Effect of Young's modulus on final fracture geometry.

Figure 4.18 shows volumetric flows over 5 seconds. Because stiffer rock tends to have a smaller fracture mouth opening, a higher pressure is required to force the fluid flow into the fracture. Therefore, with a constant pressure held at the wellbore, fluid flow tends to be less in a stiffer rock with a smaller fracture mouth opening.

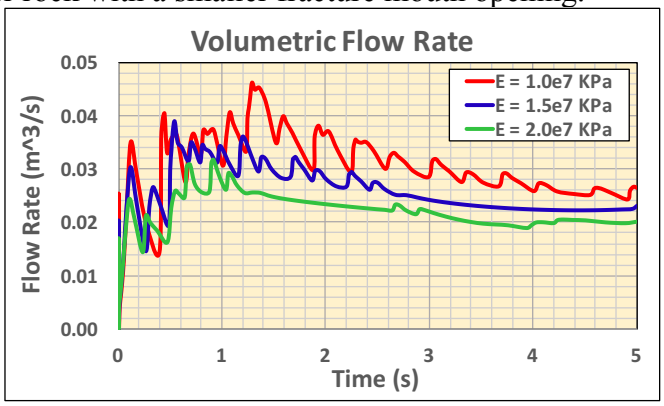

Figure 4.18: Effect of Young's modulus on volumetric flow rate.

Because Young's modulus was mentioned to be critical in previous WBS studies, the same base-case hoop stress plots were prepared for Case 4, which has the highest Young's modulus among all the cases.

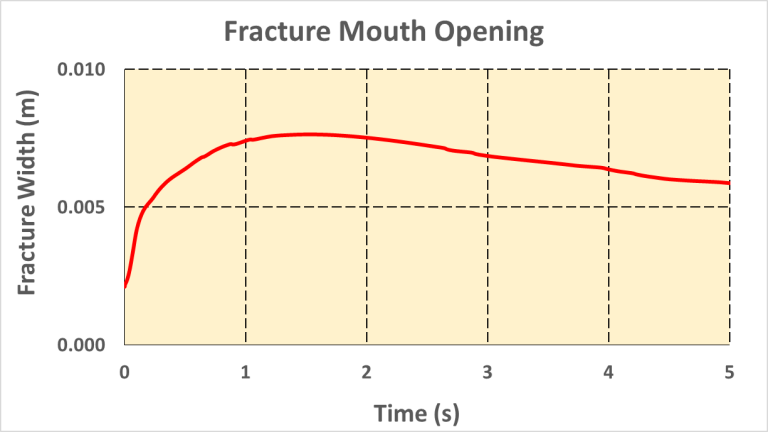

Figure 4.19: Fracture mouth widths of Case 4.

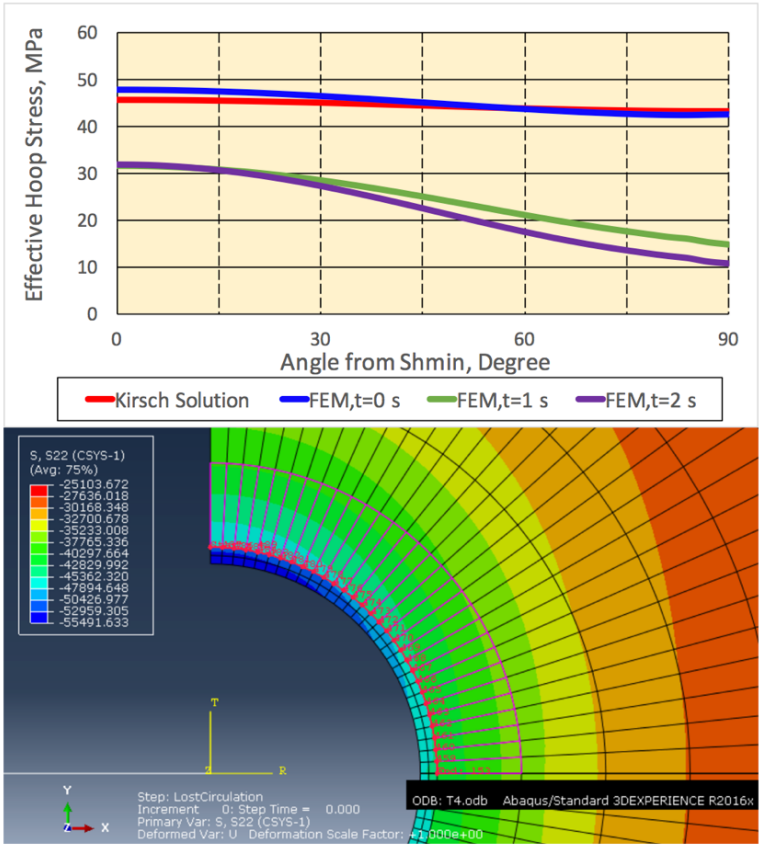

Figure 4.20: Effective hoop stress along a path in the vicinity of the wellbore from Case 4. Data are obtained from red dotted nodes in the lower picture.

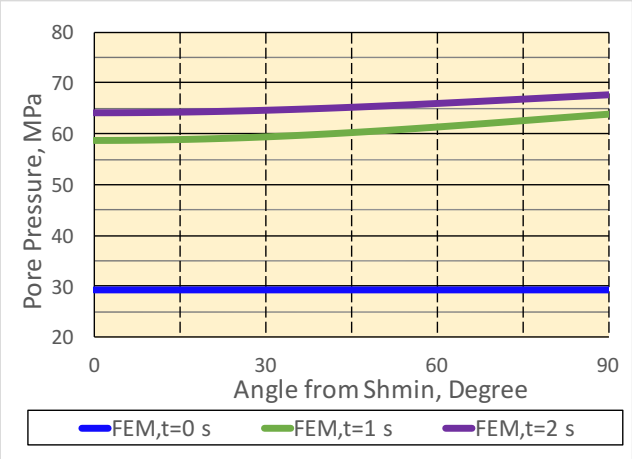

Figure 4.21: Pore pressure along the path from Case 4.

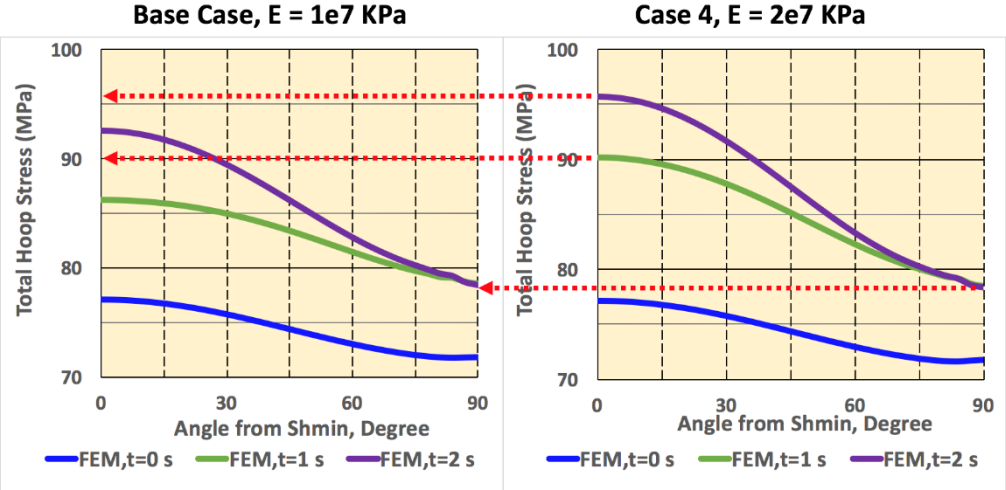

Figure 4.22: Comparison of calculated total hoop stresses along the path from the base case and Case 4.

Hoop stress behavior follows a trend identical to the base case (as shown in Figure 4.22). In the case of a higher Young's modulus, total hoop stress at the azimuth of S_{hmin}, the location least influenced by pore pressure perturbation (i.e., 0° in Figure 4.22), increases about 13.03 MPa from 0 to 1 seconds, while the base case increases 9.12 MPa at the same node. The initial hoop stress and the surface traction are the same for both models, the fracture mouth openings from the base case and Case 4 are the same at 1 second, and

the pore pressure at 0° in Case 4 is about 3.86 MPa higher than the base case at 1 second. Therefore, Young's modulus stimulates the effect of hoop stress enhancement, but it is a minor factor when pore pressure is largely perturbed.

4.4.2 Effect of Fracture Energy

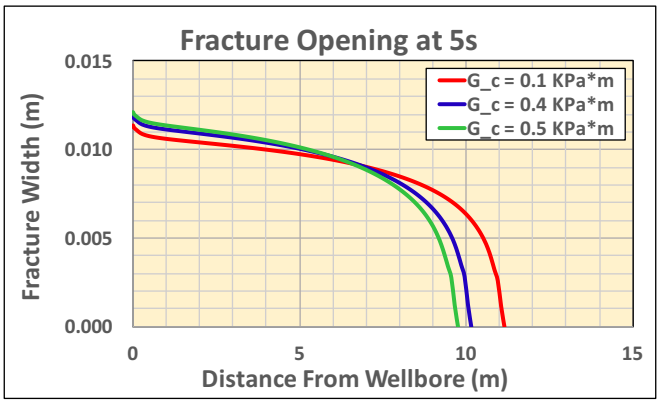

Figure 4.23: Effect of fracture energy on final fracture geometry.

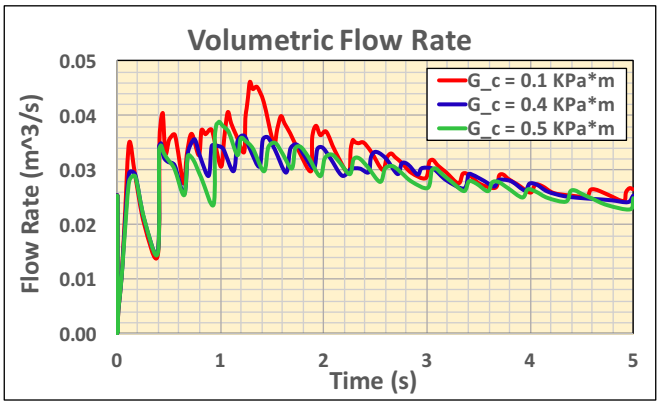

Figure 4.24: Effect of fracture energy on volumetric flow rate.

Fracture energy (i.e., strain energy release rate) mostly impacts fracture length. A higher fracture energy requires more accumulation of strain energy in the process zone ahead of the tip (which is the failure mechanism of CZM). Therefore, with a higher fracture energy, if fracture propagation is harder to generate, fracture fluid tends to diffuse into the rock. As shown in Figure 4.24, the loss rate is very similar.

4.4.3 Effect of Tensile Strength

The definition of tensile strength presented here is the normal tensile strength of the cohesive element to initiate damage. As shown in Figure 4.25 and Figure 4.26, tensile strength shows the same effects as fracture energy.

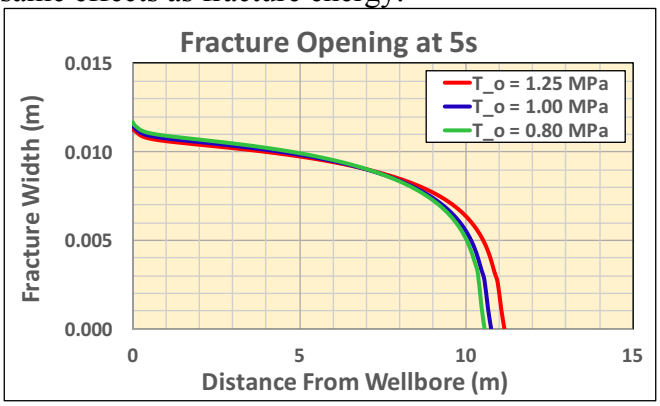

Figure 4.25: Effect of tensile strength on final fracture geometry.

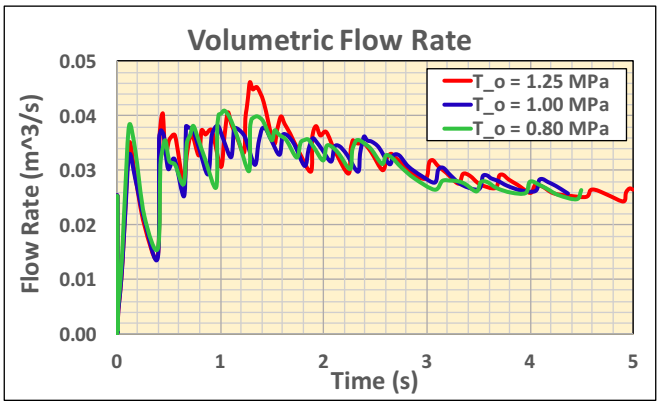

Figure 4.26: Effect of tensile strength on volumetric flow rate.

4.4.4 Effect of Rock Permeability

With a higher permeability, more fluid is driven into the rock system as the formation pore pressure is the same and wellbore pressure is set the same and constant (as shown in Figure 4.28). Therefore, a wider, longer fracture is generated by a higher loss rate in the base case (as shown in Figure 4.27).

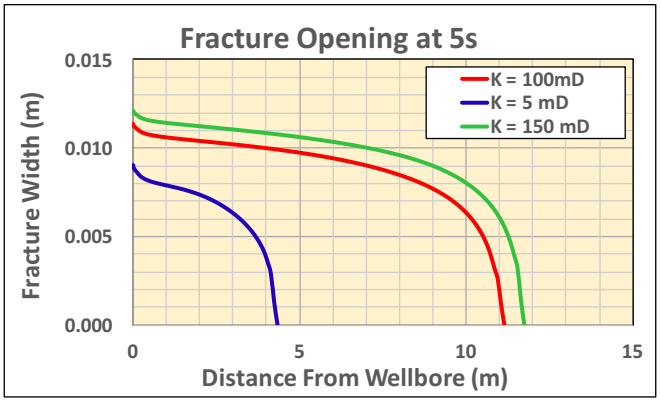

Figure 4.27: Effect of rock permeability on final fracture geometry.

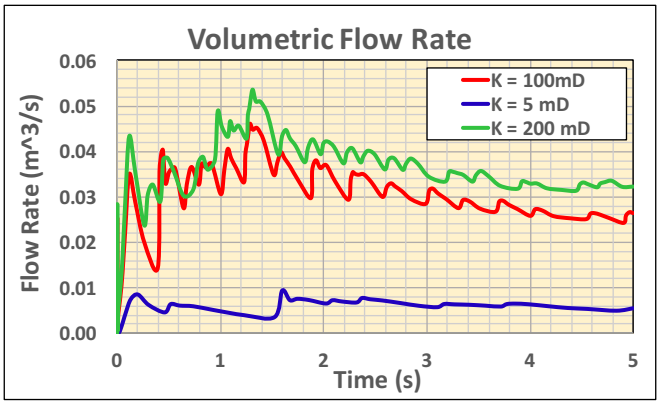

Figure 4.28: Effect of rock permeability on volumetric flow rate.

4.5 Study on Downhole Conditions

Studying downhole conditions includes the in-situ stress field, depleted pore pressure, mud pressure, and mud viscosity. For depleted pore pressure, total stress is assumed constant, which in turn changes the effective stresses for different cases.

4.5.1 Effect of Stress Anisotropy

In results of this work, stress anisotropy has negligible influence on final fracture geometry. The volumetric flow rate is very similar among all three cases. If the same minimum horizontal stress is assumed and the maximum horizontal stress is altered, fracture propagation should be theoretically identical. However, the base case has a slightly

larger total volume of fluid flowed into the system, which results in a minor difference in length compared to other cases. Therefore, the longer length of the base model is not a representative phenomenon.

In theory, a larger horizontal stress contrast leads to a greater stress concentration at the wellbore, and FIP under such conditions is lower. Because a constant wellbore pressure significantly higher than the FIP is employed, the more noticeable influence of FIP is bypassed.

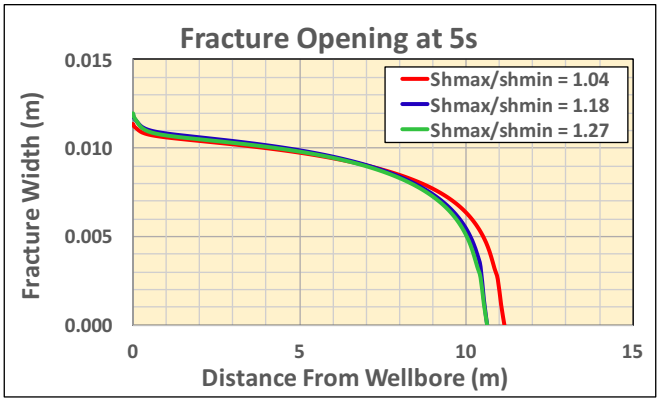

Figure 4.29: Effect of stress anisotropy on final fracture geometry.

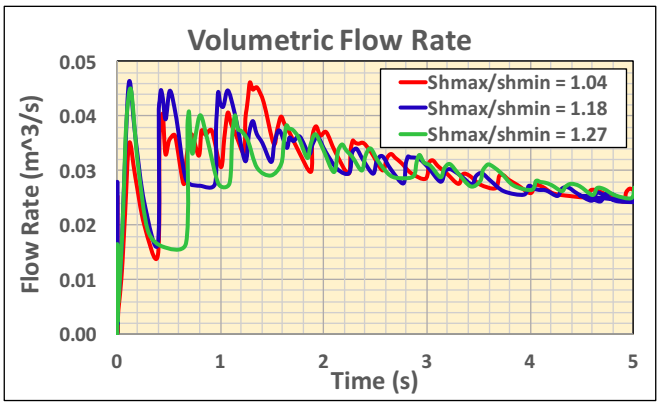

Figure 4.30: Effect of stress anisotropy on volumetric flow rate.

4.5.2 Effect of Pore Pressure

Because minimum horizontal stress (a total stress) does not change, fracture propagation is not influenced. However, a lower pore pressure raises the differential pressure between fracture fluid and pore fluid so that more fluid leaks off into the formation. Therefore, a shorter fracture length is generated when pore pressure is low (as shown in Figure 4.31).

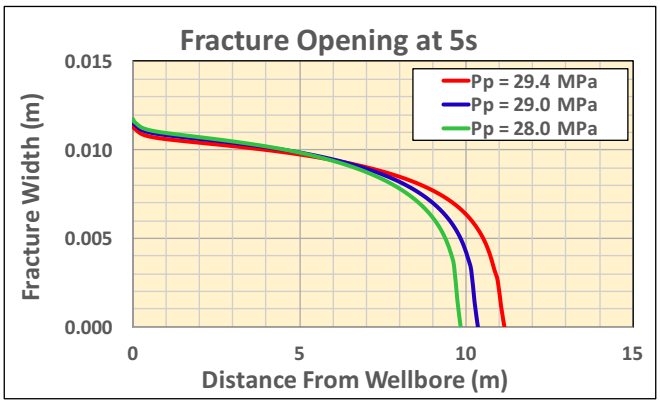

Figure 4.31: Effect of pore pressure on final fracture geometry.

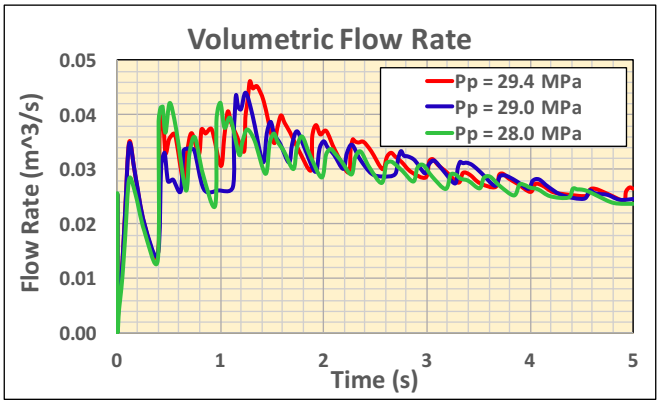

Figure 4.32: Effect of pore pressure on volumetric flow rate.

The fracture mouth opening for a low-pore-pressure case is slightly bigger, but the loss rates are very similar. Thus, pore pressure does not influence the rate of mud loss (as shown in Figure 4.32).

4.5.3 Effect of Wellbore Pressure (Equivalent Circulating Density)

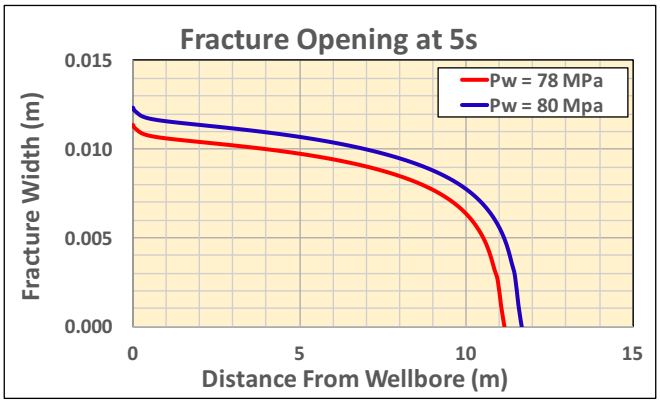

Figure 4.33: Effect of equivalent circulating density on final fracture geometry.

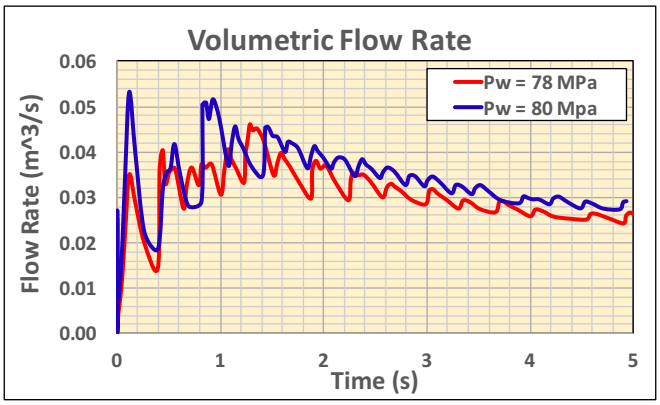

Figure 4.34: Effect of equivalent circulating density on volumetric flow rate.

There are three cases studied on wellbore pressure (i.e., ECD). The above figures show predictable results from two extremely overbalanced scenarios. A higher ECD leads to more fluid flow into the rock system and consequently generates a bigger fracture geometry.

For the third case, a wellbore pressure equivalent to the average FPP obtained from the injection case is applied. No fracture extension is observed in this case. The effective hoop stress in the vicinity of the wellbore is reduced due to elevated traction applied at the wellbore surface. Mud cake sufficiently isolates the rock matrix from mud seepage loss.

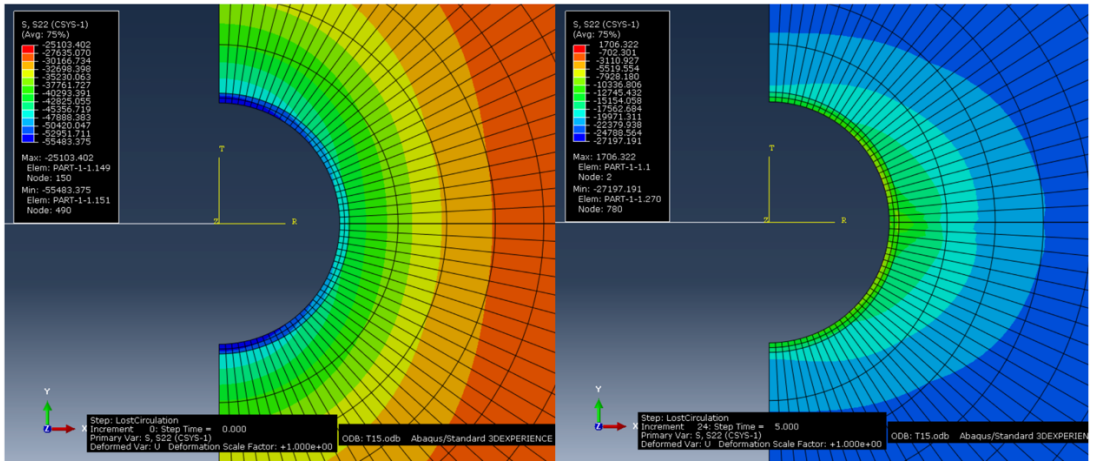

Figure 4.35: Effective hoop stress after drilling (left) and after fluid pressurization (right). No fracture extension occurs when P_{well} = fracture propagation pressure.

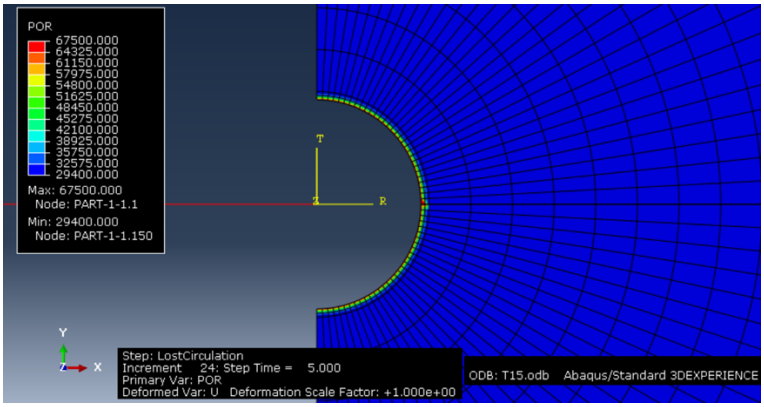

Figure 4.36: Pore pressure distribution after 5 seconds when P_{well} = fracture propagation pressure. Mud cake zonal isolation performance is noteworthy.

Arch geometry, first implemented by ancient Romans for construction, naturally dissipates loading into compression form along its tangential direction (generates hoop stress), which reduces tensile loading at the structure. From the above simulation results, FPP does not initiate fracture extension. This phenomenon proves a great wellbore strength—holding fluid pressure. Therefore, it is suggested that using FPP as the fracture gradient for a safe MWW is operationally feasible, but is not applicable for a fractured wellbore.

4.5.4 Effect of Mud Cake Permeability

As mud cake mechanical behavior is ignored, cake only provides zonal isolation at the wellbore surface. Thus, fluid tends to flow into the fracture rather than to the wellbore surface. As shown in Figure 4.37, no major difference in final fracture geometry is made by cake permeability. Figure 4.38 shows the exact same volumetric flow rate among these three cases. Therefore, it is concluded that permeability damage at the wellbore surface has no influence on lost circulation; lost circulation is dominated by fluid losses through opening fractures.

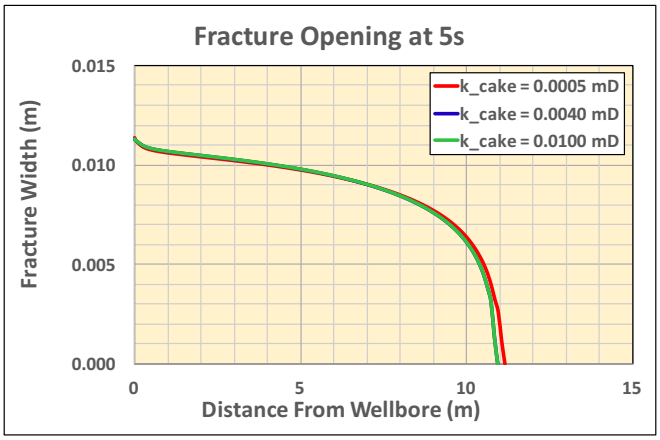

Figure 4.37: Effect of mud cake permeability on final fracture geometry.

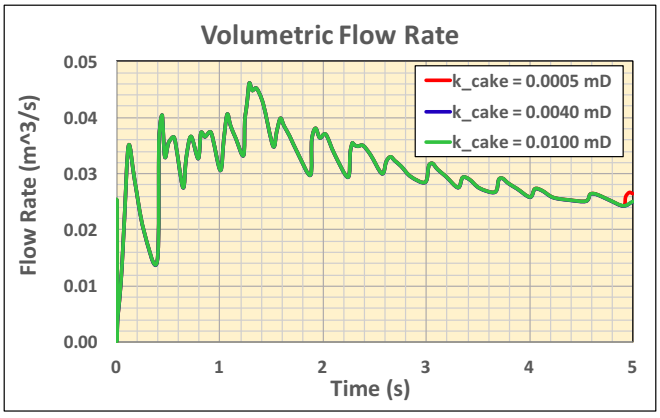

Figure 4.38: Effect of mud cake permeability on volumetric flow rate.

4.5.5 Effect of Leak-Off at Fracture Surface

When leak-off coefficient is lowered, more fluid stays within the fracture space and is implemented to propagate the fracture. Therefore, a lower leak-off rate results in a wider and longer fracture (as shown in Figure 4.39).

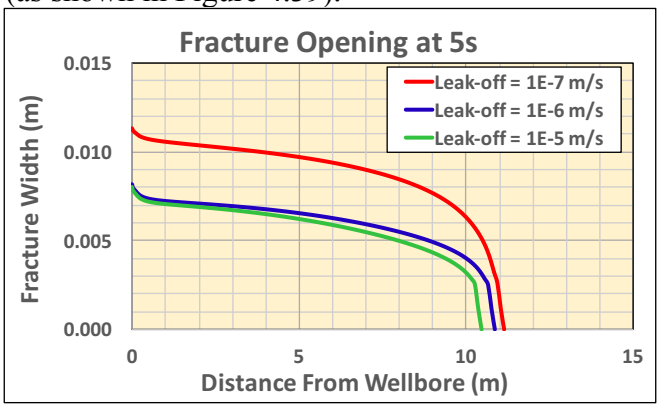

Figure 4.39: Effect of leak-off coefficient on final fracture geometry.

Early volumetric flow rates behave differently (as shown in Figure 4.40). A higher leak-off rate stimulates fluid seepage at the fracture surface, and fracture mouth width increases faster at the early time (as shown in Figure 4.9). Hence, the fracture can take more fluid coming in under the same ECD and causes a larger volumetric flow rate earlier. However, after the fracture mouth width stabilizes at a later time, volumetric flow rate is not influenced by leak-off.

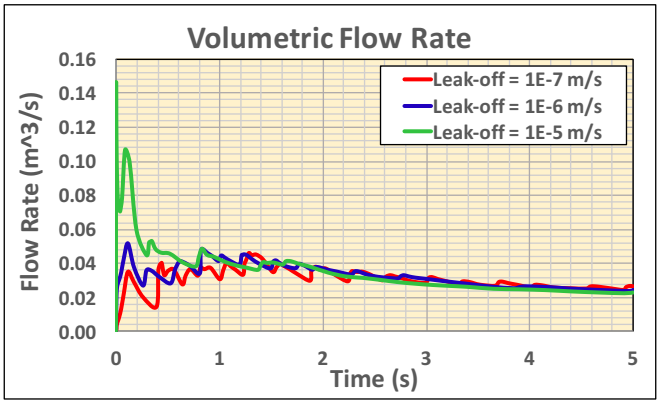

Figure 4.40: Effect of leak-off coefficient on volumetric flow rate.

4.5.6 Effect of Mud Viscosity

In Figure 4.41, increasing mud viscosity increases fracture width and decreases fracture length because a larger friction pressure loss occurs when fluid flows from the wellbore to the fracture tip. A larger fluid pressure drop is induced by a more viscous fluid. Therefore, fluid near the wellbore with a higher pressure applies a larger traction at the fracture surface, which in turn widens the fracture. On the other hand, because fluid pressure near the tip is low, strain energy buildup tends to become weak and fracture propagation tends to be depressed. In Figure 4.42, the rates of mud loss from the three cases are very similar and mud viscosity has no effect on loss rate.

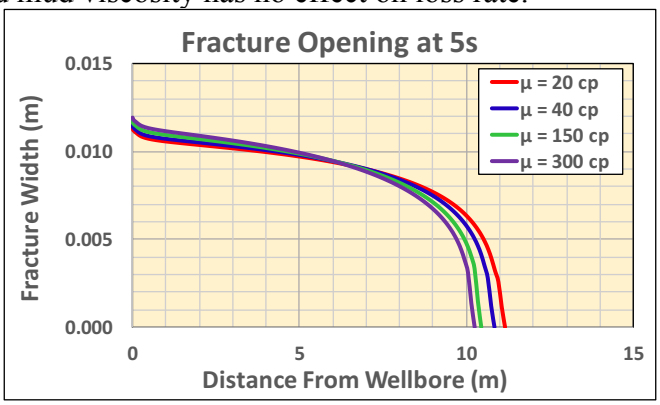

Figure 4.41: Effect of mud viscosity on final fracture geometry.

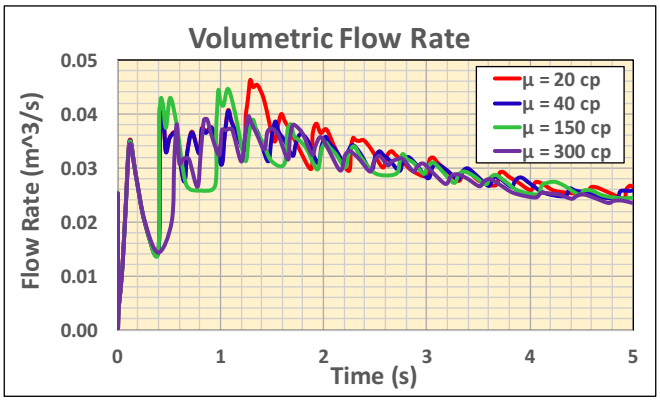

Figure 4.42: Effect of mud viscosity on volumetric flow rate.

4.6 Discussion of the Results

Parameter	Fracture Width	Fracture Length	Loss Rate	Testing Range
Young's Modulus ↑	↓	↑	↓	1e7 - 2e7 KPa
Fracture Toughness ↑	↑	↓	No	1.02 - 2.89 MPa*sqrt(m)
Tensile Strength ↑	↑	↓	No	0.8 - 1.25 MPa
Rock Permeability ↑	↑	↑	↑	5 - 150 mD
Stress Anisotropy ↑	No	No	No	1.04 -1.27
Pore Pressure ↑	No	↑	No	29.4 - 28 MPa
Wellbore Pressure(ECD) ↑	↑	↑	↑	68 - 80 MPa
Mud Cake ↑	No	No	No	0.0005 - 0.01 mD
Leak-off Coefficient ↑	↓	↓	No	10 - 0.1 mD (equivalent)
Mud Viscosity ↑	↑	↓	No	20 - 300 cp

Table 4.4: Summary of observations from the parametric study. Highlighted parameters are manageable in drilling operations.

The base case is analyzed and compared to an injection test simulation. The induced fracture from lost circulation (i.e., ECD-induced fracturing) is much longer and wider than that from the injection test. Since fracture fluid pressure and wellbore pressure are almost the same, constant wellbore pressure, as a boundary condition, drives mud to flow into the fracture to compensate for the fracture fluid pressure drop from leaking off and from new fracture volume generated by propagation. Furthermore, the simulations of lost circulation indicate that, even for a short period of time, the induced fracture can propagate a significant distance (beyond 6 in.) from the wellbore.

Increasing rock stiffness results in a narrower and longer fracture, because a higher stiffness tends not to deform and aids strain energy buildup at the fracture tip. As a result, due to the narrow width, loss rate is less for a higher-stiffness rock. Studying the rock's mechanical properties also highlights the effect of fracturing criteria, in which a higher fracture critical energy or a higher tensile strength contributes more resistance in fracture propagation and results in a shorter fracture length. However, these two rock properties cannot be modified in drilling operations.

Mud loss rate is significantly influenced by rock permeability, which is expressed by hydraulic conductivity in the simulation, and a higher ECD fosters a bigger volume of mud loss into a rock system. Therefore, mud loss rate is mainly controlled by the hydraulic conductivity of the rock matrix and the differential pressure driving the fluid flow.

Within the fracture domain, the volume of fracture fluid and fracture fluid pressure play an important role on final fracture geometry. When fluid leak-off at the fracture surface is restricted or when fracture fluid is less viscous, more fluid flows to the fracture tip and increases tensile concentration at the tip. As a result, strain energy buildup at the fracture tip becomes easier and stimulates fracture propagation. On the other hand, a higher fracture fluid pressure generates a higher surface traction that further widens the fracture opening. Because leak-off rate and mud viscosity can be controlled by adjusting mud formulation, these properties might be the breakpoints to resolve lost circulation.

From simulation results in this work, hoop stress enhancement is proved true. Also, high rock stiffness can assist hoop stress enhancement. However, pore pressure elevation substantially depresses the enhanced hoop stress due to fracture opening and overrides further hoop stress buildup due to a higher stiffness. In fact, there is total hoop stress enhancement from the intact wellbore to the fractured wellbore at the early time, but part of the wellbore surface later experiences a reduction in total hoop stress as the fracture is further widened. Because the simulation of lost circulation assumes a highly permeable rock, assumes a Biot's coefficient of 1, and does not consider pore fluid dissipating away from the near-wellbore region, enhancement of effective hoop stress was not captured, but an enhancement of total hoop stress was observed at an early time. Therefore, hoop stress is enhanced as a fracture is widened for a linear elastic material, with reservations regarding the time-dependent poroelastic effect, where undesired pore pressure eliminates stress buildup by widening the fracture.

4.7 HIGHLIGHTS OF THE CHAPTER

- An extensive parametric study on lost circulation is conducted with respect to various rock properties and bottomhole conditions.
- During lost circulation, ECD-induced fracture length can be several meters, even in a short time period.
- Fracture energy and tensile strength of rock show minimal influences on the severity of lost circulation at an intact wellbore.
- Hydraulic conductivity of the rock matrix and fluid pressure driving the fluid dictate the rate of mud loss.
- Induced fracture length reduces as more fluid dissipates to the rock matrix and as more fracture fluid pressure loss is generated by viscous fluid.
- Hoop stress enhancement is possible when the fracture is open. However, it requires efficient fluid dissipation in the target site to mitigate the poroelastic effect.
- Rock stiffness impacts the amount of hoop stress buildup.

Chapter 5: Fracture Resistance Enhancement Mechanism

In this chapter, a novel simulation approach is presented that integrates the fracture resistance enhancement mechanism into the hydraulic fracturing simulation. The goal of this approach is to quantify immobile mass performance with respect to fracture gradient extension. This chapter first introduces the methodology we developed and a recommended workflow. Then, a case study on fracture sealing conditions, which implements the workflow, is discussed. The case study separately investigates permeability and length of immobile mass with guidance from the tip screen-out model (a preventive treatment) and the FCS model (a remedial treatment). The case study is on modeling reopening of a sealed fracture. Finally, insights from simulation results and operational suggestions on optimizing fracture resistance enhancement are summarized.

5.1 Simulation of Fracture Resistance Enhancement

Drilling in narrow MWWs, such as in depleted zones, requires sufficient hydrostatic pressure to prevent fluid influx and wellbore collapse so that minimum mud weight is inherently invariant. To resolve such an operational challenge, WBS offers the capability of widening the MWW by artificially lifting the fracture gradient (or the upper limit of the mud weight). From the parametric study, hoop stress enhancement is observed as the wellbore is wedged by the fracture opening, along with an elevation of fracture propagation resistance as mud rheology is modified. Nevertheless, hoop stress enhancement is regressed by pore pressure elevation, and its benefits are confined to poroelastic rock. Therefore, the fracture resistance enhancement mechanism is further investigated toward developing a methodology to quantify benefits from this mechanism regarding fracture gradient.

By screening parametric effects, mud viscosity and leak-off quantity (i.e., coefficient) are both found to be favorable for fracture resistance enhancement and to be operationally feasible. In this study of leak-off coefficient, it was found that fracture leak-off at the fracture surface dissipates hydraulic power within the fracture and weakens the tendency for fracture propagation. In this study of mud viscosity, it was found that a viscous fluid requires a high differential pressure to drive fluid flow to the tip and ultimately reduces propagation rate and fracture length.

The tip screen-out method and the FCS method, which mention protection of the fracture tip, are revisited here. Even though the two methods suggest different operational philosophies, both suggest a certain volume of solids deposition within the fracture aperture. Similar to the mud viscosity measuring fluid's frictional pressure loss, an immobile mass compressed by LCM can inhibit longitudinal fluid flow within a fracture (as shown in Figure 5.1).

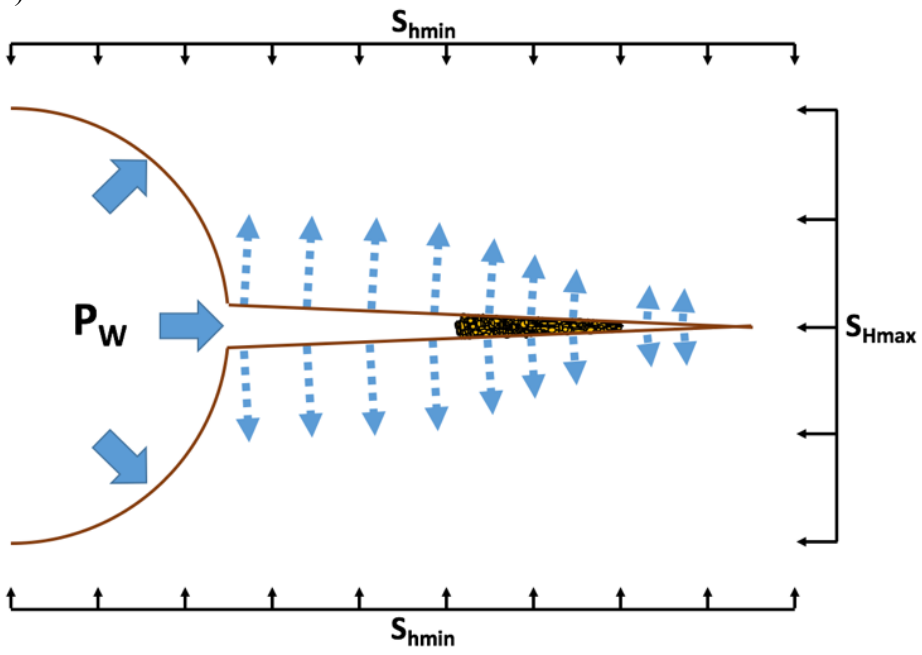

Figure 5.1: Schematic of fracture resistance enhancement mechanism. The dashed blue arrow represents fluid leak-off. The solid arrow indicates wellbore pressure.

Once an immobile mass forms inside a fracture, less fluid flows through the immobile mass to the isolated part of the fracture, where leak-off rate is also lessened. Consequently, fluid pressure at the isolated section equalizes with nearby pore pressure and stress intensity at the tip reduces. After all of this, fracture resistance is enhanced.

To simulate this phenomenon, a novel simulation approach is used that practically and exclusively considers the reduction of longitudinal fracture fluid flow due to particle plugging (i.e., the immobile mass) inside the fracture aperture. This approach is based on Abaqus modeling resources, but can be adapted to any other fracture simulator. Specifically, Reynold's equation is implemented for modeling tangential fluid flow rather than Darcy's equation modeling linear fluid flow in porous media. From experiments, measured immobile mass permeability is converted to the initial hydraulic conductivity of the fracture fluid. Because hydraulic conductivity increases as fracture aperture widens, immobile mass permeability is actually smaller than the defined value. Therefore, the approach quantifies fracture resistance in a conservative manner.

Reynold's equation constitutes tangential fracture fluid flow as follows:

$$q_f = -\frac{g^3}{12\mu_f}\frac{\partial p_f}{\partial s}$$

where μ_f is the fracture fluid viscosity, and g is the width of fracture aperture. Darcy's equation constitutes linear fluid in an immobile mass (i.e., porous media) as follows:

$$\mathrm{q} = -\frac{kA}{\mu}\frac{\partial p}{\partial s}$$

Then, the hydraulic diffusive term from Darcy's equation to the hydraulic conductivity term in Reynold's equation is equalized as follows:

$$\frac{g_{initial}{}^3}{12\mu_f} = \frac{kA_{initial}}{\mu_{filtrate}}$$

Finally, the above equation is reorganized as follows:

$$\mu_f{}^* = \frac{g_{initial}{}^3 \mu_{filtrate}}{12kA_{initial}}$$

assuming the width of fracture aperture g as the initial width $g_{initial}$ after the material is fractured (i.e., $g_{initial}$ = 0.002 m = 2000 um is a default value in Abaqus), where $A_{initial}$ = $g_{initial}$×1m = 0.002 m^2 is the initial cross-section area of fracture assuming plain-strain thickness of 1m, $\mu_{filtrate}$ is the filtrate viscosity (i.e., water viscosity is used) assuming blended LCM does not influence mud rheology, and $\mu_f{}^*$ is the modified viscosity of fracture fluid and an input parameter in "Gap Flow" of Abaqus.

5.2 Workflow of Fracture Gradient Extension Quantification

A recommended workflow of fracture gradient extension quantification is presented here to utilize this novel simulation approach (as shown in Figure 5.2).

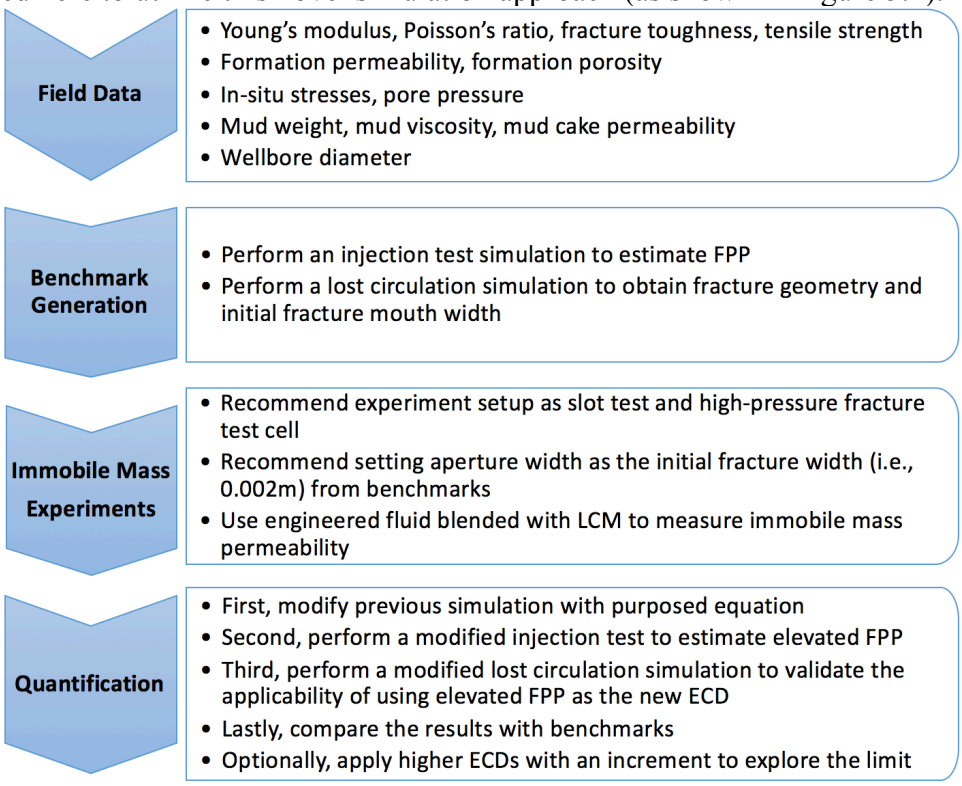

Figure 5.2: Recommended workflow for fracture gradient extension quantification.

The process begins with collecting field data for the formation and the fluid. From the parametric study, fracture energy and tensile strength show a minor influence on lost circulation. Therefore, these parameters, which are often not well known during drilling operations, can be omitted. But rock stiffness and formation permeability are very important in generating the following simulation and must be carefully evaluated.

After the input values are specified, two benchmark cases are conducted using Abaqus. An injection test simulation is necessary for estimating a more realistic FPP, considering in-situ stress conditions as well as mud pressure frictional loss inside the fracture and fluid diffusion to the rock matrix. For lost circulation simulation, using analytical breakdown pressure is recommended. Because lost circulation most likely happens when breakdown pressure is reached, breakdown pressure results are useful for consequent WBS analysis.

In the experiments of immobile mass, it is suggested to singularly measure immobile mass permeability, which is the focus point of this approach. Even though there is potential particle-rock interaction in forming the immobile mass, the new approach is more engineering-driven and avoids further complexity. This reasoning also serves as the ideological basis for the new approach. Experiments on a slot disk (Wang et al. 2016) or high-pressure fracture test cell (Kaageson-Loe et al. 2009) offer setup simplicity. Also, if the experiment setup allows, an artificial fracture aperture width of 0.002 m (i.e., a default value of initial fracture width in Abaqus) is recommended. The immobile mass, which is the particle aggregation formed by LCM and small particles in drilling fluid, is expected to be viscoelastic, cohesive to rock surface, and able to sustain a high external load or a large deformation without dissipation.

The last stage is to simulate fracture resistance and quantify fracture gradient extension by analyzing results. Because immobile mass is predefined in the model, it

simulates the fracture reopening after WBS treatment (including both preventive and remedial treatment) for assessment in drilling operations. First, the cohesive element is predamaged (i.e., using initial gap) based on the lost circulation simulation in the previous stage. Then, according to individual preference or field experience, a portion of predamaged fracture is modified with customized mud viscosity calculated from the proposed equation given. The desired ECD of post-WBS treatment is input in the simulation. The WBS treatment succeeds if no severe fracture propagation occurs during the simulation time. Alternately, Figure 5.2 presents another route to explore the potential for particle sealing. Because ECD flocculation induces the majority of lost circulation, the simulation time can be the tripping time for each pipe connection or the longest time of excessive mud pressure applied to the wellbore.

A systematic workflow is presented that couples the effect of particle plugging to a robust fracture simulator. A few limitations still exist, including not simulating fracture height growth, ignoring transport and aggregation mechanisms of immobile mass, disregarding the mechanical strength of immobile mass that describes the dissipation of packed particles due to fracture aperture movement and creeping movement, and not considering time-dependent fracture surface permeability damage. These limitations demonstrate challenges for improving simulation models in the near future.

This workflow can be adopted to optimize field operations and provide practical insights for the drilling community. Meanwhile, any suggestion or critique to improve the approach are welcome.

5.3 Study on Fracture Sealing Conditions

A method and a simulation workflow to the base model from Chapter 4 quantifies fracture propagation resistance. The following section discusses the results of fracture resistance enhancement on various sealing lengths and permeabilities.

5.3.1 A Case Study on Sealing Permeability

The case study on sealing permeability is guided by the tip screen-out model. Tip screen-out originated from the DEA-13 project and is mostly applied as a preventive treatment for lost circulation. Its sealing condition is to have particle aggregation in the narrow fracture tip zone (as shown in Figure 2.12), which inhibits fracture fluid invasion to the tip.

For this case study, the fracture is predamaged with respect to the final fracture length of the base case, which is about 11 m. Simulation setup of the base case can be found in Chapter 4. An immobile mass (i.e., LCM) with a length of 0.5 m is placed 1.5 m behind the fracture tip (as shown in Figure 5.3). Table 5.1 shows different permeability values assigned to the immobile mass

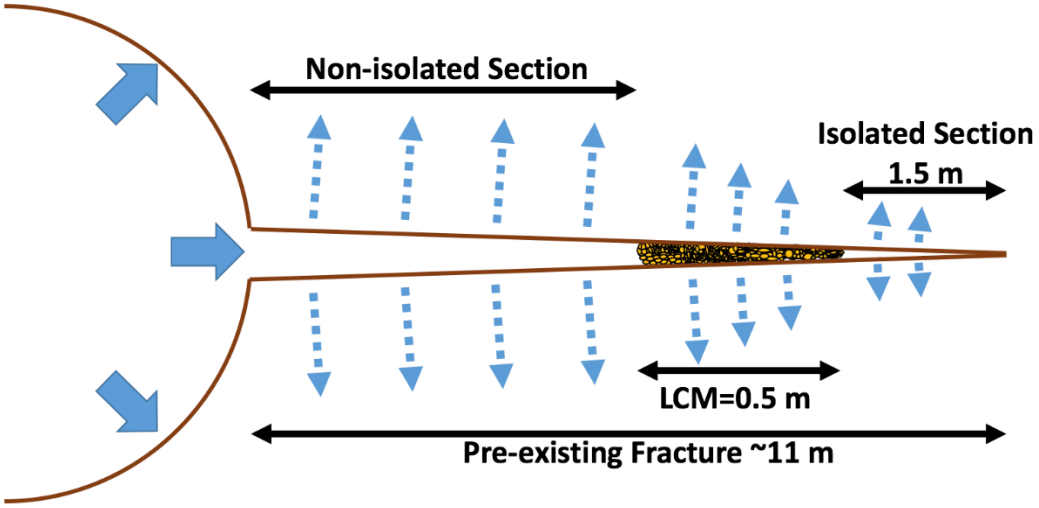

Figure 5.3: The immobile mass placement used in the case study of sealing permeability.

Case #	k_LCM (mD)	k_LCM (m^2)	g_initial (m)	μ_filtrate (KN*S*M^-2)	A_initial (m^2)	μ*_f (KN*S*M^-2)	ECD (MPa)
P-1	50	5E-14	0.002	1.00E-06	0.002	6.667	90
P-2	500	5E-13	0.002	1.00E-06	0.002	0.667	90
P-3	5000	5E-12	0.002	1.00E-06	0.002	0.067	90

Table 5.1: List of inputs for the case study on sealing permeability.

Similar to the parametric study, a fracture re-opening injection test for Case P-1 is performed to detect the signature of tip screen-out with respect to injection pressure and fracture fluid pressure. The same injection condition of Case 4 in the parametric study (as shown in Figure 4.6) is applied for 60 seconds. As shown in Figure 5.4.A, FPP constantly increases during injection. The injection pressure of Case P-1 elevates beyond the average FPP of Case 4 after 20 seconds, showing an enhancement of fracture resistance. The simulated phenomenon is consistent with the experimental data from the DEA-13 project (as shown in Figure 5.4.B) and published LOT data. The difference between this work and others' is the assumption that the LCM is assumed to be immobile. The green line in Figure 5.4.B records the initial injection using drilling fluid, and the red line records the secondary injection to reopen the induced fracture by using LCM-blended drilling fluid.

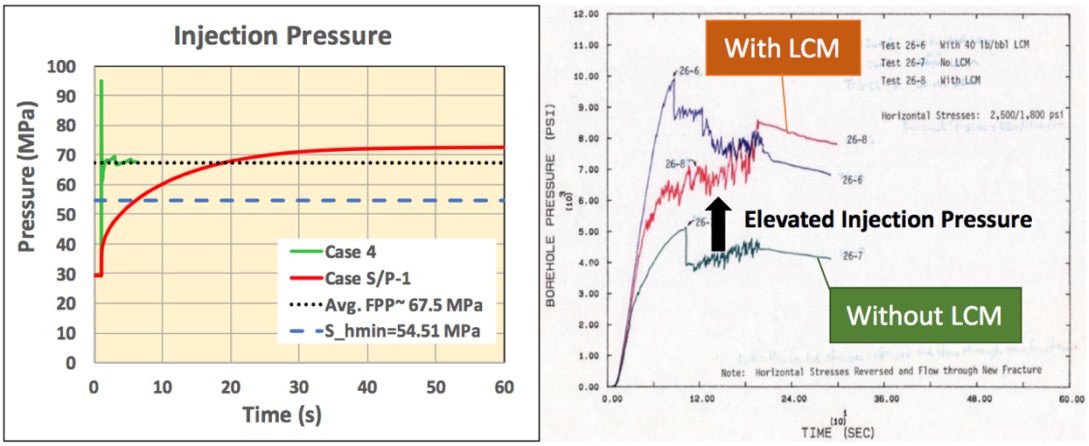

(A) (B)

Figure 5.4: (A) Simulated injection pressure from Case P-1. (B) DEA-13 fracturing experiment data show an elevation of injection pressure (Black et al. 1985).

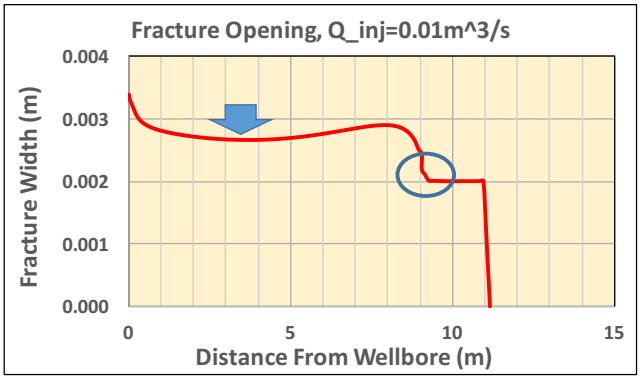

Figure 5.5: Final fracture geometry for Case P-1 after 60-second injection.

The final fracture geometry shows compelling results—the blue-circled area where the LCM is located has a minor opening with no width increasing at the isolated fracture section. Most importantly, no further fracture propagation is observed, indicating the success of tip isolation and enhanced fracture resistance.

The reduction of width in the middle of the fracture, labeled by the blue arrow in Figure 5.5, is due to the poroelastic back-stress. Because fracture propagation is mitigated and fracture fluid exclusively leaks off to the rock matrix, part of the fracture experiences a longer period of fluid invasion so that the pore pressure elevates higher (as shown in Figure 5.6). Hence, high pore pressure tends to dilate the porous medium and generates more compressive backstress, which tends to close the fracture.

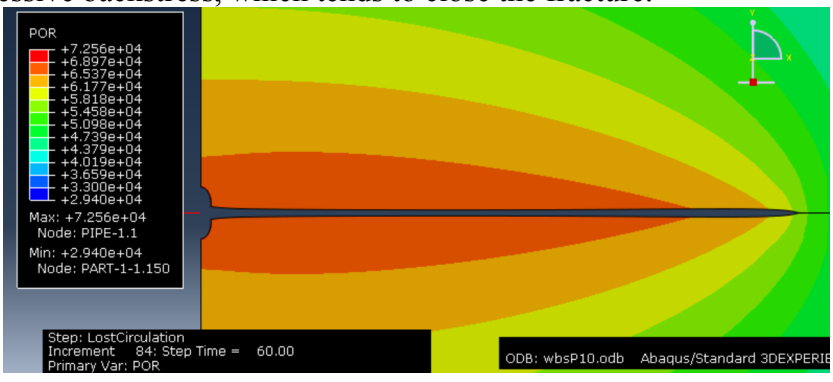

Figure 5.6: Pore pressure distribution near the fracture for Case P-1 after 60-second injection. Deformation is magnified 150 times.

Lost circulation simulation models fracture reopening with an ECD of 90 MPa, which is 12 MPa higher than the ECD of inducing the preexisting fracture. Under such a high fluid pressure, the results of lost circulation simulation are considerable. Figure 5.7 shows the fracture geometry after 60 seconds. The green box labels the LCM location.

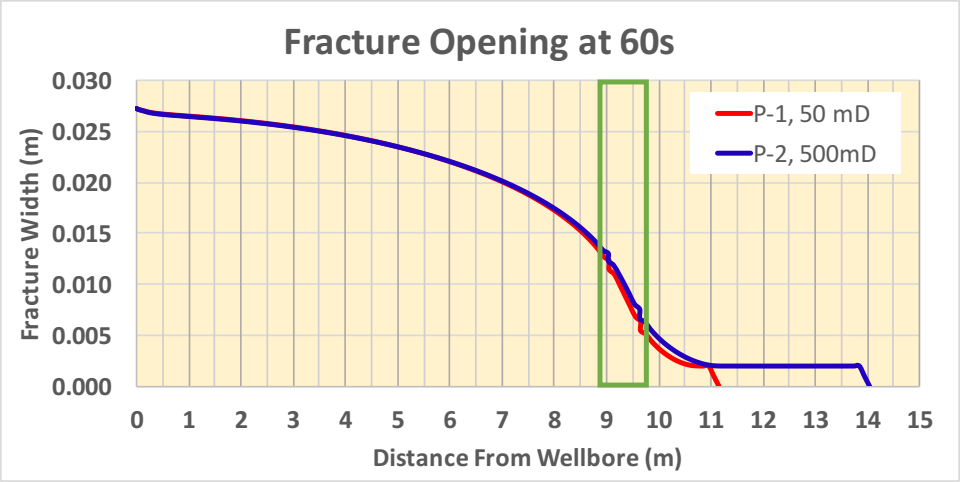

Figure 5.7: Comparison of final fracture geometry between Cases P-1 and P-2.

Case P-1, with 50-mD permeability, presents a great capability of tip isolation, where no further propagation appears. In Case P-2, with 500-mD permeability, fracture propagation resumes at about 9 seconds. However, as additional fracture surface is generated at the isolated section, the reduced fluid influx can momentarily dissipate into the rock matrix and fracture growth is inhibited at 40 seconds. These two cases both have a narrow fracture width at the isolated section, and the wellbore is strengthened in both cases. The simulation of Case P-3, with 5000-mD permeability, is aborted before 60 seconds because the fracture propagates to the external boundary. Lost circulation happens again at about 2 seconds. Even though fracture resistance enhancement fails, the fracture fluid pressure and the fracture geometry after resuming propagation are highly illustrative of the fracture resistance enhancement mechanism (as shown in Figure 5.8).

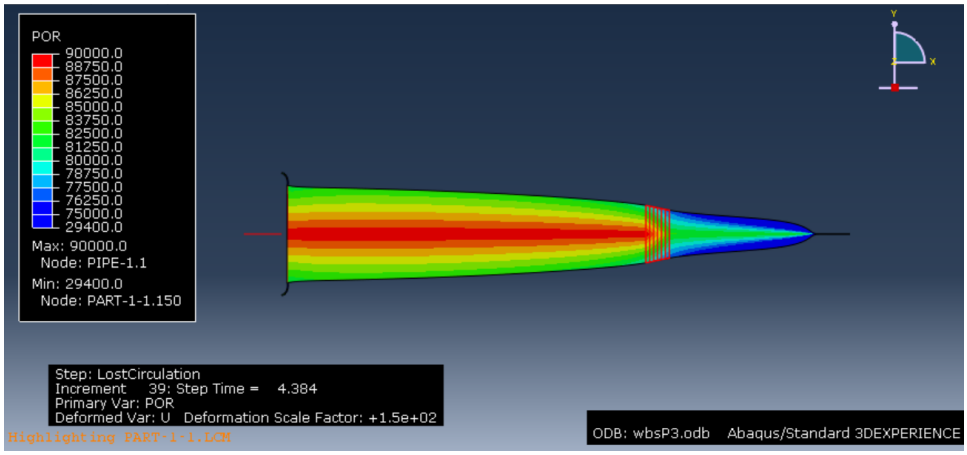

Figure 5.8: Fracture fluid pressure at 4 seconds from Case P-3. The immobile mass is highlighted with red mesh. Deformation is magnified 150 times.

In the above figure, a distinguished pressure drop is shown across the LCM, the fracture width at the isolated section is significantly reduced, and the fracture width at the non-isolated section is very large. Figure 5.9 shows the reduction of fracture fluid pressure through the LCM, as well as the effect of LCM permeability on the fluid pressure inside the isolated section.

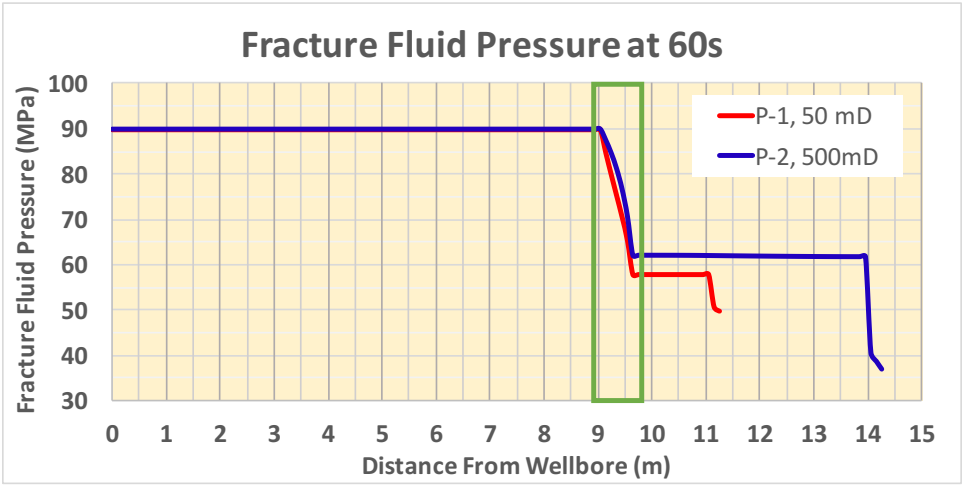

Figure 5.9: Comparison of fracture fluid pressure between Cases P-1 and P-2.

The rates of mud loss from Cases P-1 and P-2 (as shown in Figure 5.10) are very close. Case P-2, with a higher permeability, induces ~0.2 m^3 more in total loss volume than Case P-1, but both cases show mitigated fracture propagation at 60 seconds. In Figure 5.10, the early peak indicates the completed re-opening of the non-isolated fracture section. Then, the drop in flow rate indicates fracture plugging by the LCM, which constrains the longitudinal fracture fluid flow.

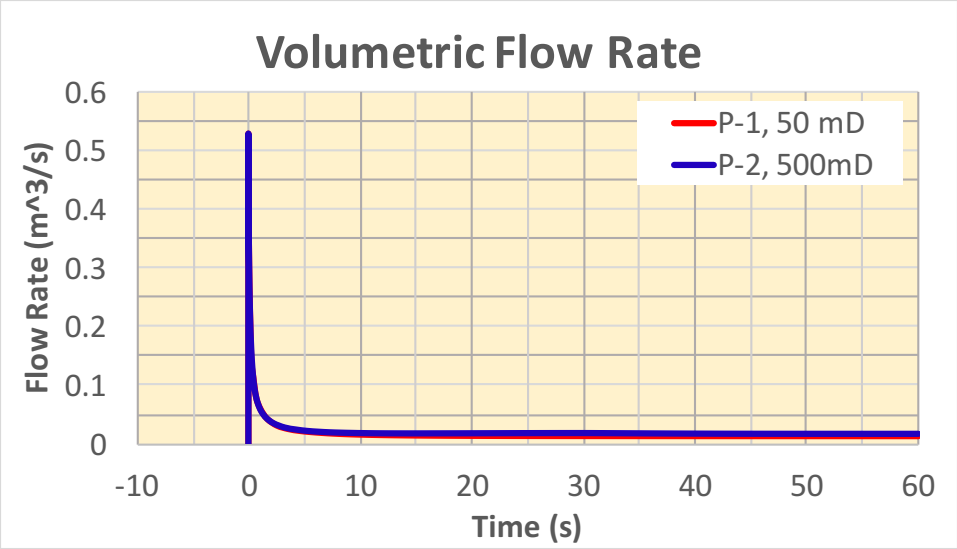

Figure 5.10: Comparison of fluid loss rate between Cases P-1 and P-2.

5.2.2 A Case Study on Sealing Length

The case study on sealing length is guided by the FCS model. Even though FCS has two objectives (i.e., tip isolation and fracture closing stress enhancement), this study only focuses on the tip isolation benefits of this remedial treatment. FCS instructs a hesitation squeezing operation that generates a larger volume of immobile mass than tip screen-out does. The sealing condition of this model has a large portion of fracture in the near-wellbore region to be plugged by the LCM (as shown in Figure 2.10).

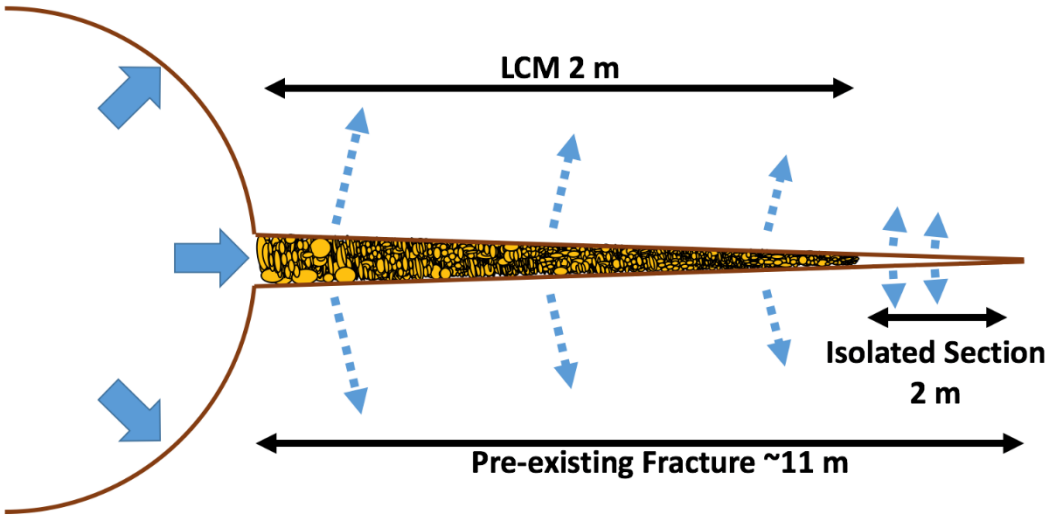

Figure 5.11: The immobile mass placement used in the case study of sealing length.

For this case study, the fracture is predamaged with respect to the final fracture length of the base case. An immobile mass (i.e., LCM) with a length of 9 m is placed 2 m behind the fracture tip (as shown in Figure 5.11). ECD is set at 90 MPa. Table 5.2 shows different permeability values assigned to the immobile mass.

Case #	k_LCM (mD)	k_LCM (m^2)	g_initial (m)	μ_filtrate (KN*S*M^-2)	A_initial (m^2)	μ*_f (KN*S*M^-2)	ECD (MPa)
L-1	50	5E-14	0.002	1.00E-06	0.002	6.667	90
L-2	500	5E-13	0.002	1.00E-06	0.002	0.667	90
L-3	5000	5E-12	0.002	1.00E-06	0.002	0.067	90

Table 5.2: List of inputs for the case study on sealing length.

With the same permeability values and increments as the previous case study, the overall fracture sealing capability improves remarkably as sealing length increases. As expected, Cases L-1 and L-2 both show small fracture widths in the near-wellbore region, where L-1, with the lowest permeability, has about 0.4 m of reopened fracture (as shown in Figure 5.12). Case P-3, with 5000-mD permeability of tip screen-out configuration, fails to prevent lost circulation. However, with a much longer LCM length, only 0.5 m of new

fracture is induced in Case L-3. Fracture propagation occurs at 45 seconds in Case L-3, while it occurs at 2 seconds in Case P-3. The significant delay of resuming propagation is caused by the length of the LCM. Similar to Case P-2, with 500-mD permeability of tip screen-out configuration, the newly induced propagation soon mitigates as enough fracture surface is generated to dissipate the fracture fluid to rock. Overall, all three cases show the success of WBS.

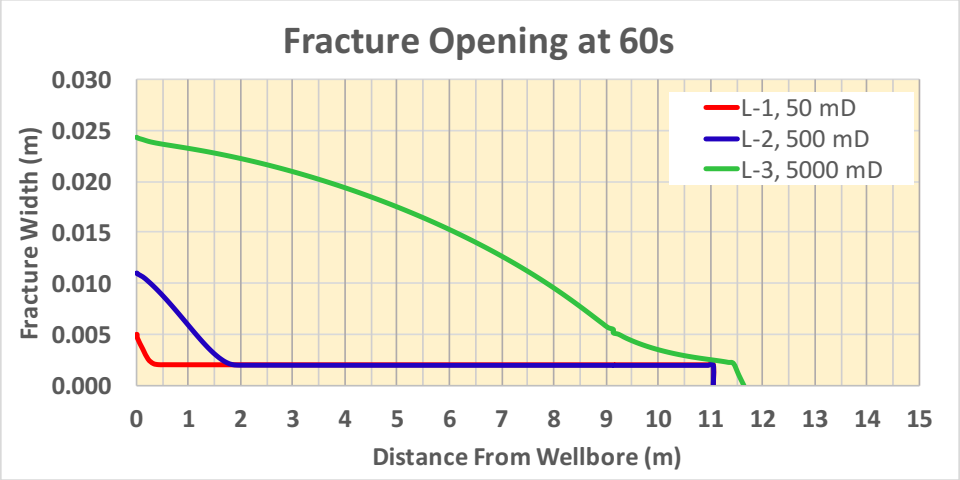

Figure 5.12: Comparison of final fracture geometry among Cases L-1, L-2, and L-3.

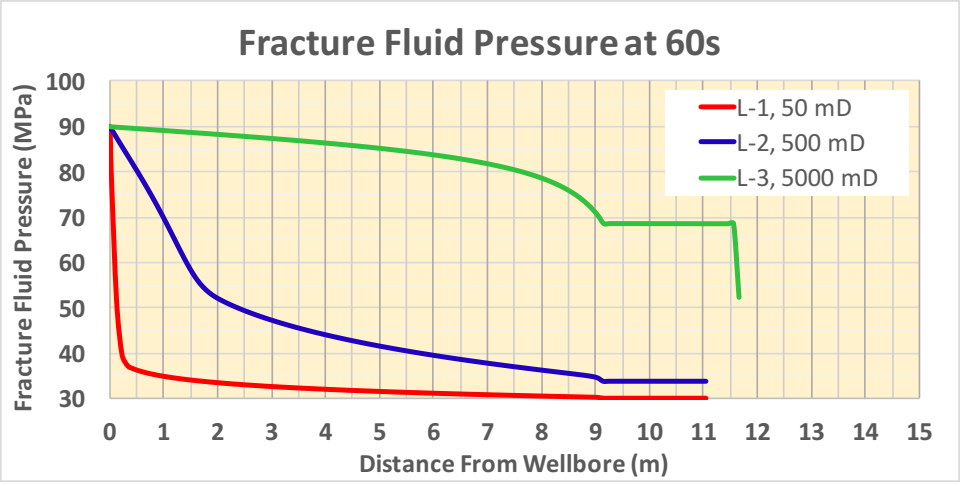

Figure 5.13: Comparison of fracture fluid pressure among Cases L-1, L-2, and L-3.

Fracture fluid pressure along the fracture length is shown in Figure 5.13. As permeability decreases, fracture fluid pressure drops sharply. In Case L-3, even though the fracture fluid pressure at the isolated section is about two times higher than the other two cases, it still cannot produce enough strain energy at the tip and is more or less under an equilibrium condition of "barrel in, barrel out."

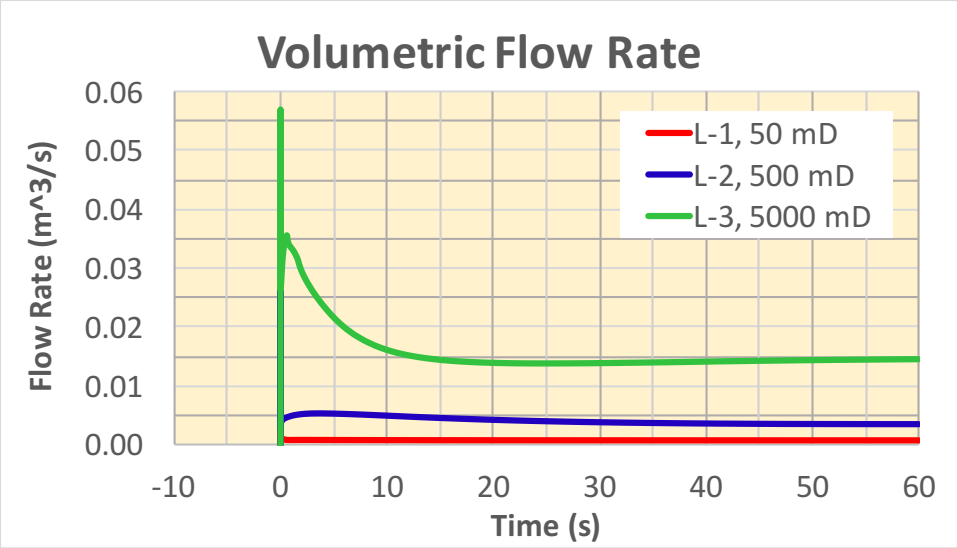

Figure 5.14: Comparison of fluid loss rate among Cases L-1, L-2, and L-3.

Figure 5.14 shows the fluid loss rates of the three cases. Despite the highest permeability by orders of magnitude in Case L-3, the LCM length compensates for the deficiency of fluid flow constraint and yields a drastic reduction of fluid loss rate similar to the other two. In addition, Case L-1, with the lowest permeability, merely induces ~0.09 m^3 of total mud loss, which is ~1 m^3 less total loss than Case P-1.

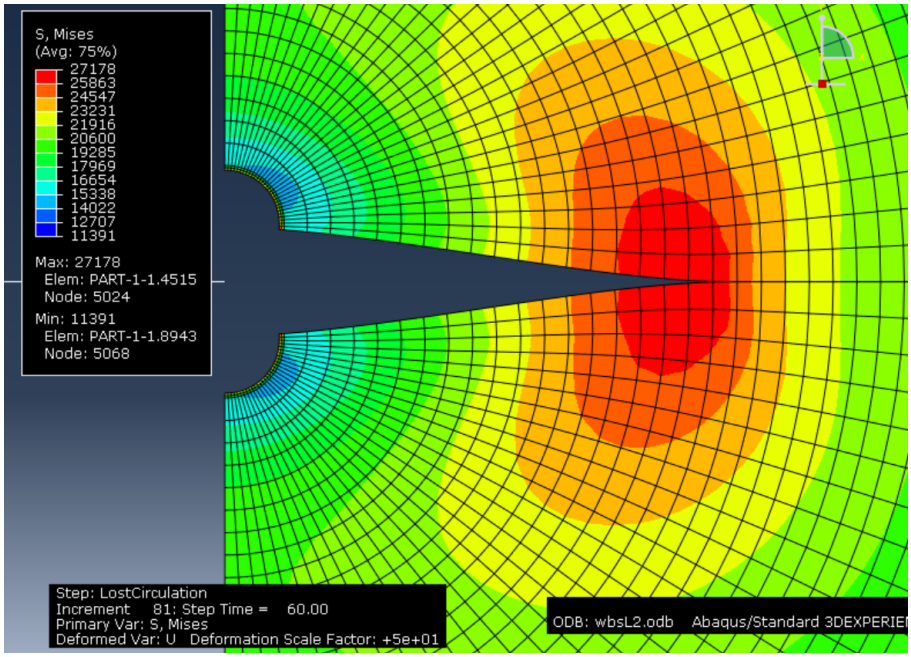

Figure 5.15: Von Mises stress at 60 seconds from Case L-2. Deformation is magnified 50 times.

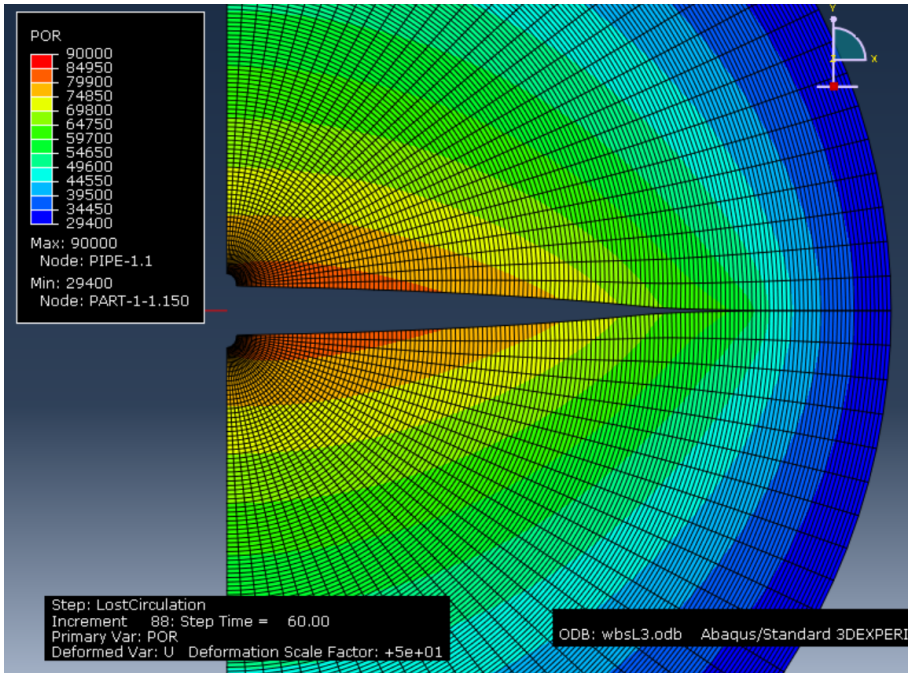

Figure 5.16: Pore pressure at 60 seconds from Case L-3. Deformation is magnified 50 times.

5.4 Discussion of the Results

An injection simulation is performed first. The injection pressure after sealing is elevated above the average FPP of the base case. The trends of the simulated injection pressures are consistent with the experimental data. No further propagation is observed during injection. Fracture width reduction is observed due to poroelastic effect.

A distinguished fracture fluid pressure drop in the immobile mass is observed in all cases. Decreasing immobile mass permeability or increasing immobile mass length aids tip protection and contributes to fracture resistance enhancement. However, it is a compounded effect that generates fracture resistance. This means that immobile mass length and permeability are mutually beneficial for enhancing fracture resistance.

Some sealing cases reflect a resumption of fracture propagation. However, fracture propagation stops after generating enough opening surface to allow fluid to dissipate to the rock matrix, which in turn mitigates stress intensity at the tip. In addition, the existence of immobile mass inside the fracture can delay the fracture propagation time.

Rate of mud loss is significantly reduced after sealing. Even with a high-permeability immobile mass, the reduction of volumetric flow rate is phenomenal. Overall, rate of mud loss depends on the seal capability that constrains the fluid flow inside the fracture.

Suggestions for WBS treatment can be derived from these simulation results. Preventive treatment, which continuously keeps LCM within the drilling fluid, is always beneficial because a minimal amount of LCM can effectively increase the apparent FPP. For remedial treatment, the squeezing volume of LCM should be carefully estimated because a larger isolated fracture space actually assists fluid leak-off to the rock matrix and ultimately mitigates additional strain energy buildup at the fracture tip. For the same reason, injection rate during the squeezing treatment should be maintained as low as possible,

giving more time for fracture fluid dissipation in the vicinity of the fracture tip. To maximize fracture resistance, LCM should be designed with a low permeability after deposition. Moreover, even with a high-permeability LCM, increasing LCM concentration for a longer sealing length can compensate such a deficiency of material.

5.5 HIGHLIGHTS OF THE CHAPTER

- A systematic workflow of fracture gradient extension quantification is demonstrated.
- Injection pressure elevated above FPP is due to the constraint of fracture fluid flow.
- Reducing immobile mass permeability and extending seal length enhance fracture resistance.
- Permeability and length are mutually beneficial for optimizing tip isolation.
- Additional fracture length stabilizes the fracture fluid pressure buildup in the isolated section, which in turn inhibits fracture propagation.
- Suggestions for WBS treatment are detailed.

Chapter 6: Summary, Conclusions, and Recommendations

In this chapter, the summary and conclusion for this thesis are presented, followed by recommendations for future work.

6.1 SUMMARY AND CONCLUSIONS

The summary and conclusion of this research are as follows:

1. A fully coupled hydraulic fracturing model is developed on Abaqus Standard finite element analysis software. The accuracy of the numerical model is enforced by a convergent study. The meticulous simulation setup enables a more realistic simulation of lost circulation and WBS. A parametric study is performed to investigate impacts of various rock properties and bottomhole conditions on lost circulation. A novel approach to quantify fracture gradient extension due to fracture resistance enhancement is proposed and is followed by a case study on fracture sealing conditions.
2. The parametric study on rock properties first emphasizes the competition between induced strain energy at the fracture tip and fracturing criteria, where a high Young's modulus accelerates strain energy buildup and where high fracture energy and high tensile strength improve fracturing resistance. However, rock properties are uncontrollable during drilling operations.
3. Mud loss rate is significantly influenced by rock permeability, which is expressed by hydraulic conductivity in the simulation, and a higher ECD fosters a bigger volume of mud loss into a rock system. Therefore, mud loss rate is mainly controlled by the hydraulic conductivity of the rock matrix and the differential pressure driving the fluid flow. With a higher loss rate, a wider and longer fracture is generated.
4. Regarding fluid flow inside the fracture, conclusions are derived from studies on leak-off coefficient and mud viscosity. When fluid leak-off to the rock matrix is restricted

or when fracture fluid is less viscous, fracture fluid buildup at the fracture tip accelerates and, in turn, fosters fracture propagation. In drilling operations, fluid loss control and mud viscosity can be modified with mud formulation. These parameters are possible alternatives for WBS. The observation from mud viscosity lays the foundation for development of the proposed simulation approach of WBS.

5. Hoop stress enhancement is validated by comparing total hoop stress from multiple time frames. Effective hoop stresses do not show any elevation among the cases. Hence, the role of poroelastic effect is emphasized and indicates the requirement for dissipating pore pressure. The analysis of hoop stress enhancement also indicates that an elevated Young's modulus further increases hoop stress.
6. A proposed novel simulation approach honors the fracture resistance enhancement mechanism aiming for tip protection. The approach modifies the viscosity term in Reynold's equation in order to model fluid flow within an immobile mass. Conservative assumptions are made for the modification. A workflow to quantify extended fracture gradient is demonstrated.
7. Based on the approach and workflow, a case study on fracture sealing conditions investigates the effect of sealing permeability and sealing length. Results show the decline of fracture fluid pressure across the immobile mass. The fracture width at the isolated section is much smaller than the non-isolated section. The rate of mud loss is sharply reduced after fracture sealing.
8. According to the results, length and permeability of immobile mass are mutually beneficial in enhancing fracture resistance.
9. As fluid leaks off to rock matrix, a certain length of opening surface in the vicinity of fracture tip can also assist lost circulation mitigation.

10. By comparing results of the injection test and lost circulation from both studies, the induced fracture geometry from lost circulation is much bigger than the one induced from the injection because a constant excessive pressure stimulates fluid loss through the propagating fracture. The fracture lengths simulated by the fully coupled hydraulic fracturing model can be as much as two orders of magnitude longer than the commonly assumed 6-in. fracture. After the fracture is effectively sealed with immobile mass, injection pressure can elevate above the FPP without triggering further propagation.
11. Suggestions for WBS treatment emphasize the benefits of fracture sealing and the interplay among sealing permeability, sealing length, and fluid leak-off in the vicinity of the fracture tip.

6.2 RECOMMENDATIONS FOR FUTURE WORK

1. A large-scale 3D simulation is suggested. Because a very large width is induced in the current 2D model, the effects of fracture sealing in a 3D model are unknown. An additional simulation step to model elevated pore pressure dissipation will provide more guidance on the hoop stress enhancement mechanism.
2. Investigation of LCM transport and deposition pattern within the fracture is suggested. Up to now, this WBS study is constrained by personal judgements of LCM placement. No doubt, these judgements can be biased by not considering the transport mechanism of LCM. Therefore, understanding LCM placement is an urgent demand to further develop the WBS model.
3. Investigation of LCM mechanical strength is also necessary. Various rupture mechanisms of mud cake are mentioned in the thesis. A mud-cake-like LCM aggregation might perform differently inside the narrow fracture. Extensive use is made of the term “immobile mass” to describe LCM aggregation inside the fracture and is

also assumed immobile in this work. But this might not be the real case as the simulation model shows a wide fracture opening during lost circulation.

4. Based on current understanding of fracture modeling, a more realistic time-dependent leak-off model can be included in the model. Due to lack of understanding of formation damage at the fracture surface, it is not considered in this work. Further investigation of formation damage at the fracture surface by drilling fluid is recommended and will not only benefit modeling WBS, but also the well-being of the future production phase.
5. The results emphasize the fracture sealing capability of WBS. Therefore, an optimized PSD that generates minimum hydraulic conductivity at the fracture requires further investigation for field applications.
6. Experimental or field validation is necessary for the application of the proposed model.

Nomenclature

A	Cross-section area
α_P	Biot's coefficient
E	Young's modulus
f	Body forces (excluding fluid weight) per unit volume
G_C	Fracture energy
g	Fracture aperture width
I	Unit matrix
K	permeability
$\widehat{K}$	Hydraulic conductivity
K_I	Stress intensity factor
K_{IC}	Critical stress intensity factor/ fracture toughness
P_p	Pore pressure
P_w, P_{well}	Wellbore pressure
p_f	Fracture fluid pressure
p_{ini}	Fracture initiation pressure
q_f	Tangential flow rate of fracture fluid across the fracture
r	Distance from wellbore center
r_w	Wellbore radius
S	Total stress tensor
$\tau_{r\theta}$	Effective shear stress
σ_{ij} or S^*	Effective normal stress
S_{Hmax}	Maximum horizontal total stress
S_{hmin}	Minimum horizontal total stress

S_v	Vertical total stress
t	Surface tractions per unit area
T, N_o, T_o	Tensile strength
μ_f	Fracture fluid viscosity
$\mu_f{}^*$	Modified fracture fluid viscosity
v	Poisson's ratio
v_T, v_B	Normal fluid flow velocities through fracture surface
$\boldsymbol{v_w}$	Average velocity of pore fluid
δ_{ij}	Kronecker delta
ρ_w	density of pore fluid
η	Poroelastic parameter of rock
ϕ	Porosity

Greek Symbols

α, β, and γ	Eulerian angles defining the rotation of principal stress tensor
δ	Azimuth of the wellbore measured clockwise from geographic north
ϕ	Deviation of the wellbore with respect to the vertical direction
θ	Angle measured clockwise from bottom of wellbore

Subscripts/Superscripts

r, θ, z	Wellbore radial coordinate system
1,2,3	Principal coordinate system
T,B	Top, Bottom

Acronyms

CZM	Cohesive zone model
ECD	Equivalent circulating density
EMW	Equivalent mud weight
FCS	Fracture closure stress
FIP	Fracture initiation pressure
FPP	Fracture propagation pressure
FPR	Fracture propagation resistance model
FST	Formation strength test
LCM	Lost circulation material
LEFM	Linear elastic fracture mechanics
LOT	Leak-off test
LPM	Loss prevention material
MWW	Mud weight window
OBM	Oil based mud
PSD	Particle size distribution
SFG	Shear failure gradient
TVD	Trure vertical depth
WBM	Water based mud
WBS	Wellbore strengthening
WPC	Wellbore pressure containment
XLOT	Extended leak-off test
2D	Two-dimensional
3D	Three-dimensional

Acronyms (Abaqus Standard)

FP2D2	2-node linear fluid pipe element
COH2D4P	6-node displacement and pore pressure two-dimensional cohesive element
CPE4P	4-node bilinear displacement and pore pressure element
PORMECH	Mechanical pore pressure loads on coupled pore pressure elements
CFLOW	Prescribing node-based seepage flow
SDEG	Scalar stiffness degradation variable

References

Aadnoy , B.S., Belayneh, M., Jorquera, M.A.A. et al. 2008. Design of Well Barriers To Combat Circulation Losses. SPE Drilling & Completion 23 (3). SPE-105449-PA. http://dx.doi.org/10.2118/105449-PA.

Abaqus Analysis User's Manual, 2016, Version 2016, Dassault Systèmes Simulia Corp., Providence, Rhode Island.

Alberty, M.W. and McLean, M.R. 2004. A Physical Model for Stress Cages. Presented at the SPE Annual Technical Conference and Exhibition, Houston, Texas, 26—29 September. SPE-90493-MS. http://dx.doi.org/10.2118/90493-MS.

Alberty, M.W. and McLean, M.R. 2014. The Use of Modeling To Enhance the Analysis of Formation-Pressure Integrity Tests. SPE Drilling & Completion 29 (4). SPE-167945-MS. http://dx.doi.org/10.2118/167945-MS.

Anderson, T.L. 2005. Fracture mechanics: fundamentals and applications. Taylor&Francis.

Aston, M.S., Alberty, M.W., and McLean, M.R. 2004. Drilling Fluids for Wellbore Strengthening. Presented at the IADC/SPE Drilling Conference, Dallas, Texas, 2—4 March. SPE-87130-MS. http://dx.doi.org/10.2118/87130-MS.

Aston, M.S., Alberty, M.W., and Duncum , S.D. 2007. A New Treatment for Wellbore Strengthening in Shale. Presented at the SPE Annual Technical Conference and Exhibition, Anaheim, Montana, 11—14 November. SPE-110713-MS. http://dx.doi.org/10.2118/110713-MS.

Black, A, et al. 1985. DEA 13 (Phase I) Final Report: Investigation of Lost Circulation Problems and Apparent Fracture Gradient Reduction Encountered in the Field with Oil-Based Drilling Fluids During Large-Scale Laboratory Fracturing Experiences.

Box, G.E.P. and Draper, N.R. 1987. Empirical Model Building and Response Surfaces. New York, New York: John Wiley&Sons.

Bradley, W.B. 1979. Failure of Inclined Boreholes. Journal of Energy Resources Technology 101 (4): 232—239. http://dx.doi.org/10.115/1.3446925.

Cook, J., Guo, Q., Way , P. et al. 2016. The Role of Filtercake in Wellbore Strengthening. Presented at the IADC/SPE Drilling Conference and Exhibition, Fort Worth, Texas, 1—3 March. SPE-178799-MS. http://dx.doi.org/10.2118/178799-MS.

Dupriest, F.E. 2005. Fracture Closure Stress (FCS) and Lost Returns Practices. Presented at the SPE/IADC Drilling Conference, Amsterdam, Netherlands, 23—23 February. SPE-92192-MS. http://dx.doi.org/10.2118/92192-MS.

Ewy, R.T. 1998. Wellbore Stability Predictions Using a Modified Lade Criterion. Presented at the SPE/ISRM Rock Mechanics in Petroleum Engineering, Trondheim, Norway, 8—10 July. SPE-47251-MS. http://dx.doi.org/10.2118/47251-MS.

Feng, Y., Arlanoglu, C., Podnos, E. et al. 2015. Finite-Element Studies of Hoop-Stress Enhancement for Wellbore Strengthening. SPE Drilling & Completion 30 (1). SPE-168001-PA. http://dx.doi.org/10.2118/168001-PA.

Feng, Y., Jones, J.F., and Gray, K.E. 2016. A Review on Fracture-Initiation and -Propagation Pressures for Lost Circulation and Wellbore Strengthening. SPE Drilling & Completion 31 (2). SPE-181747-PA. http://dx.doi.org/10.2118/181747-PA.

Fjaer, E., Holt, R.M., Horsrud, P. et al. 2008. Petroleum related rock mechanics, second edition. Elsevier.

Fuh, G.-F., Morita, N., Boyd, P.A. et al. 1992. A New Approach to Preventing Lost Circulation While Drilling. Presented at the SPE Annual Technical Conference and Exhibition, Washington, DC, 4—7 October. SPE-24599-MS. http://dx.doi.org/10.2118/24599-MS.

Haddad, M. and Sepehrnoori, K. 2014. Simulation of Multiple-Stage Fracturing in Quasibrittle Shale Formations Using Pore Pressure Cohesive Zone Model. Presented at the Unconventional Resources Technology Conference, Denver, Colorado, 25—27 August. SPE-2014-1922219-MS. http://dx.doi.org/10.2118/2014-1922219-MS.

Haimson, B. and Fairhurst, C. 1967. Initiation and Extension of Hydraulic Fractures in Rocks. SPE Journal 7 (3). SPE-1710-PA. http://dx.doi.org/10.2118/1710-PA.

Hubbert, M.K. and Willis, D.G. 1957. Mechanics Of Hydraulic Fracturing. Petroleum Transactions, AIME 210: 153—168.

Jaeger, J.C., Cook, N.G.W., and Zimmerman, R.W. 2007. Fundamentals of rock mechanics. Wiley-Blackwell.

Jaffal, H.A. 2016 Evaluation of mudcake buildup and its mechanical properties. MS thesis, The University of Texas at Austin

Kaageson-Loe, N., Sanders, M.W., Growcock, F. et al. 2009. Particulate-Based Loss-Prevention Material--The Secrets of Fracture Sealing Revealed!. SPE Drilling & Completion 24 (4). SPE-112595. http://dx.doi.org/10.2118/112595.

Kostov, N., Ning, J., and Gosavi, S.V. 2015. Advanced Drilling Induced Fracture Modeling for Wellbore Integrity Prediction. Presented at the SPE Annual Technical Conference and Exhibition, Houston, Texas, 28 January—30 September. SPE-174911-MS. http://dx.doi.org/10.2118/174911-MS.

Lee, D., Bratton, T., and Birchwood, R. 2004. Leak-Off Test Interpretation And Modeling With Application To Geomechanics. Presented at the North America Rock Mechanics Symposium, Houston, Texas, 5—9 June. ARMA-04-547.

Morita, N., Black, A.D., and Guh, G.-F. 1990. Theory of Lost Circulation Pressure. Presented at the SPE Annual Technical Conference and Exhibition, New Orleans, Louisiana, 23—26 September. SPE-20409-MS. http://dx.doi.org/10.2118/20409-MS.

Morita, N., Black, A.D., and Fuh, G.-F. 1996. Borehole breakdown pressure with drilling fluids—I. Empirical results. International Journal of Rock Mechanics and Mining Sciences&Geomechanics Abstracts 33 (1). http://dx.doi.org/10.1016/0148-9062(95)00028-3.

Morita, N. and Fuh, G.F. 2012. Parametric Analysis of Wellbore-Strengthening Methods From Basic Rock Mechanics. SPE Drilling & Completion 27 (2). SPE-145765-PA. http://dx.doi.org/10.2118/145765-PA.

Ning, J., Kao, G., Kostov, N. et al. 2015. Experimental Validation of Simulation Capabilities for Hydraulic Fractures Propagation in a Porous Medium. Presented at the 2015 SIMULIA Community Conference, Berlin, Germany.

Okland, D., Gabrielsen, G.K., Gjerde, J. et al. 2002. The Importance of Extended Leak-Off Test Data for Combatting Lost Circulation. Presented at the SPE/ISRM Rock Mechanics Conference, Irving, Texas, 20—23 October. SPE-78219-MS. http://dx.doi.org/10.2118/78219-MS.

Onyia, E.C. 1994. Experimental Data Analysis of Lost-Circulation Problems During Drilling With Oil-Based Mud. SPE Drilling & Completion 9 (1). SPE-22581-PA. http://dx.doi.org/10.2118/22581-PA.

Peska, P. and Zoback, M.D. 1995. Compressive and tensile failure of inclined well bores and determination of in situ stress and rock strength. J. Geophys. Res 100 (NaN). http://dx.doi.org/10.1029/95JB00319.

Postler, D.P. 1997. Pressure Integrity Test Interpretation. Presented at the SPE/IADC Drilling Conference, Amsterdam, Netherlands, 4—6 March. SPE-37589-MS. http://dx.doi.org/10.2118/37589-MS.

Razavi, O., Vajargah, A.K., Van Oort, E. et al. 2015. How to Effectively Strengthen Wellbores in Narrow Drilling Margin Wells: An Experimental Investigation. Presented at the SPE Annual Technical Conference and Exhibition, Houston, Texas, 28—30 September. SPE-174976-MS. http://dx.doi.org/10.2118/174976-MS.

Schmitt, D.R. and Zoback, M.D. 1989. Poroelastic effects in the determination of the maximum horizontal principal stress in hydraulic fracturing tests—A proposed breakdown equation employing a modified effective stress relation for tensile failure. International Journal of Rock Mechanics and Mining Sciences 26 (6): 499—506. http://dx.doi.org/10.1016/0148-9062(89)91427-7.

Shin, D. and Sharma, M.K. 2014. Factors Controlling the Simultaneous Propagation of Multiple Competing Fractures in a Horizontal Well. Presented at the SPE Hydraulic Fracturing Technology Conference, The Woodlands, Texas, 4—6 February. SPE-168599-MS. http://dx.doi.org/10.2118/168599-MS.

Song, J. and Rojas, J.C. 2006. Preventing Mud Losses by Wellbore Strengthening. Presented at the SPE Russian Oil and Gas Technical Conference and Exhibition, Moscow, Russian, 3—6 October. SPE-101593-MS. http://dx.doi.org/10.2118/101593-MS.

van Oort, E. and Vargo, R.F. 2008. Improving Formation-Strength Tests and Their Interpretation. SPE Drilling & Completion 23 (3). SPE-105193-MS. http://dx.doi.org/10.2118/105193-MS.

van Oort, E., Friedheim, J.E., Pierce, T. et al. 2011. Avoiding Losses in Depleted and Weak Zones by Constantly Strengthening Wellbores. SPE Drilling & Completion 26 (4). SPE-125093-PA. http://dx.doi.org/10.2118/125093-PA.

van Oort, E. and Razavi, S.O. 2014. Wellbore Strengthening and Casing Smear: The Common Underlying Mechanism. Presented at the IADC/SPE Drilling Conference and Exhibition, Fort Worth, Texas, 4—6 March. SPE-168041-MS. http://dx.doi.org/10.2118/168041-MS.

Wang, H., Towler, B.F., and Soliman, M.Y. 2007. Near Wellbore Stress Analysis and Wellbore Strengthening for Drilling Depleted Formations. Presented at the Rocky Mountain Oil&Gas Technology Symposium, Denver, Colorado, 16—18 April. SPE-102719-MS. http://dx.doi.org/10.2118/102719-MS.

Wang, H., Soliman, M.Y., and Towler, B.F. 2009. Investigation of Factors for Strengthening a Wellbore by Propping Fractures. SPE Drilling & Completion 24 (3). SPE-112629-PA. http://dx.doi.org/10.2118/112629-PA.

Wang, H., Savari, S., Whitfill , D.L. et al. 2016. Forming a Seal Independent of Formation Permeability to Prevent Mud Losses—Theory, Lab Tests, and Case Histories. Presented at the IADC/SPE Drilling Conference and Exhibition, Fort Worth, Texas, 1—3 March. SPE-178790-MS. http://dx.doi.org/10.2118/178790-MS.

Wang, H., Marongiu-Porcu, M., and Economides, M.J. 2016. Poroelastic and Poroplastic Modeling of Hydraulic Fracturing in Brittle and Ductile Formations. SPE Production & Operations 31 (1). SPE-168600-MS. http://dx.doi.org/10.2118/168600-MS.

Yao, Y., Gosavi, S.V., Searles, K.H. et al. 2010. Cohesive Fracture Mechanics Based Analysis to Model Ductile Rock Fracture. Presented at the 44th U.S. Rock Mechanics Symposium and 5th U.S.-Canada Rock Mechanics Symposium, Salt Lake City, Utah. ARMA-10-140.

Yew, C.H. and Weng, X. 2014. Mechanics of Hydraulic Fracturing. Elsevier Science.

Zhang, J. and Roegiers, J.C. 2005. Double Porosity Finite Element Method for Borehole Modeling. Rock Mechanics and Rock Engineering 38 (3). http://dx.doi.org/10.1007/s00603-005-0052-9.

Zhang, J., Standifird, W.B., and Lenamond, C. 2008. Casing Ultradeep, Ultralong Salt Sections in Deep Water: A Case Study for Failure Diagnosis and Risk Mitigation in Record-Depth Well. Presented at the SPE Annual Technical Conference and Exhibition, Denver, Colorado, 21—24 September. SPE-114273-MS. http://dx.doi.org/10.2118/114273-MS.

Zhang, J. 2011. Pore pressure prediction from well logs: Methods, modifications, and new approaches. Earth-Science Reviews 108 (1-2): 50—63. http://dx.doi.org/10.1016/j.earscirev.2011.06.001.

Zielonka, M.G., Searles, K.H., Ning, J. et al. 2014. Development and Validation of Fully-Coupled Hydraulic Fracturing Simulation Capabilities. Presented at the 2014 SIMULIA Community Conference, Providence, Rhode Island.

Zoback, M.D. 2010. Reservoir Geomechanics. Cambridge University Press.